MACHINABILITY OF CLEAN THIN-WALL GRAY AND DUCTILE IRON CASTINGS

Final Report

February 1997

Work Performed Under Contract No. FC07-94ID13319

For
U.S. Department of Energy
Assistant Secretary for
Energy Efficiency and Renewable Energy
Washington, DC

By
University of Alabama at Birmingham
Birmingham, AL

MASTER

MACHINABILITY OF CLEAN THIN-WALL GRAY AND DUCTILE IRON CASTINGS

Final Report

Charles E. Bates
Harry E. Littleton
Evangelos Eleftheriou
Robin D. Griffin
Zoe B. Dwyer
Carl DelSorbo
Jeff Sprague

February 1997

DISCLAIMER

MACHINABILITY OF CLEAN THIN WALL
GRAY AND DUCTILE IRON CASTINGS

Table of Contents

Table of Contents Continued

LIST OF FIGURES

LIST OF TABLES

MACHINABILITY OF CLEAN THIN WALL
GRAY AND DUCTILE IRON CASTINGS

ABSTRACT

The first phase of this project was conducted to develop a laboratory technique for evaluating the machinability of gray and ductile iron. The technique was then used to measure the machinability of irons from a variety of sources, and the metallurgical factors controlling machinability were determined. A longer term goal is to learn how to modify the foundry process to produce castings that meet all specified mechanical properties while providing substantially improved machining behavior.

The procedure developed for evaluating machinability involved drilling holes with a feed rate of 0.009 in/rev at various surface speeds. High speed steel (HSS) drills were used so wear could be more quickly observed. Future studies will include turning, milling, and boring and will involve higher performance tool materials.

Microcarbides present in the irons were found to dominate the machinability of iron. Pearlitic irons considered to have "acceptable" machinability were found to contain from 8.9 to 10.5% by weight microcarbides. The weight fraction microcarbides in the iron is influenced by carbide forming element concentrations, the presence of elements that retard carbon diffusion, and the cooling rate from the eutectic through the eutectoid temperature range.

The tool wear rate increased when machining at higher surface speeds and when machining irons containing higher weight percentages of microcarbides. All irons containing above 11.5% microcarbides consistently exhibited poor machinability. Other factors such as graphite size, shape, and distribution affected machinability, but the iron carbide weight fraction had a dominant effect.

Tool wear results obtained using tungsten carbide (WC) and cubic boron nitride (CBN) cutters in commercial machine shops paralleled the results obtained with HSS. Irons with higher microcarbide concentrations produced faster tool wear.

Inoculation trials were conducted in a ductile iron foundry using a grade 65-45-12 ductile iron. The amount of inoculant added was found to have a significant effect on tool life. Reducing the addition of a foundry grade calcium and aluminum bearing 75% FeSi inoculant from 0.5% to 0.2% increased the tool life by about 100%. A companion set of inoculation test castings were poured in a class 40 gray iron, and laboratory analysis is currently underway.

Exploratory studies were conducted to determine if tool force measurements could be used to predict tool life. Torque and feed

forces were found to correlate with machinability. This report
summarizes the data currently available on gray and ductile cast iron.

INTRODUCTION

The Clean Iron Production and Machining project was undertaken in 1995 to develop benchmark data on the machinability of gray and ductile iron, compare benchmark data to results obtained on castings produced in commercial foundries, define inclusions and other conditions that degrade machinability, evaluate inoculants for their effectiveness in minimizing chill and improving machinability, and demonstrate the best technology for mitigating factors that degrade machinability. This report summarizes the principal experimental results obtained during Phase I.

The general approach consisted of pouring non-commercial castings in production foundries using a wide variety of melt practices. Most of the work was conducted on plate castings made under a wide variety of production conditions. The plates were used to develop tool life curves using high speed steel (HSS) drills.

"Acceptable" and "hard-to-machine" commercial castings were also obtained from sponsor companies to determine if differences could be found in microstructures or compositions that would explain the reported differences in machinability. Samples of "acceptable" and "hard-to-machine" castings submitted by four companies have been analyzed.

MACHINABILITY LITERATURE REVIEW

Machinability has been defined by Boulger (1) as "a complex property of a material which controls the facility with which it may be cut to the size, shape, and surface finish required commercially". Many attempts have been made to experimentally measure machinability, and numerous machinability tests have been described in the literature.(1,2-6)

Evaluations of machinability are usually based on determinations of tool life, rate of metal removal, or power consumption. Relatively few investigators have made surface finish the primary basis for rating machinability although surface finish is an important criteria. The surface finish often controls the machining practice followed.

Machinability tests are customarily accomplished by standardizing a machining operation to eliminate the effects of as many variables as possible and then measuring the effects of other variables believed to have a relationship to machinability. For example, the quantity of metal removed at a constant feed load or tool-life is often used as a criterion. Measurements of the amount of heat generated or the power consumed during a cutting operation on a given machine have also been used as a basis for comparing machinability tests.(2)

Because of numerous assumptions and various test types, the results of machinability tests are often inconsistent. Even if each test answered a particular question, sufficient knowledge of metal cutting is not available to integrate the results of individual tests into a comprehensive understanding of metal cutting.

Generally, materials with lower strengths and ductilities exhibit better machinability. However, for some metallic materials, strength and ductility are inversely proportional, and consequently, the desired balance between machining behavior and mechanical properties is not easily obtained.

Two types of machinability evaluations are generally recognized.(3) These are "short" tests based on material characteristics and "long" tests based on tool-life. Short tests are desirable since they are less influenced by some of the uncontrolled variables encountered in tool life experiments. However, most tests in use at the present time are of the long (tool-life) type, requiring considerable expenditures of time, effort, and material.

Machinability has been defined by Schlesinger as "the resistance of a material, if adequately machined, measured by the main cutting force in pounds." Tool-life is defined as the time between resharpening under standard conditions of tip contour, feed, speed, chip cross-section, etc. Both short and long machinability tests require careful control of such variables as tool material, tool shape, cutting edge sharpness, chip cross-sectional area, ratio of

4

depth cut to feed, cutting speed, machine tool used, and surface quality of the cut produced.

A drill test is a typical and relatively simple machinability evaluation procedure. The number of revolutions of a standard test drill is plotted against the depth of penetration or rate of drill penetration under a fixed thrust load. Control tests are run before and after each sample to check the drill sharpness.

The milling test developed by Field and Bullock is a typical long-term tool life test.(5) The test consisted of machining 6.5 by 3.5 by 20.5 inch cast-iron blocks in a hydraulically controlled milling machine equipped with a single-tooth cutter mounted in a 500-pound flywheel. The cutter consisted of a carbide tip brazed to a shank and ground to predetermined tip contour and dimensions.

The machinability evaluation procedure consisted of making 6 inch wide by 0.187 inch deep cuts in the iron block. Tool wear was determined by measuring the width of wear on the tooth clearance land with a Brinell microscope after each pass. Tool life was evaluated in terms of several criteria including the cutting time to dull one tooth, the number of chips required to dull one tooth, the total length travel by the tooth, the total volume of metal removed per tooth, and the cubic inches of metal removed per inch of cutting edge per tooth. A land wear of 0.030 inch was considered to produce a dull tooth.

The most significant of these criteria was considered to be the volume of metal removed per tooth, since this gave a direct indication of the number of parts that could be milled before the cutter had to be resharpened. Corresponding studies of power consumption and surface finish produced during the tool life were also described.

Ernst summarized the important developments associated with the principles of machining.(6) Reviews of the works of Rosenhain, Sturney, and Herbert in England, Klopstock and Schwerd in Germany, Boston at the University of Michigan, and others were included as important chapters in the monograph.(6)

Ernst described the two fundamental processes involved in metal cutting operations using the analogy of a flat-faced punch being forced into a block of ductile material. First, there is compression and flow of the metal along the face of the tool, and second, there is either a rupture or plastic flow in a direction generally perpendicular to the face of the tool. The occurrence of one or the other of these two alternatives (rupture or plastic flow) determines the type of chip that will be produced. When rupture occurs, as with relatively brittle materials, a discontinuous or segmented type of chip is produced. The entire compressed region passes off with the rupture of each segment, and the cycle is repeated. When plastic flow occurs, as with relatively ductile materials, a continuous or flow type of chip results having a more or less uniform structure.(6)

5

Ernst also described the three fundamental types of chips produced during metal cutting. Type 1 chips are discontinuous or segmented. Chips of this type are characteristic of brittle materials. The point of the cutting tool engages the material, compresses it, and causes material to escape along a trajectory toward the free space above the cutting edge. With additional movement, the plastic flow extends along a trajectory farther and farther ahead of the tool until finally a rupture occurs approximately perpendicular to the tool face. The entire chip segment then passes off up the face of the tool, and the cycle is repeated indefinitely.

Type 2 chips consist of a continuously escaping compressed layer adjacent to the tool face. In ductile materials, where conditions are favorable in other respects, the successive ruptures characteristic of the Type 1 chip will not occur. At the beginning of the cut, the material is compressed and escapes outwardly along the tool by plastic flow as in Type 1. But as the work continues its advance upon the tool, the increasing stress toward the part surface causes continuous flow in this direction.

As plastic flow takes place by deformation on a multitude of crystallographic slip planes, an aggregate movement occurs without rupture. However, such deformation is normally accompanied by work hardening. The effects of work hardening on tool life and surface finish have been described by Merchant.(7) Microhardness measurements indicated that the surface hardness may increase as much as 300% by work hardening during certain cutting operations.

Type 3 chips are continuous chips with a "built-up edge" adjacent to the tool face. In practical machining operations, particularly when cutting low-carbon steel with high-speed steel tools, the ideal chip (Type 2) is seldom obtained. High friction caused by atomic bonding between the compressed layer of metal and the tool face, aided by the high temperatures and high specific pressures, cause the compressed layer to bond to the tool face to form a built-up edge while the chip body shears away and passes off.

The compressed metal or built-up edge becomes increasingly larger and increasingly unstable and eventually failure occurs. Fragments of the built-up edge are torn off and escape both with the chip and with the work piece. This building up and breaking down of the built-up edge occurs at a rapid rate, and as a result, the surface of the finished work has many adhering fragments of built-up metal. These fragments cause surface roughness, the degree of roughness being a function of the average fragment size on the tool edge.

In recognizing the difficulty of formulating a comprehensive definition for the term machinability, Ernst states:

We are attempting to use one word, machinability, to cover at least three different material properties; first, the ease with which a chip may be removed, i.e., the true machinability, which is probably a direct function of the tensile strength of the material; second, the

6

ease with which a good finish may be obtained, which means the ease with which we may achieve or approach the ideal Type 2 chip, and which is therefore probably an inverse function of ductility (for lack of a name for this property we may coin the word "finishability"); and third, the tendency of the material to abrade the tool, which is the negative property, abrasiveness.

If, instead of grouping these three conflicting properties under one heading, we subdivide them into machinability, finishability and abrasiveness, we will be able to arrange groups of materials in definite series by rating them according to these three properties without reference to the requirements of a particular operation. In selecting the material for a given operation, however, we will naturally consider each property separately and evaluate the ratings in accordance with their importance in each particular case.(6)

Ernst pointed out that the fundamentals of metal cutting theory have been established and an understanding of certain metallurgical and machining operating factors have been obtained, but the knowledge is largely qualitative rather than quantitative. Much work will be required before the numerous variable factors can be brought under control to provide optimum results in machine output, finish, and tool life. Further studies are required in the field of stress distribution in the material being machined and the optimum workpiece temperature.

IRON MICROSTRUCTURE DEVELOPMENT

Many metallurgical factors have been postulated to affect the machinability of iron, but definitive data to support most of the theories is lacking. Metal processing factors suggested to affect machinability include:

1. type of melting furnace,
2. type of furnace lining,
3. furnace atmosphere during melting,
4. maximum metal temperature reached during melting,
5. oxygen dissolved during melting,
6. nitrogen dissolved during melting,
7. trace elements picked up from the charge materials,
8. type and composition of the material used as the carburizer,
9. type of silicon addition,
10. moisture in the furnace,
11. time that the metal was held at an elevated temperature after melting,
12. presence of elements that stabilize carbides in the iron,
13. type and amount of inoculant used to promote graphite formation during solidification,
14. when and how the inoculant was added,
15. the time interval between the inoculant addition and metal solidification,
16. graphite size and spacing in the casting,
17. rate of casting solidification,
18. rate of casting cooling in the mold,
19. mold shakeout time,
20. rate of cooling after the casting was knocked out of the mold, and others.

The list of possibilities is great and the amount of supporting data for each idea is relatively small.

This section reviews the literature on metallurgical structure development in iron. Prior research has shown that the structure of iron has a significant affect on machinability.(1,5) It is therefore important to understand microstructure development because improving machinability will require changes in the microstructure. As experience and data grow, it may be possible to develop data to substantiate certain theories, serve as the basis for better theories, and suggest methods to modify and improve machinability by microstructure control.

The solidification review describes the sequence associated with solidification and cooling of relatively pure iron-carbon and iron-carbon-silicon alloys. It is essential to understand solidification because virtually all gray irons and the majority of ductile irons must be machined in the as-cast condition. Heat treatment adds too much to the cost of the castings even though it could be used to improve the machinability.

8

Phase Formation in Cast Iron

Iron is an element in the periodic chart, and the term "cast iron" refers to an iron alloy containing more than 1.7% carbon. Iron alloys containing less than about 1.7% carbon are technically steels, but very few steels are produced that contain more than about 1% carbon, and most contain less than 0.5% carbon. Throughout this review, the term "iron" will be used to refer to cast iron usually containing from 3.2 to 3.7% carbon. The term "cast iron" will be used generically to refer to all types of high carbon alloys. The term gray iron (flake graphite iron), ductile iron (nodular graphite iron), and malleable iron (aggregate graphite iron) will be used when discussing irons with particular graphitic forms.

Most commercial cast irons contain 3.2 to 3.7% carbon, 1.8 to 2.4% silicon, 0.5 to 0.8% manganese, and smaller amounts sulfur, chromium, copper, nickel, tin, phosphorous, and other minor elements. When cast irons solidify, the solid phases formed are austenite, graphite, iron carbide, manganese sulfides, and if the phosphorus concentration is high enough, a ternary iron-phosphorus-carbon compound. The graphite shape and distribution in both gray and ductile iron is dominated by

1. the chemical composition of the molten metal,
2. the state of melt nucleation,
3. the presence of elements that restrict graphite or eutectic cell growth,
4. surface active elements including sulfur and oxygen, and
5. the rate of heat removal from the metal by the mold.

The overwhelming majority of iron castings produced today require that iron solidify to allow the liquid to decompose to form austenite and graphite. Massive (eutectic) carbides must be minimized since their presence degrades the ductility, produces hard spots, and makes the resulting products hard to machine.

Minimizing iron carbide formation demands that graphite form during eutectic solidification. For graphite to grow, it must first be nucleated. Homogeneous nucleation is thermodynamically difficult, so nucleating additions are almost always made to cast iron before pouring. These nucleating additions are referred to as inoculants, and their purpose is to provide substrates upon which the graphite can begin to grow near the austenite-graphite eutectic temperature. Graphite flakes grow from these nucleation sites, and all graphite growing from a particular nucleus is interconnected. The interconnected graphite and the associated austenite formed during eutectic solidification is referred to as a eutectic cell.

Eutectic solidification begins at the cell nucleus and progresses by radial cell growth until cells begin to impinge. The impingement area is enriched in phosphorus, molybdenum, and other elements more soluble in liquid than in solid iron. The impingement areas are referred to as the eutectic cell boundaries. If the graphite is not

nucleated and the iron undercools a few degrees below the austenite-graphite eutectic temperature, massive (eutectic) iron carbides will form. The formation of massive iron carbides is undesirable and must be minimized.

When cast iron has solidified and the heat (enthalpy) associated with solidification has evolved, the iron cools at a rate proportional to the heat removal characteristics of the mold. As the iron cools, the carbon solubility in the austenite decreases from about 1.7% at 1150°C (2100°F) to about 0.7% at 715°C (1320°F). The decrease in carbon solubility causes about one weight percent carbon to be rejected from the austenite as the iron cools through a 400°C range. The carbon may precipitate onto existing graphite flakes or nodules, may precipitate as microscopic iron carbides in the austenite, or remain in the austenite (supersaturated austenite).

Another structural change occurs when iron reaches the eutectoid temperature of approximately 715°C (1320°F). At or near this temperature, the austenite decomposes to produce either ferrite and carbon or ferrite and thin sheets of iron carbide. The alternating lamallae of iron carbide and ferrite is called pearlite. The eutectoid transformation, by definition, consists of one phase (austenite) decomposing to form two new phases (ferrite and iron carbide).

The thermodynamically stable phase combination is ferrite and graphite, but graphite growth requires sufficient time for carbon to diffuse from the austenite over distances of 5-25 microns to attach to existing graphite. The conditions that make it difficult for the austenite to decompose into ferrite and graphite include:

1. cooling rates which do not provide sufficient time for carbon diffusion,
2. the presence of elements that either retard carbon diffusion or retard attachment of the carbon to preexisting graphite, and
3. the presence of elements that reduce the free energy difference between graphite and iron carbide.

Structures composed of ferrite and graphite have relative low strength and hardness. A microstructure consisting of the lamellar arrangement of ferrite and iron carbide platelets (pearlite) has a much higher strength and is usually the preferred structure in gray iron and many ductile irons.

Solidification of Ternary Fe-C-Si Alloys

The effect of a third alloying addition on the composition of phases and transformation temperatures can be observed using a ternary phase diagram. However, a ternary phase diagram presented in 3-dimensional space is more difficult to visualize than a 2-dimensional binary phase diagram. Isopleths are often used to simplify multicomponent phase diagrams. Isopleths are vertical sections

10

through phase diagrams of alloys containing three or more components at a constant concentration of one or more elements.

Isopleths provide information on the stable phase fields as elemental concentrations and temperatures change. The lever rule does not apply when using isopleths, and calculations regarding the weight of a particular phase present cannot be made from the diagram.

Superimposed iron-graphite and iron-Fe_3C diagrams at zero silicon concentration are shown in Figure 1(A).(8) The iron-iron carbide isopleths at 2% and 4% silicon are illustrated in Figures 1(B) and 1(C), respectively. Note that the eutectic carbon concentration, and the carbon solubility in austenite at the eutectoid temperature decrease as the silicon concentration increases. The eutectic composition shifts from approximately 4.3 wt % C at 0 wt % Si to approximately 3.0 wt % C at 4 wt % Si.

The presence of silicon also splits both the eutectic and eutectoid temperatures into a temperature range as illustrated in Figure 1.(8) These ranges represent fields in which three phases - liquid, austenite, and iron carbide - are in equilibrium. At temperatures just above the eutectic range, only liquid and austenite are present in a hypoeutectic iron. At temperatures just below the lower limit of the range, austenite and iron carbide are in pseudo equilibrium. The equilibrium iron-graphite phase diagram is similar to the iron-iron carbide phase diagram as shown in Figure 2.(9) However, the iron-graphite phase diagram is shifted to slightly higher temperatures as illustrated by the solid line, in Figure 2.

Graphite Formation from Liquid Iron

The formation of graphite in gray and ductile iron begins with the nucleation of graphite in the liquid metal, and growth occurs by the addition of carbon atoms to the surface of the nucleus. Carbon atoms diffuse through liquid metal or solid austenite and attach to the growing graphite lattice. Carbon diffusion is relatively rapid in liquid iron and in solid austenite near the solidification temperature.

The process of nucleating graphite in iron is considerably more difficult and requires a higher free energy change than growing graphite on a stable nucleus. The difficulty in nucleating graphite often results in some undercooling of liquid metal below the equilibrium graphite formation temperature.

The state of melt nucleation is influenced by the iron composition, addition of special nucleants, and the cooling rate. Certain elements, notably sulfur, exert a marked effect on graphite nucleation in gray iron. Carbon and silicon concentrations are also important. The carbide formers - chromium and vanadium - interfere with graphite formation.
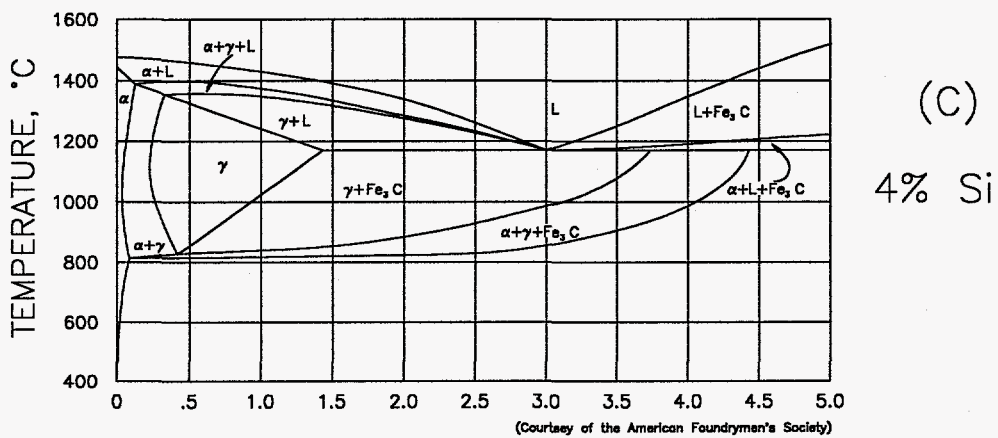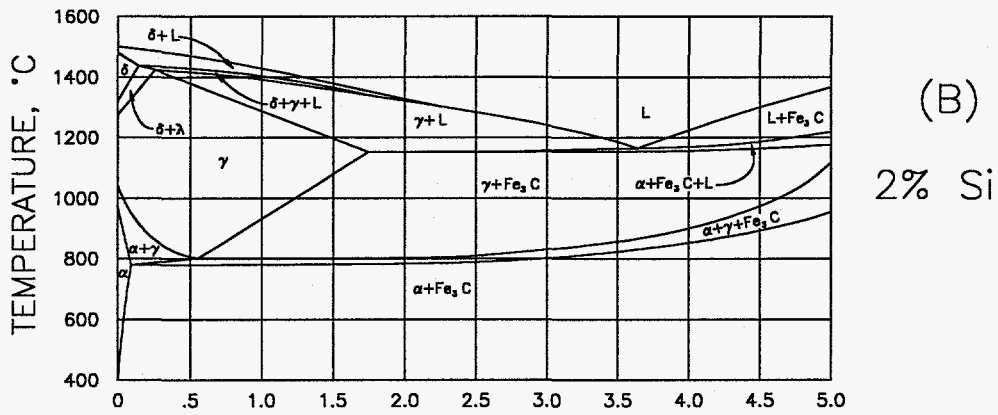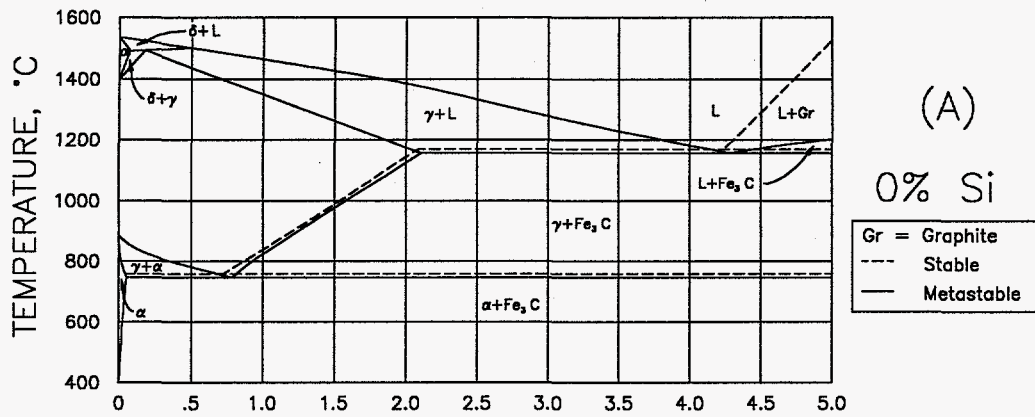
Figure 1.   Vertical Sections Through the Iron−Carbon−
Silicon Ternary System at (A) 0, (B) 2, and
(C) 4% Si.
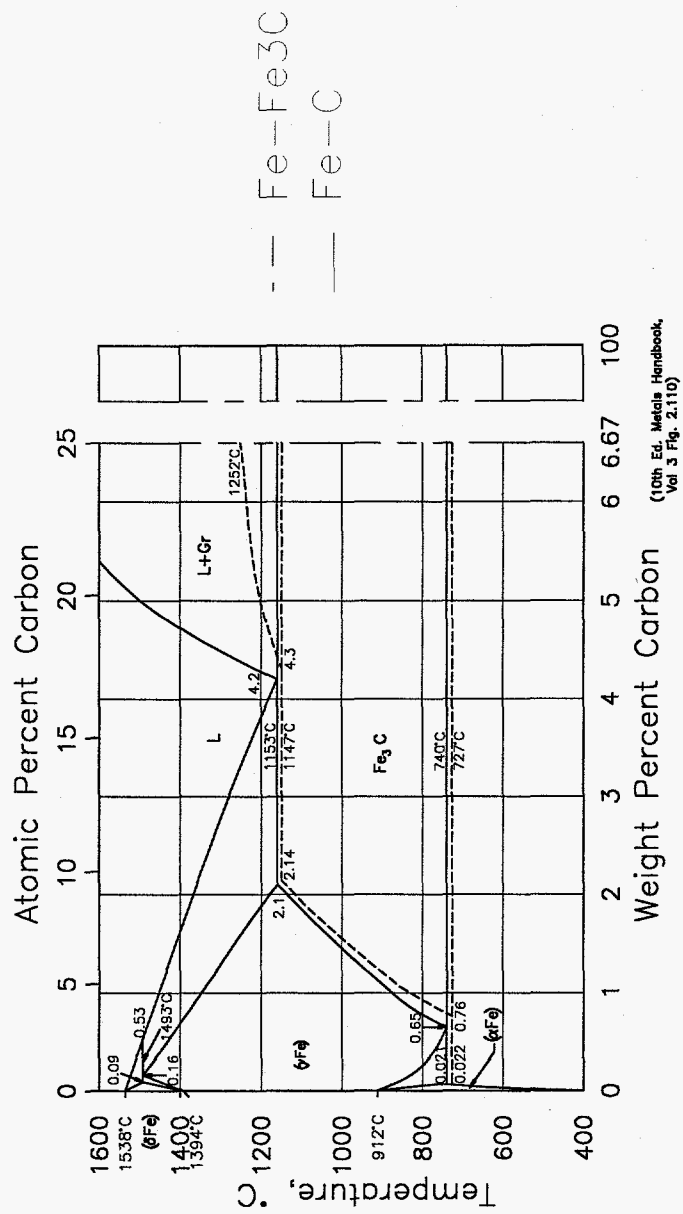
Figure 2. Superimposed Fe-Fe3C and Fe-C Phase Diagrams

13

The number of nuclei activated to initiate eutectic cells is increased by faster cooling.(10) However, if sufficient heat is not evolved by small eutectic cell growth, undercooling below the temperature range suitable for graphite formation occurs, and solidification occurs to form the iron carbide-austenite eutectic.

Nucleation determines the number of growth sites for graphite particles, but the growth process controls the final graphite shape and distribution. Graphite flakes in gray iron consist of sheets or planes of crystals with basal planes on the sheet faces. The weak bonds between the basal planes permit relatively easy displacement facilitating the bending, turning, and twisting of flakes as they grow.

Spheroidal graphite growth proceeds radially from the nucleation point in the graphite c-axis direction. A nodule consists of columnar graphite crystals with basal planes tangent to nodule surfaces. The spheroidal graphite shape is considered a result of high interfacial energy difference between the melt and graphite and a result of different growth rates on different planes of the graphite crystal.(11-15) Flake graphite forms when conditions favor growth perpendicular to prism planes. The graphite assumes a spheroidal form when growth occurs perpendicular to basal planes.

Graphite Growth in Gray Iron

The mechanisms of graphite growth in gray iron are fairly well established. Some of the more general references are listed in the bibliography, but many more are available.(10,16,17-24) The early work of Boyles established that flake graphite in hypoeutectic and eutectic irons grows in contact with the liquid iron and with austenite.(25) Kish or Type C graphite also grows in contact with the melt, but without companion austenite growth, so it is subject to less mechanical restraint. Because of the reduced restraint on kish graphite and the relatively small amount of material precipitated from the melt, Kish has a characteristic straight shape compared to the more irregular forms of eutectic graphite.

The eutectic graphitic forms are well known to all iron foundrymen. The so-called randomly oriented, Type A graphite is known to be interconnected with a junction at the eutectic cell center since the early work of MacKenzie.(26) More recent work has established that the undercooled Type D graphite is also interconnected. Type B or the rosette type graphite has a Type D center and Type A graphite at the outer portions of the eutectic cell. Type E graphite has an oriented structure with small graphite flakes distributed around prior austenitic dendrites. Type D generally occurs in irons of lower carbon equivalent.

The state of nucleation existing in the melt when various types of graphite form is also well established. The growth rates of the different graphite types follow directly from the amount of undercooling. Type A graphite nucleates and grows relatively slowly

14

with only limited undercooling. Type B graphite grows rapidly at the central portion of the cell, but the undercooling is relatively low so the heat evolved during initial eutectic growth raises the temperature of the remaining liquid to near the equilibrium eutectic value. Growth then proceeds more slowly providing the Type A graphite around the cell periphery. Type D and E graphite grow at relatively high radial growth rates.

Graphite Growth In Nodular Iron

The state of nucleation in nodular iron is influenced by composition, cooling rate, and inoculation just as in gray iron. However, nodular iron has a somewhat lower eutectic arrest temperature. The end of eutectic arrest for nodular graphite is less well defined as indicated by the gradual sloping off from the eutectic temperature.(18,27,28)

The addition of magnesium or cerium to cast iron in amounts sufficient to produce nodular graphite causes massive iron carbide formation, especially at higher cooling rates. Massive carbides may be avoided by suitable post-inoculation if the magnesium concentration is in the correct range. The alloys used as post-inoculants in ductile iron are the same as those used for inoculation of gray irons. Increasing additions of post-inoculants increase the number of nuclei present and, therefore, the number of nodules observed at any cooling rate.(10)

Irons with nodular graphite differ from irons containing flake graphite in the number of cells that grow. The number of eutectic cells in nodular iron may be 100 times greater in a given volume than in flake irons of comparable carbon equivalent.(10)

Effects of Processing and Composition on Microstructure

Higher states of graphite nucleation in the melt are favored by the following:

1. graphitic materials in the charge,
2. the addition of effective inoculants, particularly those with appreciable calcium, aluminum, and rare earth concentrations, and
3. reducing conditions in the melting furnace (CO atmospheres).(29-30)

The presence of factors that lower the state of graphite nucleation and increase iron carbide formation include the following:

1. oxidizing conditions in the furnace,
2. steel in the charge,
3. water vapor in the furnace atmosphere, and
4. superheating the metal.(29,30)

15

The chemical composition of the melt also exerts a marked influence on iron carbide formation. These effects are produced by the following:

1. those elements such as C, Si, Mn, S, P normally present in molten iron,
2. trace elements in the melt (Cr, V, W, Sb, H_2 N_2 O) from the charge or furnace atmosphere, and
3. elements deliberately added by inoculating additions such as Ca, Al, Sr, etc.

Higher carbon and silicon concentrations decrease the tendency for iron carbide formation perhaps by enhancing graphite nucleating conditions or by expanding the eutectic temperature range. Stoichiometric relations require Mn concentrations according to the following formula: 1.7 x wt % S = wt % Mn to form MnS. The usual procedure is to allow an excess of Mn by such formulas as 2 x %S = %Mn, or 1.7%S + 0.2% = % Mn to obtain a Mn-S balance.

Other trace elements, including Sn and Sb, appear to have a small effect on iron carbide formation but stabilize pearlite. Small amounts of titanium, depending to some extent on the sulfur content, can promote undercooled graphite formation. (23,29,30)

The presence of hydrogen and nitrogen dissolved in molten iron favors iron carbide formation during solidification. These gases have been shown to have a chill effect in cast irons and are thought to promote iron carbide formation by inhibiting the growth of the graphite-austenite eutectic. Dissolved oxygen also favors iron carbide formation perhaps by reducing the state of graphite nucleation. (23,29,30) Small additions of bismuth and tellurium sharply increase iron carbide formation.

High rates of cooling during solidification usually increases the amount of eutectic undercooling and favors the formation of metastable iron carbide and austenite in preference to austenite and graphite. In thicker casting sections, the amount of undercooling is lower, and the opportunity for primary graphite to form is favored by the slower cooling rates.

Melting and Casting Variables

Graphite-bearing materials in the charge assist graphite nucleation, and steel in the charge reduces the tendency for graphite nucleation. Oxidizing conditions in the furnace also decrease the tendency for graphite nucleation. Thin section castings reduce the tendency for graphite nucleation due to the rapid cooling rates. Thick section castings promote graphite nucleation due to the slower cooling rates.

Summary

An analysis of the mechanisms of graphite formation in Fe-Si-C alloys requires an understanding of graphite nucleation in the liquid or solid and its subsequent growth. The formation of stable graphite nucleus in molten iron is a relatively difficult process. This requires a sufficient number of carbon atoms to deposit onto a solid particle (called a substrate or heterogeneous nuclei) having a crystallographic structure that favors carbon growth on it. The number and effectiveness of these substrates or particles varies. Only a small amount of undercooling is required for graphite nucleation when substrates are numerous and effective. When the particles are few and less effective, the amount of undercooling increases. A sufficient amount of undercooling results in the formation of the metastable phase, Fe_3C, rather than the stable graphite during the solidification of the cast iron.

The same nucleating additions are effective in both gray and nodular irons, although the melt history in each case favors the use of certain types. The more effective substrates for heterogeneous graphite nucleation include salt-like carbides (calcium, aluminum, and silicon carbides), graphite particles, sulfides that may form during cerium and magnesium treatments, and boron nitride. The localized, high-silicon areas resulting from additions of silicon-rich metals also aid graphite nucleation. Inoculation of gray iron or post-inoculation of nodular iron is performed to provide effective substrates for graphite nucleation in the molten iron.

The growth of flake or spheroid graphite is determined primarily by kinetic factors resulting from absorption and incorporation of surface-active foreign atoms on the graphite surface. The presence of these foreign atoms influences the surface tension and interfacial energies. Cerium and magnesium appear to favor spheroidal growth in the liquid. These elements favor growth in the "c" crystallographic direction.

The influence of surface-active atoms determines whether flake, compacted flake, or combinations of spheroidal with compacted flake structures are obtained. Variations in the relative activity of these atoms on surface condition occur not only from iron to iron but also may vary within an iron.

EXPERIMENTAL PROCEDURES

Experimental Castings

All of the castings in this study were produced in commercial foundries. Most of the work was done with a ribbed plate as illustrated in Figure 3. The criteria for determining machinability was tool life which was defined as the number of holes drilled to produce a specified flank wear or flank wear rate. The tests were run over a range of cutting speeds to develop tool life curves.

Casting Production

Participating companies produced test castings under commercial conditions. Gray iron test plates were produced in six foundries under several production conditions and this resulted in thirteen sets of plates. These sets represented various classes of iron, melt practices, shake out times, and heat treatments as indicated by Table I.

Nine sets of ductile iron plates were produced in five foundries. These sets represent various iron grades, melt practices, and shake out times as summarized in Table II.

Continuous cast plates were also obtained in one ductile iron grade and one gray iron grade with the intent of using these materials as a machining standard material.

UAB personnel were present to document the pouring conditions of most test castings. A description of the melt practice including melting furnace, holding furnace, typical charge materials, type of inoculant, and type of molding system was obtained.

Several samples were also obtained during casting production. These samples included chemistry buttons cast in a copper chill mold, "A" and "B" bars to obtain tensile properties if necessary, and cooling curves.

Machinability Procedures

Drill Life Determination

Drills were obtained from a tool lot consisting of 0.25" diameter, high speed steel (HSS) drills certified by the manufacturer to be made from the batch of steel and produced on the same machine using the same grinding wheel. Each drill was used until failure occurred. Failure was defined as the point at which the drill "squealed" during drilling. Drilling one or two holes past "squeal" resulted in welding of the drill to the plate.

The procedure for the drillability test included the following steps:

TOP VIEW   BOTTOM VIEW

12.00"

3.25

0.50

6.00
8.00

2"
2"
2"
2"
1.00"
0.50"
0.25
2" Slant

0.50   3.25   0.50   3.25   0.50
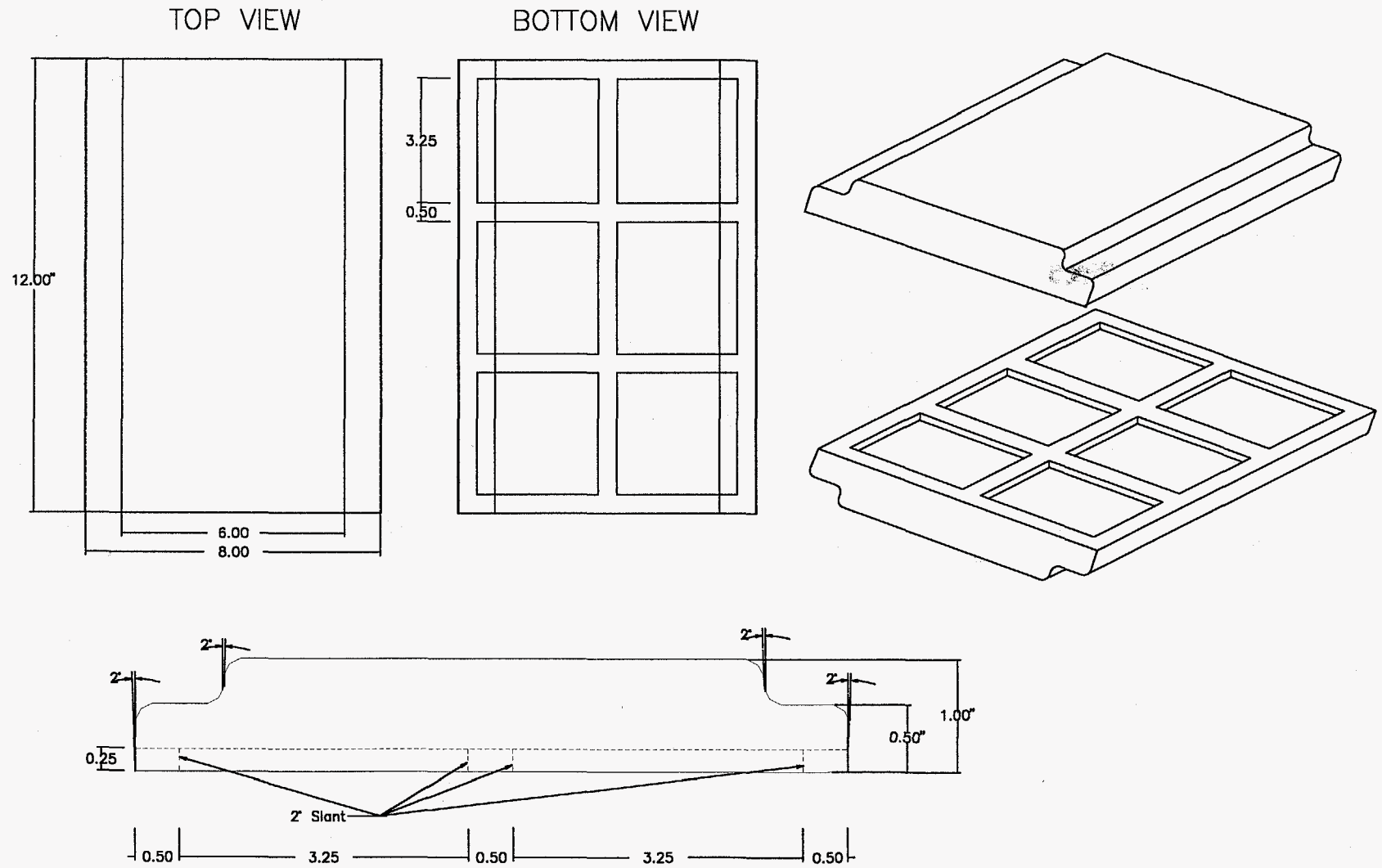
Figure 3. Proposed Ribbed Plate Casting for Machinability Project.

TABLE I

GRAY IRON PLATE CASTINGS SUBMITTED FOR MACHINABILITY ANALYSIS

Sponsor Code	Grade	Melting	Shake-out Time
GS	40	Induction	Fast
G1	30	Cupola	28 min.
G4	35	Cupola	33 min.
G5	35	Cupola	33 min.
G7	35	Cupola	18 min.
G7	35	Cupola	35 min.
G7	35	Induction	18 min.
G7	35	Induction	35 min.
G8	40	Induction	86 min.
G9	30	Cupola	18 min.

TABLE II

DUCTILE IRON PLATE CASTINGS SUBMITTED FOR MACHINABILITY ANALYSIS

Sponsor Code	Grade	Melting	Shake-out Time
DS	65-45-12	Induction	Fast
D1	65-45-12	Induction	60 min.
D1	80-55-06	Induction	60 min.
D3	80-55-06	Induction	60 min.
D4	80-52-03	Cupola	60 min.
D8	65-45-12	Induction	16-18 min.
*DF5	65-45-12	Induction	60 min.
*DF2	65-45-12	Induction	60 min.
*DB2	65-45-12	Induction	60 min.
*DA2	65-45-12	Induction	60 min.

*Inoculation Trial Irons Poured at a Participating Foundry.

1. The drill was examined under an optical comparator to ensure there were no chipped edges.
2. The drill was positioned in the tool holder so the cutting edge was parallel to the x-axis of the optical comparator.
3. These coordinates were recorded so that the same position could be found in successive measurements to establish standard reference points so that factors such as built-up material on the cutting edge would not affect the measurement.
4. The progressive tool wear test was run. Tool wear measurements were performed after drilling the first and second hole and then at various intervals depending on tool life.
5. The drill and chips from the test are collected and coded for future examination.

Drillability experiments were performed using at least four different speeds for each material and triplicate tests were performed at each speed. All tests were performed at the same feed per revolution (0.009 in/revolution) and on the same CNC vertical milling machine using programs which drilled 180 holes in the test plates.

The test plates were center drilled prior to performing the drill life tests. The drill cutting edges still encountered the cast surface. The holes were drilled on half inch centers (one drill diameter apart) to avoid strain hardening effects.

A procedure for measuring drill wear was also developed. The wear land area was digitized from the chisel edge to the lip of the drill by an optical comparator with the ability to project the surface. A fixture was mounted on the comparator so that drill wear could be measured while the drill was in the tool holder. Drill wear was measured on the flank face by measuring points along the wear surface and storing the measurements on a computer connected to the optical comparator.

A program was written to calculate the wear area from the stored data points. The program calculated an average wear value and a secondary wear value specifically defined in this study. The secondary value, high wear, was the average flank wear in the area from the mean tool radius to the lip. A schematic indicating these wear values is illustrated in Figure 4.

The calculated wear values were used to produce tool wear curves. The curves plotted the progressive tool wear versus the number of holes drilled at a given speed for the three sets of experiments. Examples of tool wear curves are shown in Figure 5. There was an initial break-in wear that occurred within the first few holes, and wear progressed after that point at an approximately linear rate.

The tool life criterion was based on the maximum wear observed in all tests. The "average" tool wear value used to represent the tool life was 0.0065 inch and the "high" wear value used was 0.009 inch.
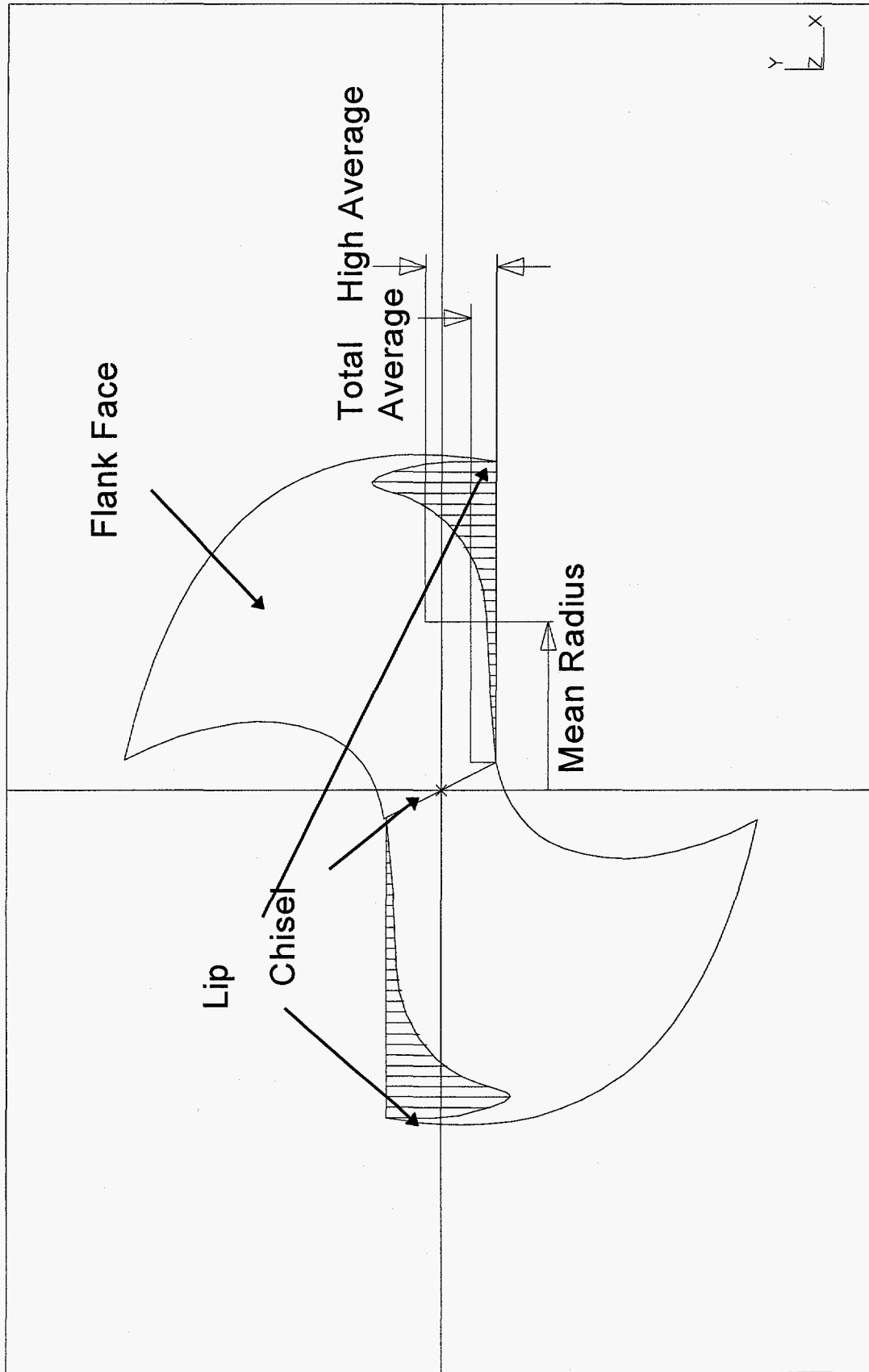
Figure 4. Schematic of Drill Wear Measurement.
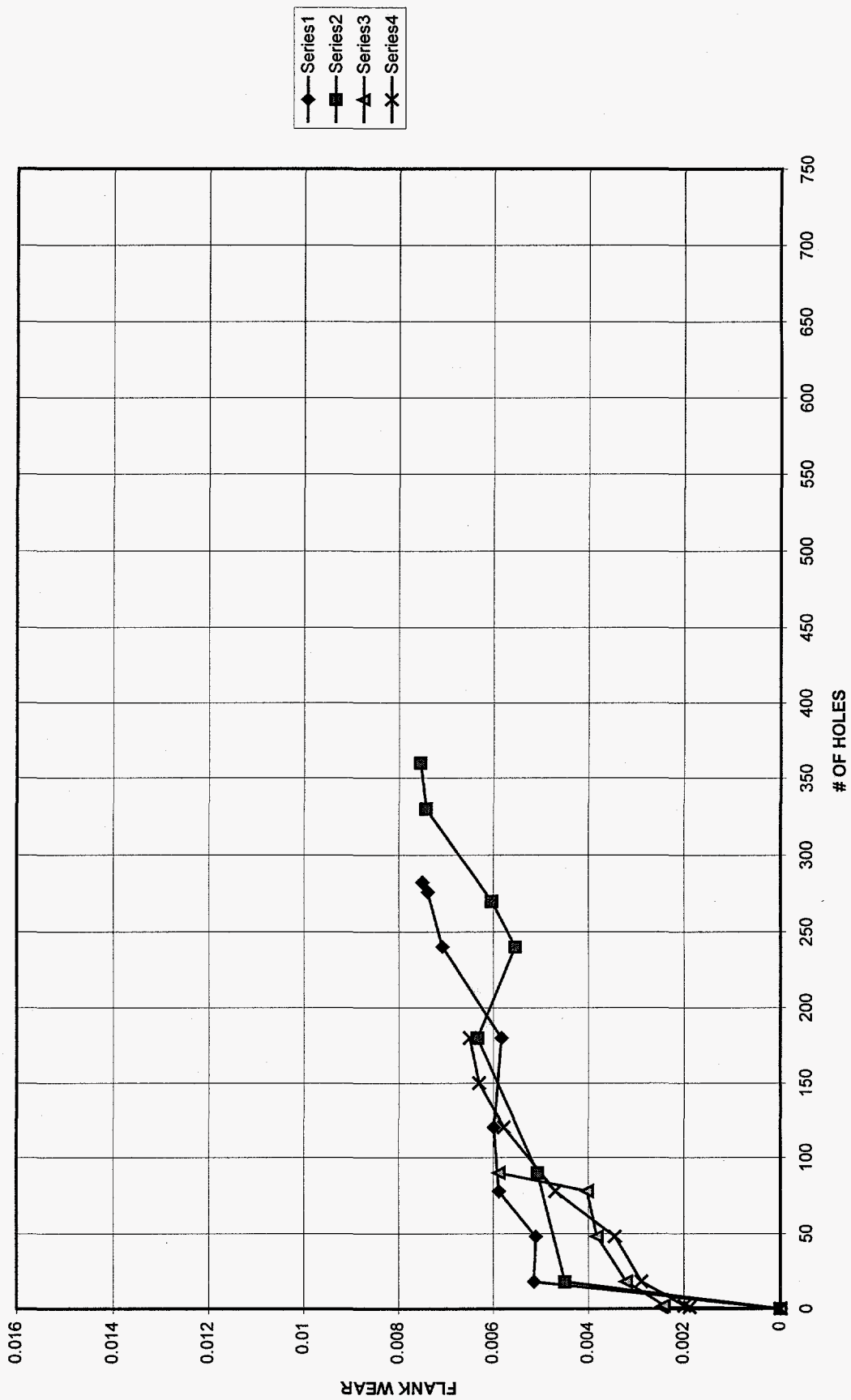
Figure 5. Wear Curve for a Class 35 Gray Iron with a Normal Cool at 124 sfm (G72).

Drill life was determined from the tool wear curve at the specified wear criteria. Tool life curves were plotted as a function of number of holes drilled versus speed (SFM) using tool life determined from the wear criteria. An example of a tool life curve is shown in Figure 6.

Another method of plotting tool life curves is common in presenting machinability data. Plotting the natural log of speed versus natural log of drill life usually produces a linear curve. The linearization allows easy calculation of the Taylor constant and exponent. The Taylor tool life equation is:

$$VT^n = C \qquad\qquad (1)$$

where   C =   the Taylor constant and
         n =   the Taylor exponent
         V =   cutting speed
         T =   drill life.

The Taylor equation may be rewritten as follows:

$$\ln T = -n^{-1}\ln V + n^{-1}\ln C \qquad\qquad (2)$$

where   ln = natural (base e) logarithm.

The slope of the line is $-n^{-1}$ and the y-intercept is $n^{-1}\ln C$ on a plot of ln(speed) versus ln(drill life). Using the Taylor equation, tool life may be calculated at other (untested) speeds after the constants are determined. An example of a Taylor tool life curve is shown in Figure 7.

Chemical Analysis of Experimental Castings

A typical composition was provided by the foundry for all plates submitted for machinability evaluation. These compositions are presented in Appendix A.

Cutting Plans

The samples for microstructural and physical property analysis were removed from plates on completion of the machinability evaluations. Samples were removed for tensile properties, microstructural characterization, Brinell hardness measurements, chemical analysis, and microcarbide analysis. A schematic of the test plate indicating the location of sample removal is shown in Figure 8.

Samples were removed using a band saw or an abrasive cut-off wheel. The density, and Brinell hardness samples were machined so that the sides were plane and parallel.

OF HOLES AT A WEAR CRITER IA OF AVERAGE WEAR = 0.0065"

DRILL SPEED IN SURFACE FEET PER MINUTE (SFM)
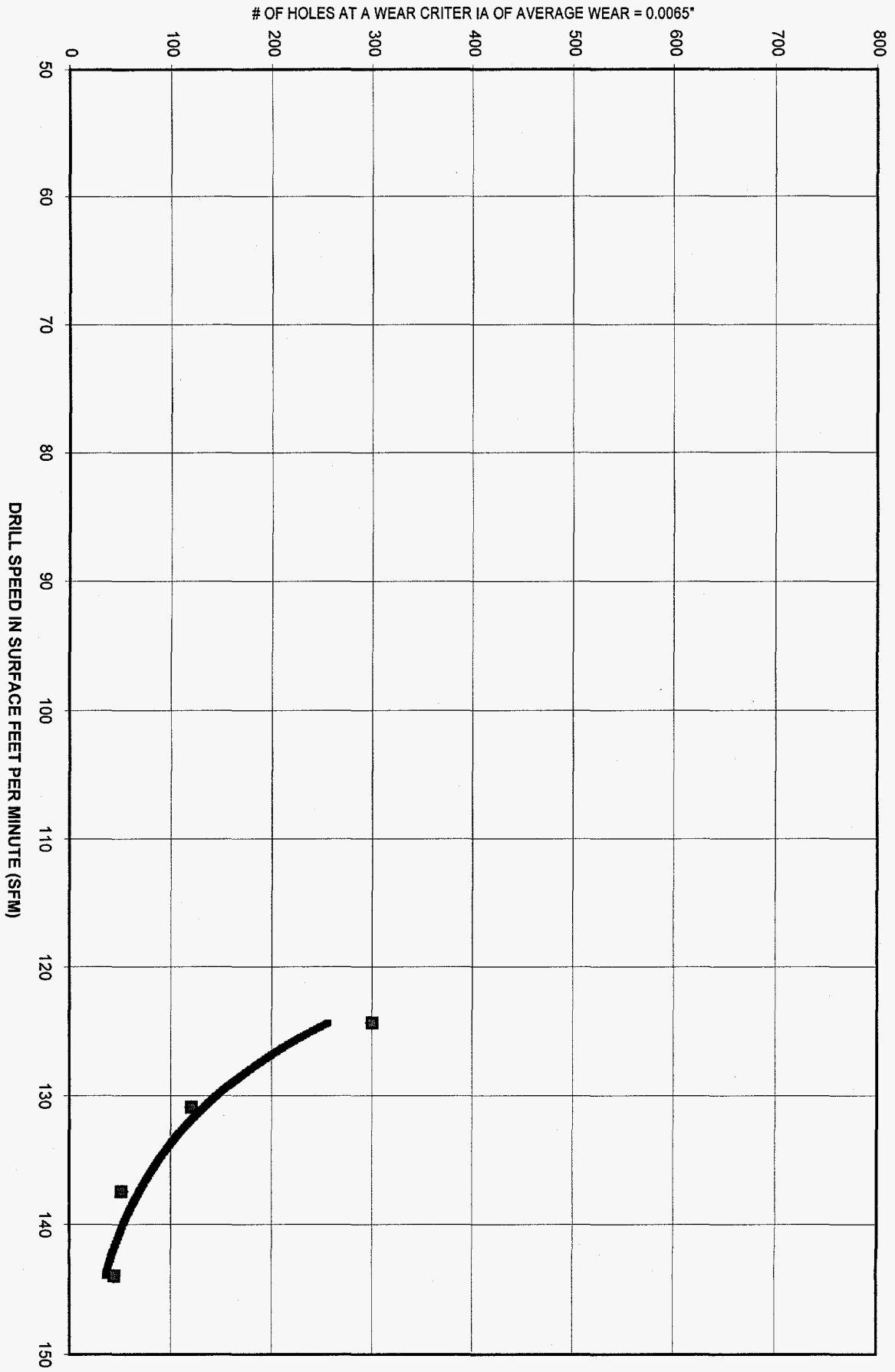
Figure 6. Tool Life Curve for a Class 35 Gray Iron with a Normal Cool (G72).
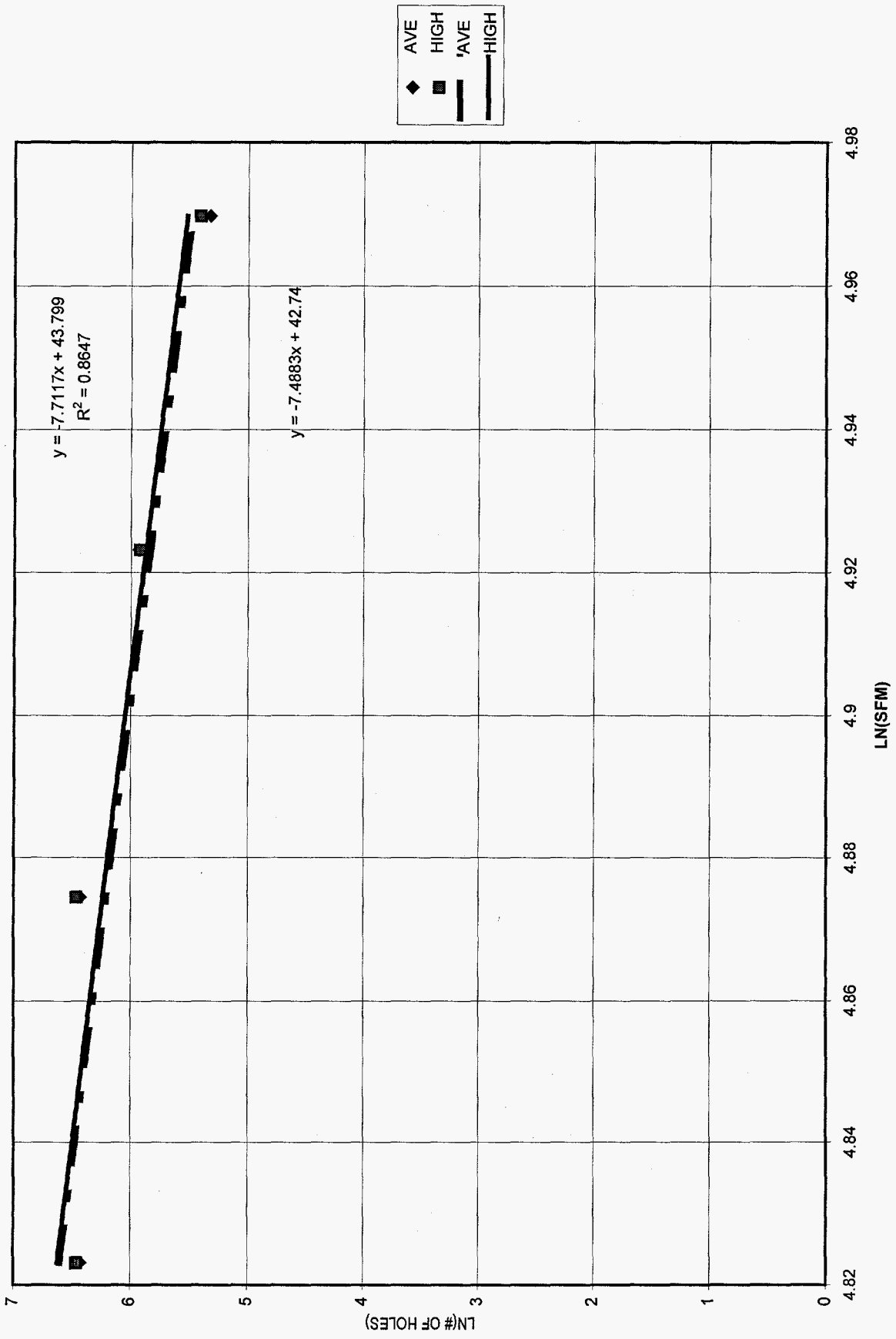
Figure 7. Taylor Tool Life Curve for a Class 35 Cupola Melted Gray Iron with a Slow Cool (G76).

GATE

1/2"

3 5/16"

UAB Tensile

5"

1/2"

12"

3 5/16"

Ultrasonic/Density   SRI Tensile   OM   CC   CH

4"

1/2"

3/4"

1/2"

3 5/16"

1/2"
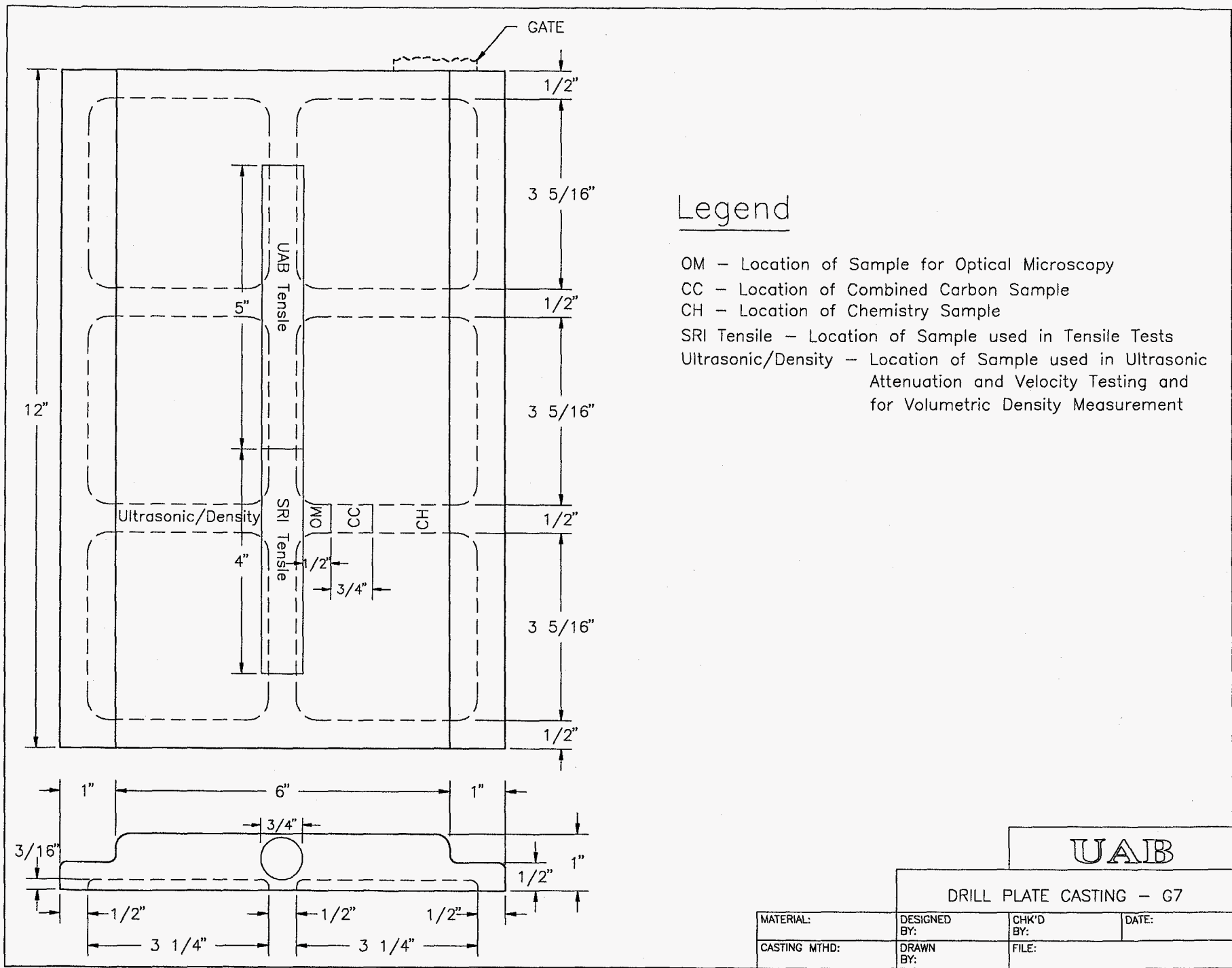
Legend

OM — Location of Sample for Optical Microscopy

CC — Location of Combined Carbon Sample

CH — Location of Chemistry Sample

SRI Tensile — Location of Sample used in Tensile Tests

Ultrasonic/Density — Location of Sample used in Ultrasonic
Attenuation and Velocity Testing and
for Volumetric Density Measurement

1"   6"   1"

3/4"

3/16"

1"

1/2"

1/2"   1/2"   1/2"

3 1/4"   3 1/4"

UAB

DRILL PLATE CASTING — G7

MATERIAL:	DESIGNED BY:	CHK'D BY:	DATE:
CASTING MTHD:	DRAWN BY:	FILE:	

Figure 8.   Schematic of Test Plate Indicating Location of Sample Removal.

Microstructural Analysis

Polishing Procedures

The samples for microstructural characterization were mounted in either Bakelite or an epoxy resin. Samples were ground using silicon carbide papers with grits ranging from 120 to 1200. The samples were etched for five minutes between grinding stages with Nital (5% nitric acid in methanol) to reduce graphite pull-out and burnishing. Grinding was performed both manually and automatically with a Leco AP-60 autopolishing head. Manual grinding was performed at each stage until all evidence of prior etching was removed. Autogrinding was performed for 10 minutes at each stage using a 15 lbf load and a 350 rpm wheel speed.

Burnishing effects were removed, prior to polishing, by etching with Nital for 10-30 seconds to reveal the matrix. Samples were polished manually and with the Leco AP-60 autopolishing head using 1 um diamond on napped polishing cloths composed of synthetic rayon fibers bonded to a woven cotton cloth. Glycerin/methanol extender was used with the 1 um diamond. The polishing cloth was continuously washed with methanol to prevent pull-out of the graphite flakes. Polishing was continued until all etching effects were removed. Autopolishing was performed using a 15 lbf load and a 350 rpm wheel speed. Firm pressure was used during manual polishing.

Etching

Graphite was examined in the unetched condition. Nital was used in the polishing procedure and also as an etchant after polishing to reveal the base microstructure.

Microstructural Characterization

Representative unetched optical microscope images were taken at 30X and 100X to determine the graphite class in the sample. The samples were etched with Nital and a 100X representative micrograph was taken to document the matrix microstructure.

The volume fractions of graphite, MnS, TiX, ferrite, pearlite and massive carbides were determined using grid counting techniques. The measurements were performed at 500X with a 5 point by 5 point grid. The volume fraction of a phase was determined by dividing the number of line intersections falling on the phase of interest by the total number of grid intersections. Equation 3 presents the formula used to make the calculation.

$$V_V = \frac{Number\ of\ points\ on\ phase}{Total\ number\ of\ points} \qquad \textbf{(3)}$$

The graphite volume fraction was also measured using an optical microscope and a Ziess Kontron automated image analysis (AIA) system.

Although this method was faster than the grid count method, slight changes in the camera contrast, or gain, and bulb intensity significantly changed the volume fraction of graphite measured.

The ratio of surface area of graphite to the volume of material (S_v) was obtained from a line measurement (P_L). This value was determined from the number of flake edge intersections with a test line, divided by the test line length. S_v was calculated using equations 4 and 5.

$$P_L = \frac{Number\ of\ boundaries\ crossed}{Length\ of\ test\ line} \tag{4}$$

$$S_V = 2\ (P_L) \tag{5}$$

Graphite surface area per unit volume (S_v) was determined using the automated image analyzer. The mean spacing between graphite flakes was obtained from the following equation:

$$\Omega_{Graphite} = 4 * \frac{V_{V_{Graphite}}}{S_{V_{Graphite}}} \tag{6}$$

Images were acquired from either an optical microscope or a Philips 515 scanning electron microscope.

Flake length distributions and average and maximum flake lengths were measured using an automated image analyzer. Scanning electron microscope (SEM) images were used to obtain graphite flake length measurements and length distributions. Optical microscope images were inadequate since at magnifications where thin flakes were resolved, the images did not contain the entire flake.

Pearlite lamellae spacings were measured in some cases using a SEM and automated image analyzer (AIA). The number of intersections of a random line with the Fe_3C in the pearlite was determined. The pearlite spacing was calculated using the following formula:

$$Pearlite\ Spacing = \frac{1}{2 * P_L} \tag{7}$$

Gray Iron Eutectic Cell Count

Samples were etched in Stead's Reagent (100 ml of ethanol, 1 g $CuCl_2$, 4 g $MgCl_2$, and 2 ml of HCl) for 2.5 hours to reveal the eutectic cell boundaries. This procedure gave results with a high standard deviation, and an alternate procedure is being examined. The

alternate procedure involves heat treating the samples at 700°C for 8 hours to decompose pearlite in the eutectic cell centers. The pearlite at the cell boundaries is more stable due to the segregation of pearlite stabilizers to the boundaries during solidification.

Statistical Analysis of Microstructural Parameters

The microstructural parameters were statistically analyzed. The mean and sample standard deviation and the coefficient of variation (CV) were used to determine the accuracy and validity of measured microstructural parameters. The CV was calculated as follows:

$$CV = \frac{\sigma_{\overline{x}}}{\overline{x}} \tag{8}$$

where $\overline{x}$ is the average of the measured parameter and $\sigma\overline{x}$ is the standard error of the mean given as follows:

$$\sigma_{\overline{x}} = \frac{\sqrt{\frac{\Sigma(x_i - \overline{x})^2}{N-1}}}{\sqrt{N}} \tag{9}$$

For most features, measurements were made until the CV was approximately 0.05 which gave a 95% confidence. However, for the low volume percent phases such as MnS and TiX, unrealistic numbers (greater than 400) of fields were required to obtain 95% confidence. In these situations, simple T-tests were performed to determine if a statistically significant difference existed between samples.

Physical Properties

Characterization of the irons included other quantitative techniques such as density measurements and microcarbide analysis. The iron density is related to the volume fraction graphite in the iron and the weight of microcarbides in the pearlite. An increase in the density of iron can occur because of a decrease in the ratio of graphite to Fe_3C in the pearlite.

Density

Two methods were used to determine density. Volumetric density was calculated on machined samples for which the dimensions could be accurately measured and the weight easily determined. In such cases, density was determined by dividing the weight of the sample by its volume.

An immersion density technique was used on smaller, irregularly shaped specimens. The samples were weighed in air and in water. The displacement of water was determined from the buoyancy weight and the

31

volume determined from the volume of displaced water. The density was calculated using the above factors and accounting for atmospheric pressure, humidity, and temperature.

Theoretical Microcarbide Content

The equilibrium microcarbide concentration in irons with known compositions was determined in many cases using Thermocalc.[31] The solubility of carbon in austenite at the eutectic and eutectoid temperatures was calculated for each iron composition. The carbon solubility in austenite at the eutectoid temperature minus the carbon solubility in ferrite was divided by the carbon solubility in Fe_3C minus the carbon solubility in ferrite to provide a measure of the microcarbide weight percent. This calculation is shown in Equation 10.

$$MCWP = \frac{X - 0.02}{6.67 - 0.02} * 100 \qquad (10)$$

For example, in an iron containing 3.5% carbon and 2.25% silicon, the carbon solubility in austenite at the eutectoid is 0.651% and the equilibrium microcarbide weight percent in a pearlitic iron is 9.49%.

Mechanical Properties

Tensile tests were performed on tensile specimens machined from samples removed from the center of the test plates. Brinell hardness measurements were made on plates with plane and parallel surfaces. In addition, Brinell hardness maps were made of the plates using 60 measurements made on a one inch grid pattern.

The pearlite microhardness was measured to determine if a correlation could be found between pearlite hardness, microcarbide content, and the pearlite lamellar spacing. Pearlite microhardness was measured using a diamond indenter with a small load ($\leq$ 50g) to maintain a distance of three indention diameters from other microstructural features. Forty measurements were made on each sample. Significantly low values were removed from analysis since the indenter possibly encountered a graphite flake or nodule just below the polished surface.

RESULTS AND DISCUSSION

Gray Iron Plate Castings

Drill Life

Drill life determinations were made on eleven sets of gray iron plates submitted by sponsor foundries. The tool wear results obtained are summarized in Figure 9 where tool life is plotted as a function of drill speed in surface feet per minute (SFM). Wide ranges in drill life were seen depending on the type and source of iron and the drill speed.

Associated with each drill life curve is a foundry code, foundry melt practice, iron class, cooling condition, and two numbers such as 8.68/8.87. The number before the slash symbol indicates the weight percent microcarbides in a pearlitic iron as predicted by ThermoCalc, and the number after the slash indicates the experimentally determined weight percent microcarbides in the iron.

At a given drill speed, for example 130 SFM, approximately 535 holes were drilled in the Class 35 iron labeled G76 before a flank wear of 0.009 inch occurred. This iron contained an experimentally determined microcarbide weight percent (MCWP) of 8.87. The number of holes decreased to about 400 under the same conditions in the cupola-melted, Class 35 iron (G75) with a MCWP value of 9.62; 300 holes in the induction-melted, Class 35 iron (G73) with MCWP value of 10.53; 100 holes in the cupola-melted, Class 30 iron (G1) with a MCWP of 11.43; and 20 holes in the induction-melted, Class 40 sand cast gray iron (H8) and continuously cast gray iron (GS) with MCWP values of 11.13 and 14.44% respectively. In general, the tool life decreased at a constant drill speed as the MCWP increased.

Secondary effects, such as cooling rate on the run-out line, are also evident in the data. For example, G76 was a cupola-melted iron poured on a DISA line and cooled on the line for about 35 minutes before shakeout. G75 was the same iron that was held 17 minutes on the line before shakeout. About 30% more holes could be drilled at a drill speed of 130 SFM in the castings cooled for a longer time in the mold compared to the normally cooled iron. The faster cooling rate resulted in increased MCWP from 8.87 to 9.62.

An even greater difference can be seen in drill life in the induction-melted irons poured on the same line. About twice as many holes could be drilled before tool failure in the slowly cooled, induction-melted iron having a 35 minute run-out time in the mold compared to the normally cooled iron with an 18 minute run-out time. The microcarbide content was 10.68% in the more slowly cooled, induction-melted iron and 10.98% in the normally cooled, induction-melted iron.

These results might suggest that cupola melting produces a more machinable iron. However, results obtained on a Class 30, cupola-
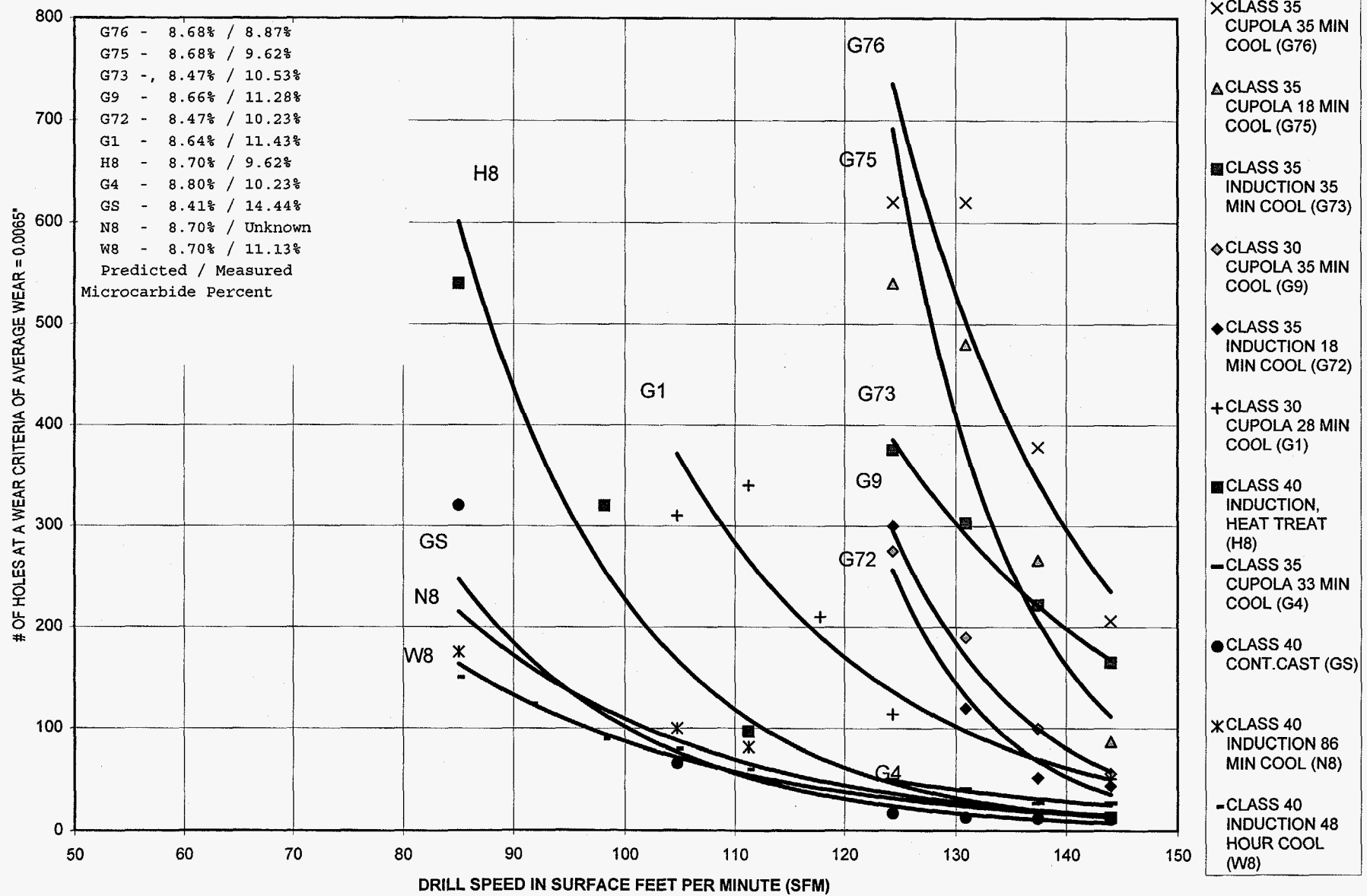
33

Figure 9. Tool Life Curves for HSS Drilling of Gray Cast Iron Plates (Number of Holes Drilled as a Function of Drill Speed).

melted iron labeled G1 indicates a lower machinability rating than the normally cooled Class 35, induction-melted iron labeled G72. Iron G1 was found to contain a rather high microcarbide weight percent of 11.43.

The tool life curves are replotted in Figure 10 as a function of weight percent microcarbide in the various irons. The three curves represent drill life at tool speeds of 124, 131, 137 and 144 surface feet per minute. Drill life progressively decreased as the microcarbide content increased. Above 11.5% by weight microcarbides, the drills exhibited a low life even at the lowest drilling speed. Additionally, as surface speed increased, tool life decreased. The equilibrium and measured microcarbide content for each set of test plates is listed in Table III. Larger deviations from the equilibrium microcarbide concentrations correlated with higher tool wear rates (lower tool life).

Microstructures

Representative etched and unetched micrographs of one of the drill plates tested for machinability are shown in Figures 11 through 13. The plate microstructures consisted principally of Type A graphite flakes in a fully pearlitic matrix. The microstructures were analyzed for MnS, TiX, and no correlation was found between the volume percent present and tool life.

Graphite Analysis. Graphite shape analyses were made to explore relations between surface area per volume of material (S_v) and flake length on machinability. High speed videos of iron being machined indicate that shearing occurs along and through the graphite flakes. It was thought that some relationship might be found between graphite shape factors amd tool life.

Graphite shape factor analysis and tool life results are illustrated in Figures 14 through 16. The tool life decreased as the average graphite flake length and maximum graphite flake length increased in the cupola melted irons. However, tool life increased with flake length in the induction melted irons.

The results obtained from the cupola and induction-melted irons produce opposite trends and cannot be rationalized at this time. No correlation between tool life and the graphite surface area per unit volume (S_v) or graphite mean spacing could be found in spite of the fact that the mean spacing should reflect the matrix shear distance associated with machining operations.

Mechanical Properties

Tensile and Compression Strength. The tensile strength of each set of iron plates submitted for analysis was determined. The tensile stress-strain curves are illustrated in Figure 17 and the correlation between tensile strength and tool life is illustrated in Figure 18. The raw data is presented in Table IV. In general, the tool life
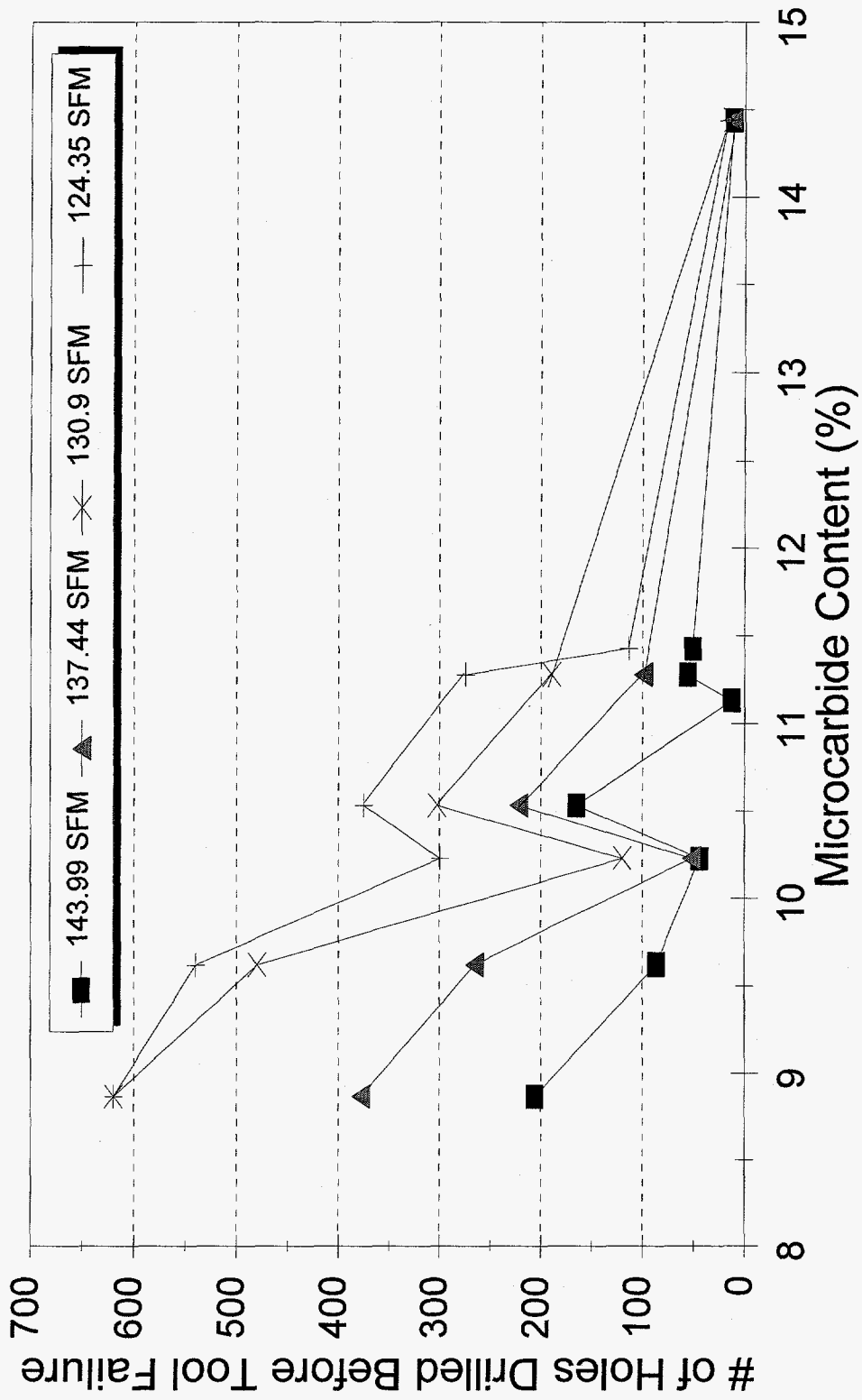
Figure 10. Effect of Microcarbide Content in Gray Iron on Tool Life.

Table III.

Measured Combined Carbon Percentage in Pearlite vs. Calculated Combined Carbon Percentage using ThermoCalc for Gray Iron Drill Plates

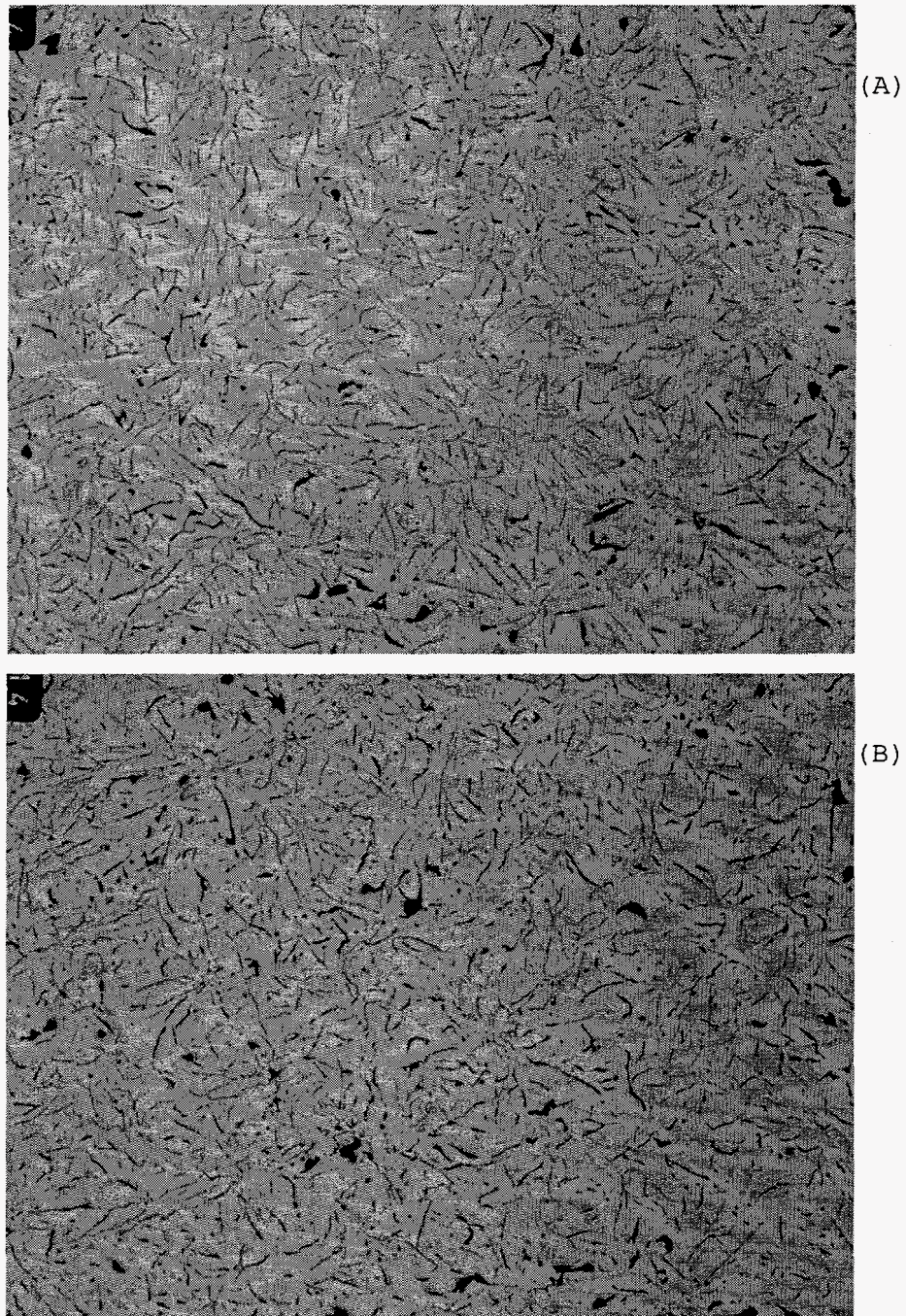| Sample	Predicted Tool Life at 124 sfm	Measured %Fe3C in Pearlite	Calculated %Fe3C (ThermoCalc) in Pearlite	Deviation of Measured %Fe3C to Calculated %Fe3C
G76	752	8.87	8.68	0.19
G75	687	9.62	8.68	0.95
G73	387	10.53	8.47	2.06
G72	261	10.23	8.47	1.76
G9	275	11.28	8.66	2.62
G1	131	11.43	8.64	2.79
G4	50	10.23	8.80	1.43
G8	35	11.13	8.70	2.43
H8		9.62	8.70	0.92
GS	21	14.44	8.41	6.03

(A)

(B)

Figure 11. Representative Unetched Microstructures
            of a (A) High Tool Life Gray Iron (G76)
            and (B) a Low Tool Life Iron (G8). 30X.

(A)
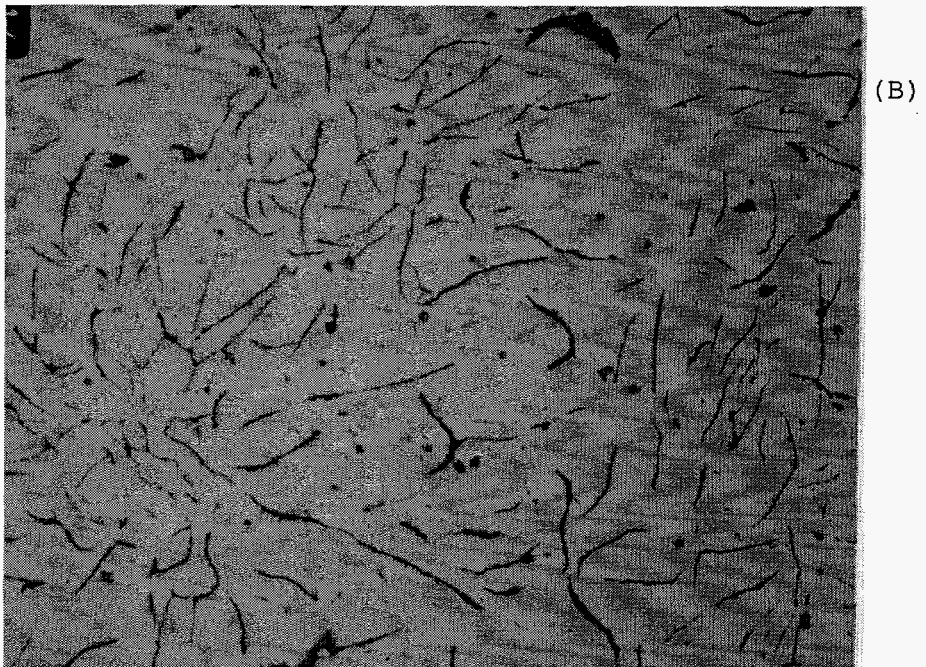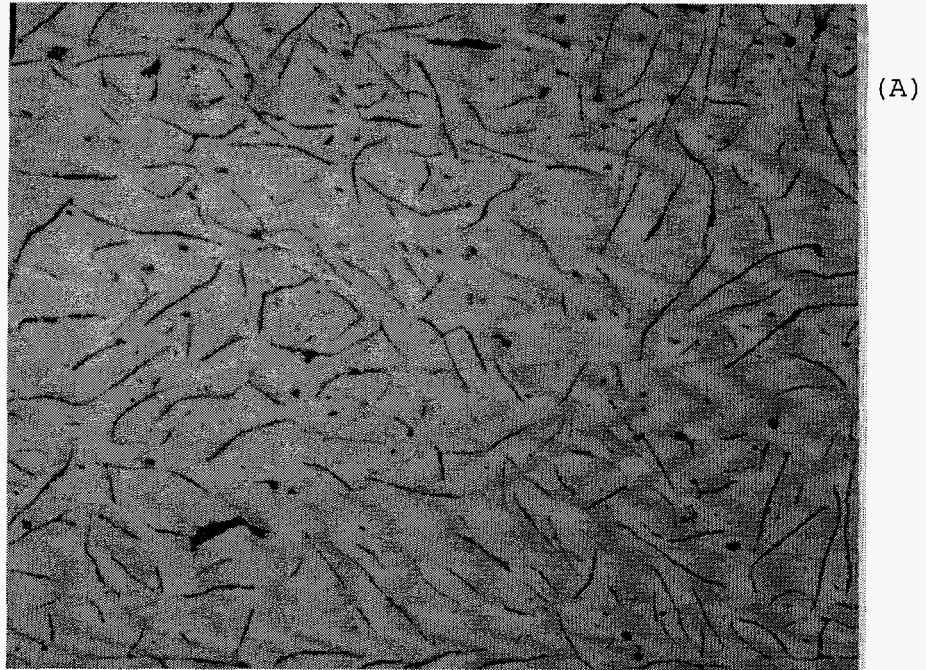
(B)

Figure 12.   Representative Unetched Microstructures
            of a (A) High Tool Life Gray Iron (G76)
            and (B) a Low Tool Life Iron (G8).   100X.
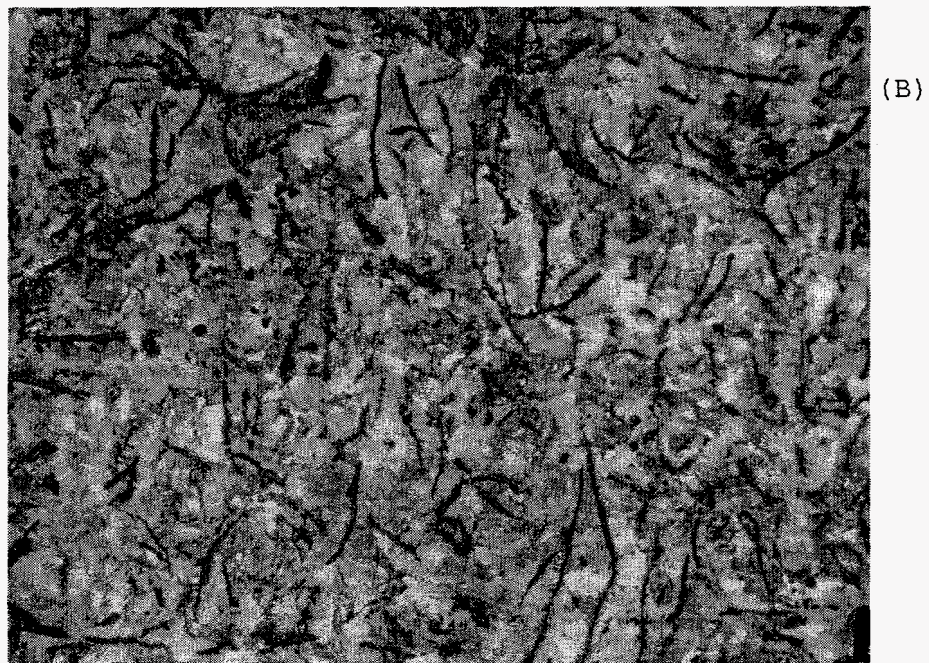
(A)

(B)

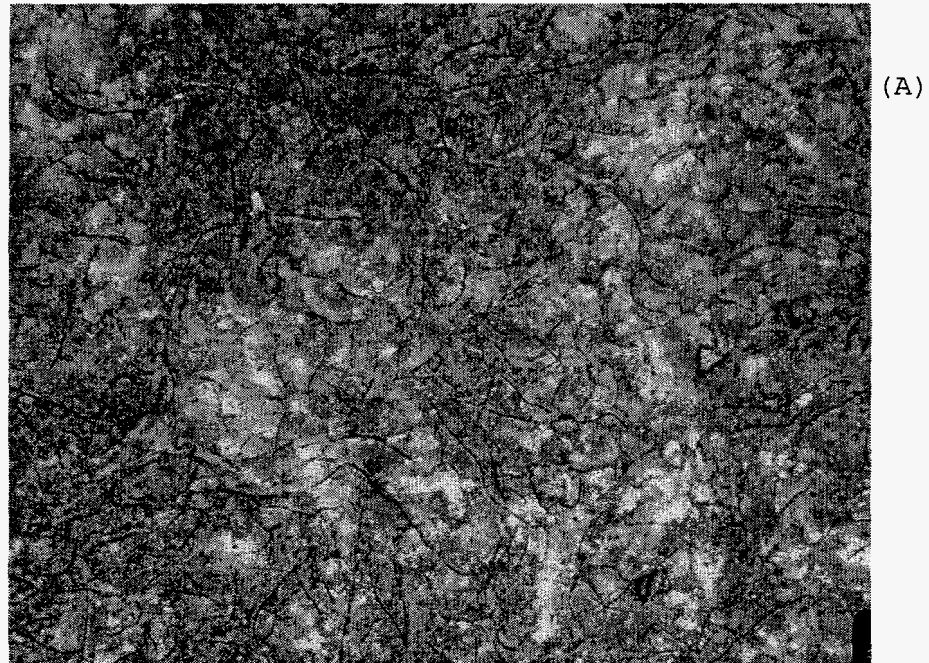Figure 13. Representative Etched Microstructures of
            a (A) High Tool Life Gray Iron (G76) and
            (B) a Low Tool Life Iron (G8). 100X,
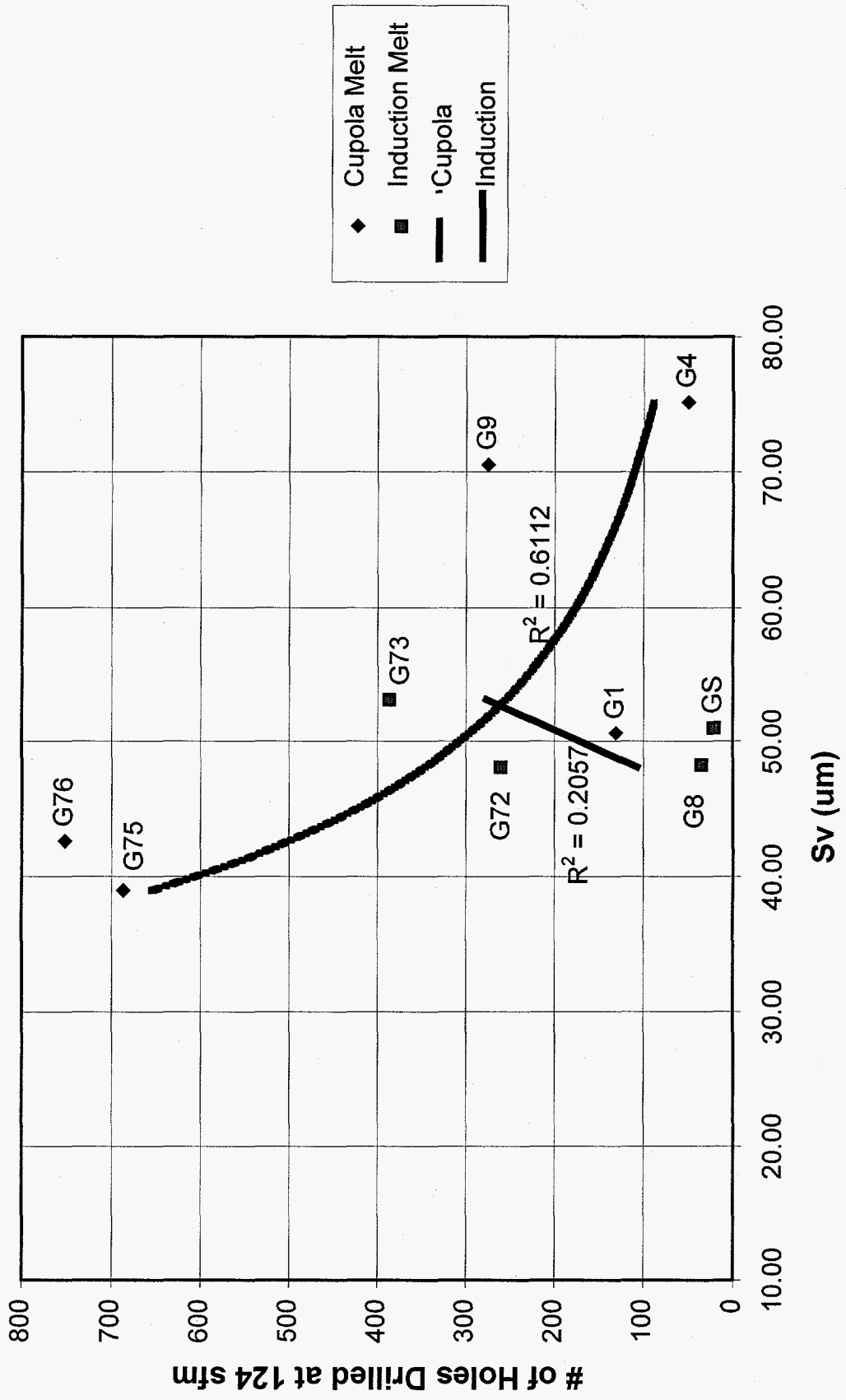   Nital.

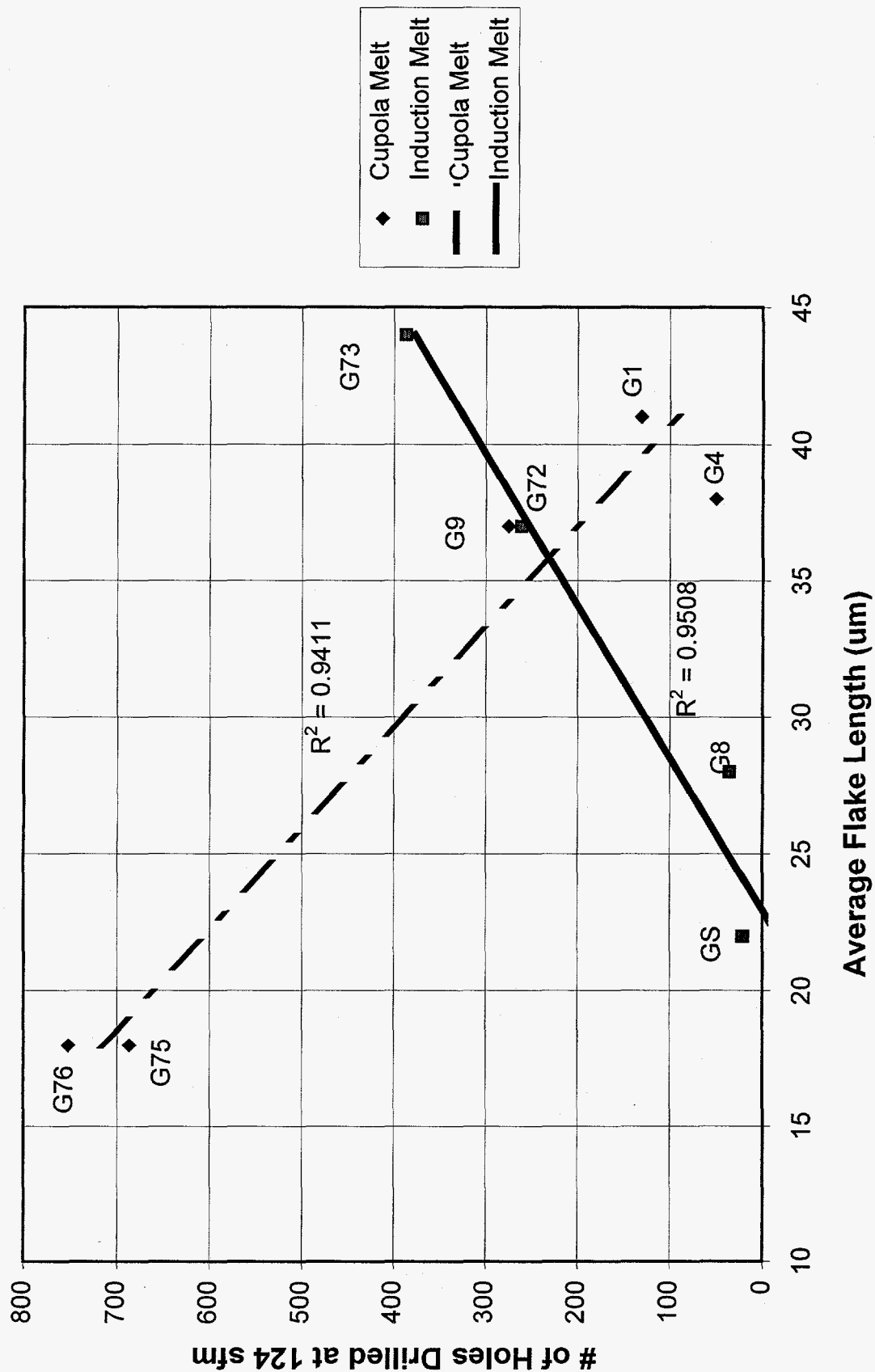Figure 14. Tool life versus Sv in Gray Iron Drill Plates

Figure 15. Tool Life versus Average Flake Length in Gray Iron Drill Plates
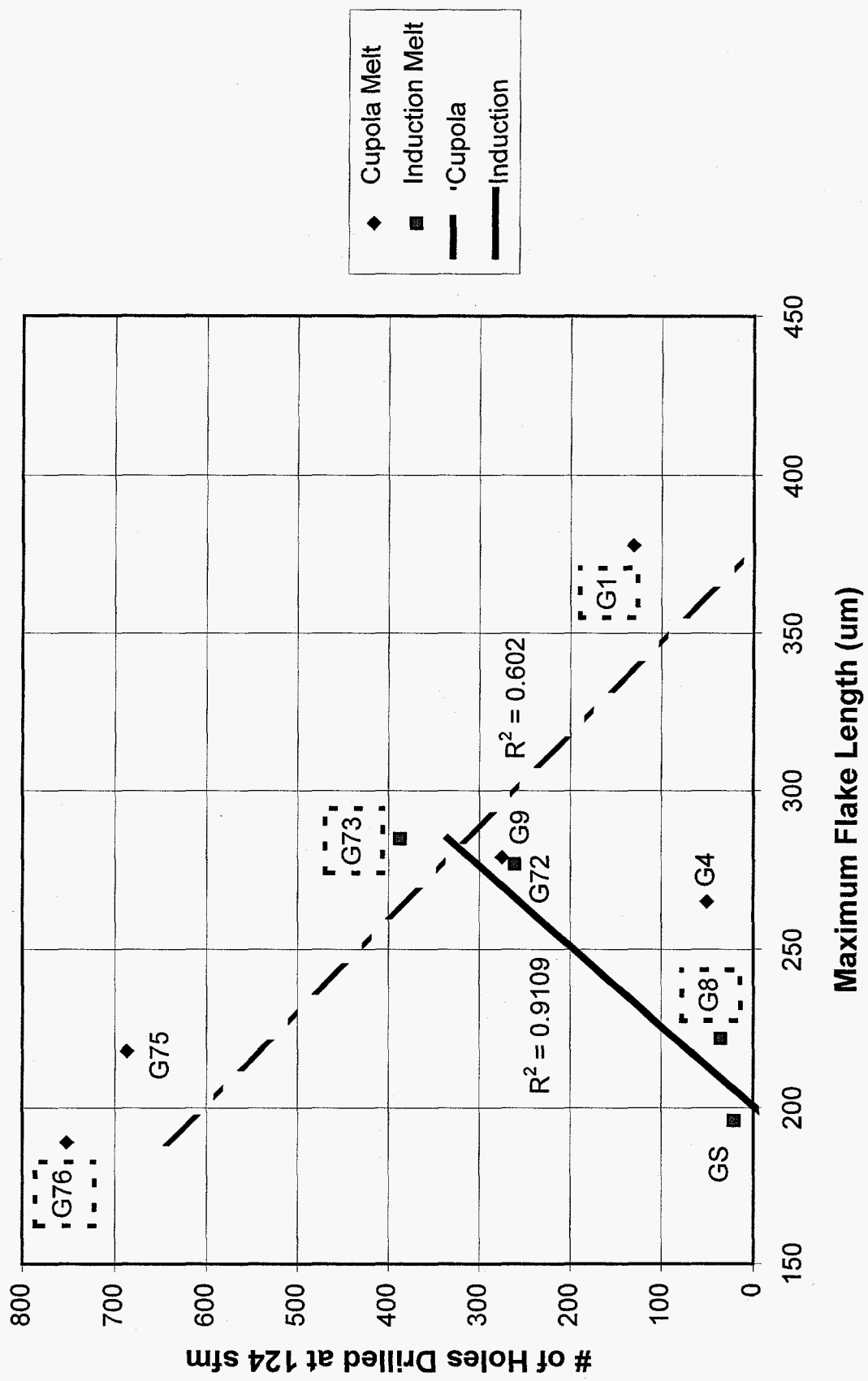
Figure 16. Tool Life versus Maximum Flake Length in Gray Iron Drill Plates.
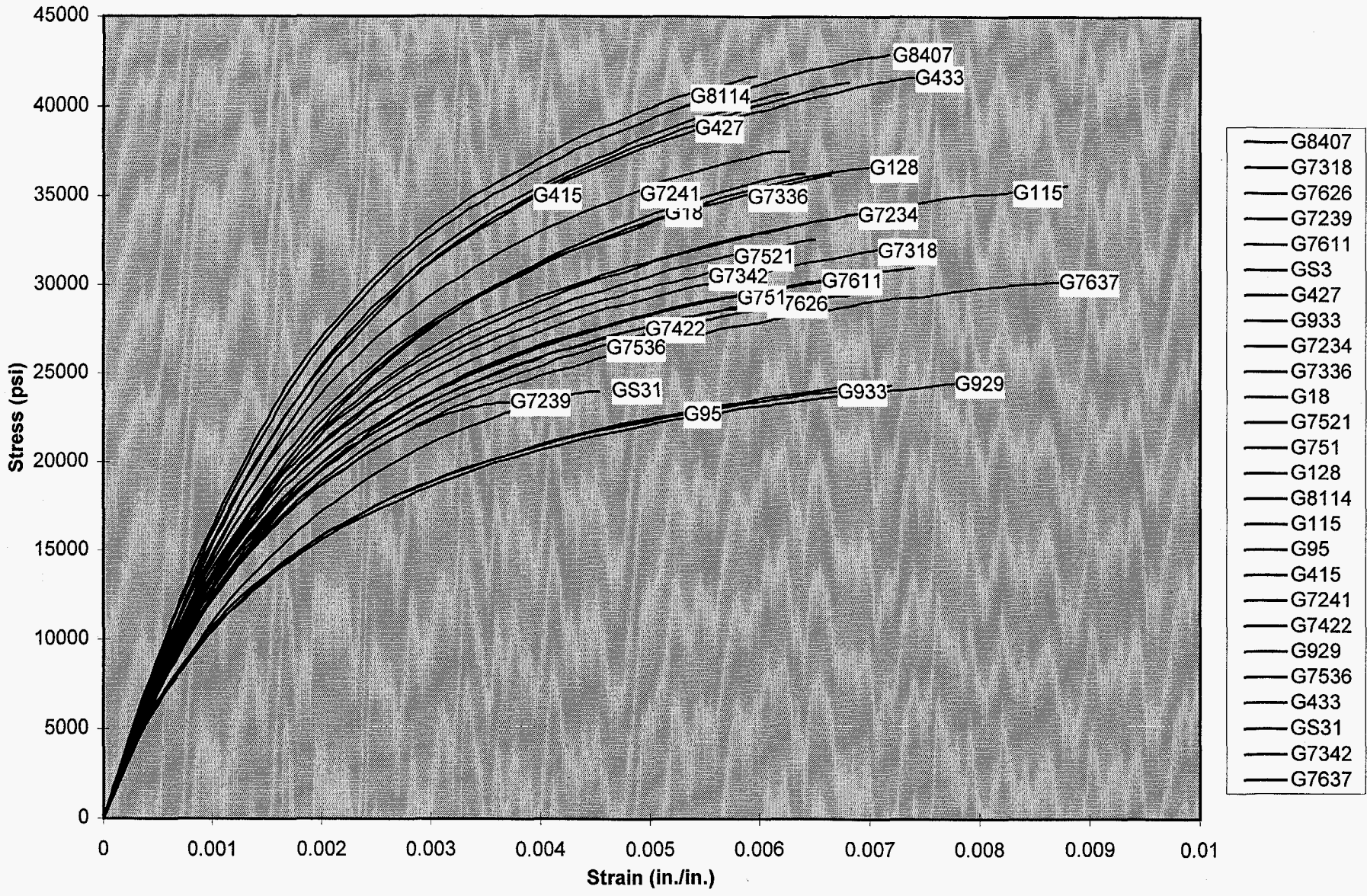
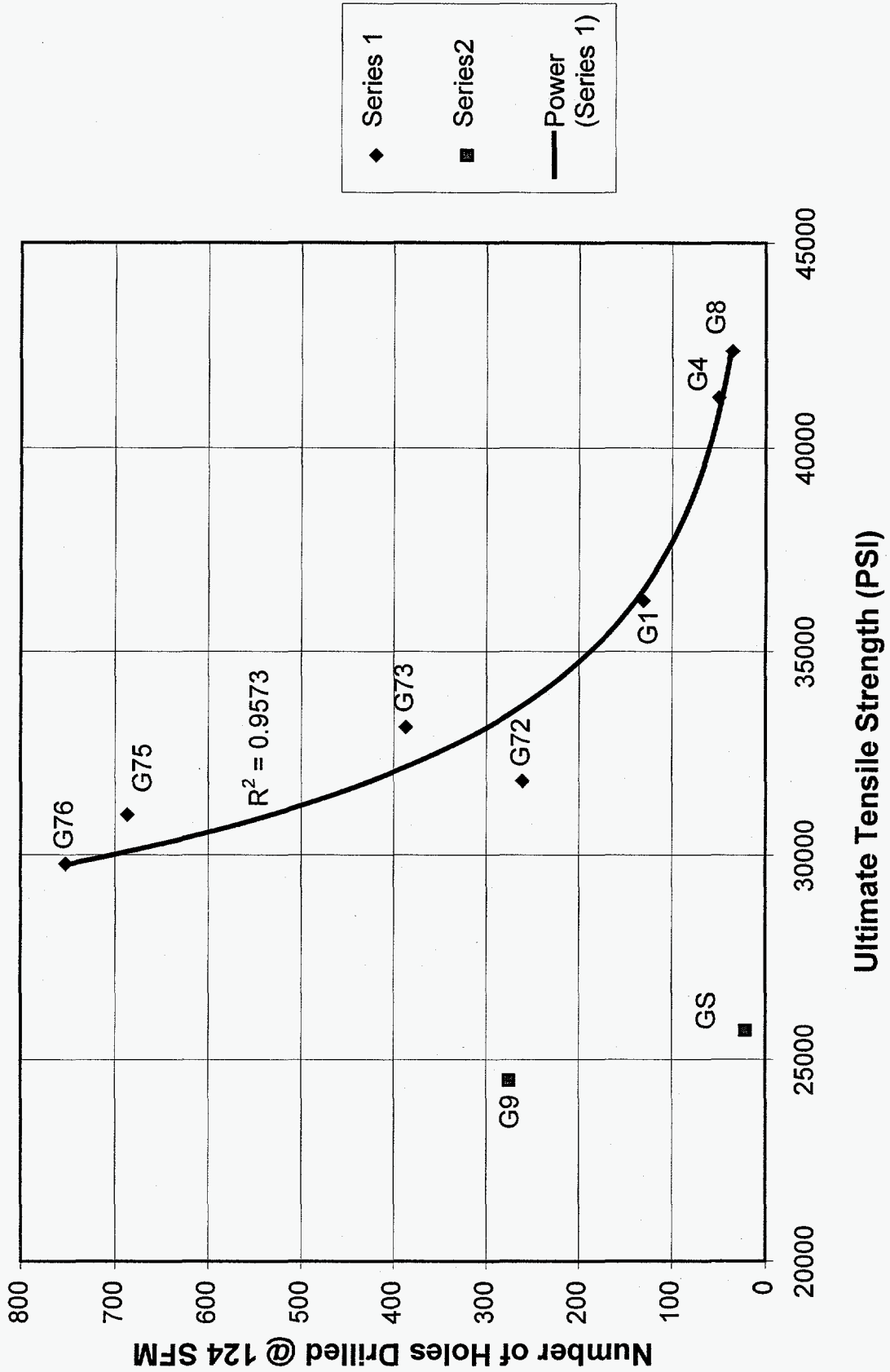Figure 17. Tensile Stress-Strain Responses of Gray Iron Drill Plates.

44

Figure 18. Tool Life versus Tensile Strength in the Gray Iron Drill Plates.

Table IV.

Tensile Properties from the Gray Iron Drill Plates.

| Sample I.D.	Remarks	Tool Life @ 124 sfm	Load Rate psi/m	Ultimate Strength psi	Ult. @ .2% Strength psi	0.2% Yield Strength psi	Int. Elastic Modulus 10^6 psi.	Total Strain in./in.	Measured Microcarbide Content (wt.%)
G7611	Class 35	752	10K	30200	25750	19850	15.33	0.0066	8.87
G7626	Cupola Melt		10K	29000	24900	18500	16	0.0063	
G7637	Slow Cool		10K	30150	24000	18850	14.49	0.0092	
			Average	29783	24883	19067	15.27	0.0074	
			Std Dev	679	875	701	0.76	0.0016	
G751	Class 35	687	10K	30950	25950	19950	14.83	0.0074	9.62
G7521	Cupola Melt		10K	32500	27650	21000	16.27	0.0065	
G7536	Normal Cool		10K	29500	24700	19000	14.92	0.0068	
			Average	30983	26100	19983	15.34	0.0069	
			Std Dev	1500	1481	1000	0.81	0.0005	
G7318	Class 35	387	10K	32500	26600	20600	16.1	0.0076	10.53
G7336	Induction Melt		10K	36200	30350	22800	17.51	0.0067	
G7342	Slow Cool		10K	30767	26800	20900	16.87	0.0059	
			Average	33156	27917	21433	16.83	0.0067	
			Std Dev	2775	2110	1193	0.71	0.0009	
G929	Class 30	275	10K	24750	19650	15650	14	0.008	11.28
G933	Cupola Melt		10K	24450	19550	15900	15.15	0.0072	
G95	Normal Cool		10K	24250	19400	15750	15.82	0.0071	
			Average	24483	19533	15767	14.99	0.0074	
			Std Dev	252	126	126	0.92	0.0005	
G7234	Class 35	261	10K	34500	28450	22000	17.31	0.0074	10.23
G7239	Induction Melt		10K	23350	23350	13650	14.29	0.0038	
G7241	Normal Cool		10K	37600	32500	23850	17.82	0.0063	
			Average	31817	28100	19833	16.47	0.0058	
			Std Dev	7494	4585	5434	1.91	0.0018	
G115	Class 30	131	10K	35600	28650	21300	15.71	0.0088	11.43
G128	Cupola Melt		10K	36800	31500	22400	14.88	0.0071	
G18	Normal Cool		10K	36350	31700	22100	15.08	0.0064	
			Average	36250	30617	21933	15.22	0.0074	
			Std Dev	606	1706	569	0.43	0.0012	
G415	Class 35	50	10K	40750	36250	25500	16.13	0.0062	9.62
G427	Cupola Melt		10K	41350	36350	24850	15.6	0.0068	
G433	Normal Cool		10K	41550	35000	25350	17.58	0.0074	
			Average	41217	35867	25233	16.44	0.0068	
			Std Dev	416	752	340	1.03	0.0006	
G8114	Class 40	35	10K	41700	37500	27150	18	0.006	11.13
G8320	Induction Melt		10K	43500	37100	27100	18.56	0.0072	
G8407	Normal Cool		10K	43000	36850	28650	17.65	0.0072	
			Average	42733	37150	27633	18.07	0.0068	
			Std Dev	929	328	881	0.46	0.0007	
GS2	Class 40	21	10K	23800	22700	16600	11.7	0.0046	
GS3	Induction Melt		10K	27700	25900	18500	15.18	0.0047	14.44
GS31	Fast Cool		10K	23740	22600	17100	13.39	0.0046	
			Average	25720	24250	17800	14	0.0047	
			Std Dev	2800	2333	990	1.27	0.0001	
G7422	Cupola Melt		10K	28850	25450	19500	14.26	0.0061	
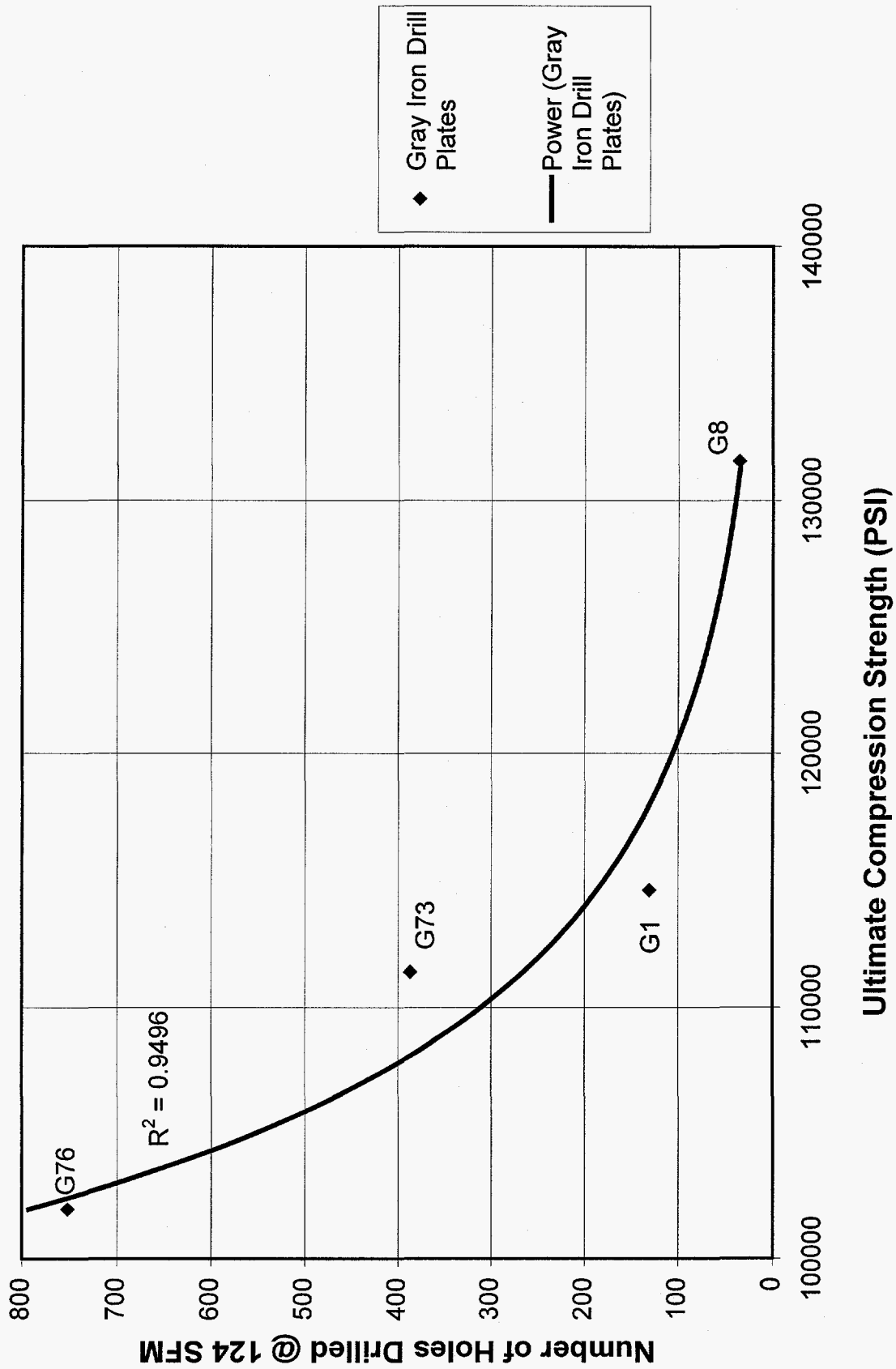
Figure 19. Tool Life versus Compression Strength in the Gray Iron Drill Plates.
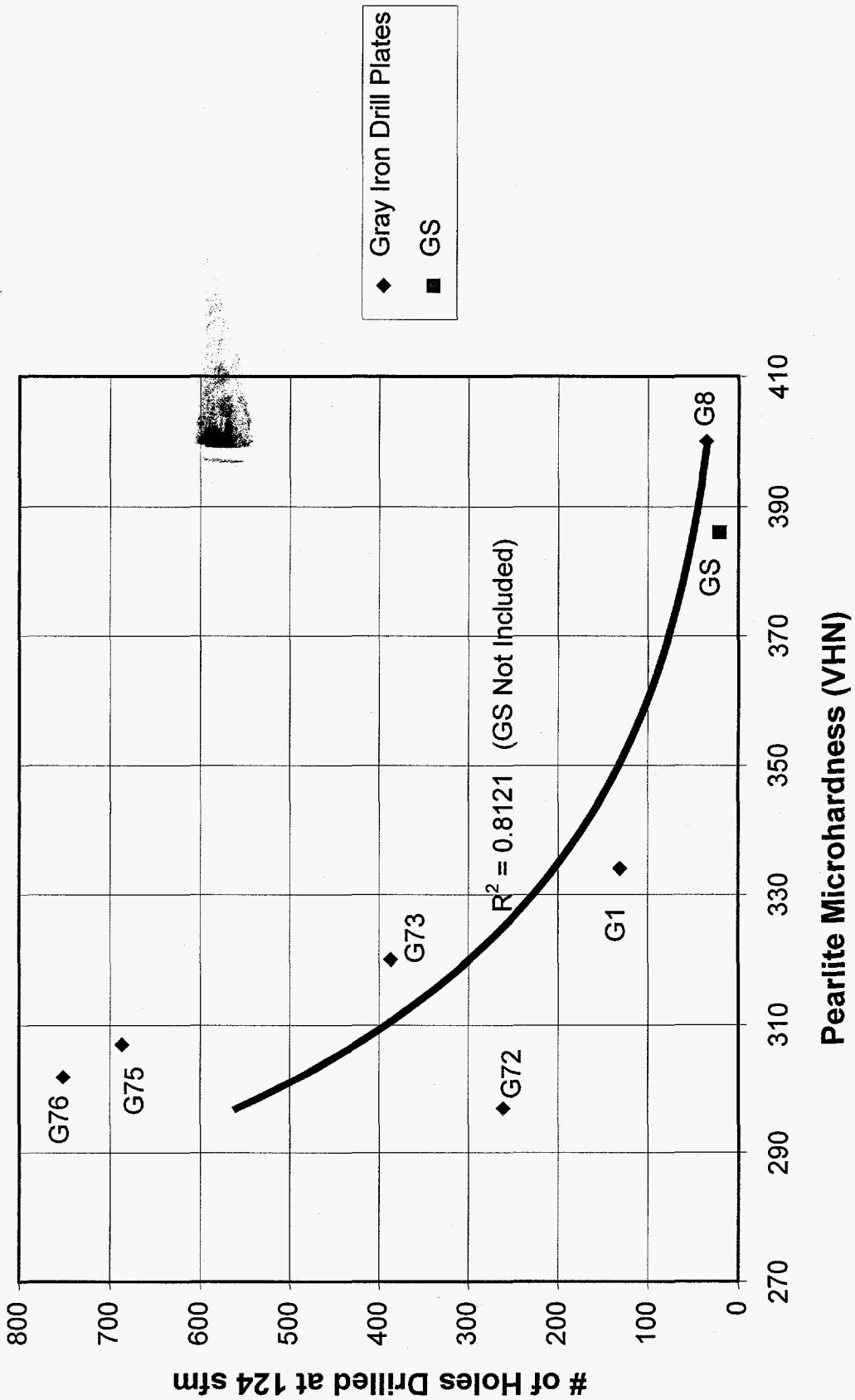
Figure 20. Tool Life versus Pearlite Microhardness in Gray Iron Drill Plates.

Table V.

Pearlite Microhardness of the Gray Iron Test Plates

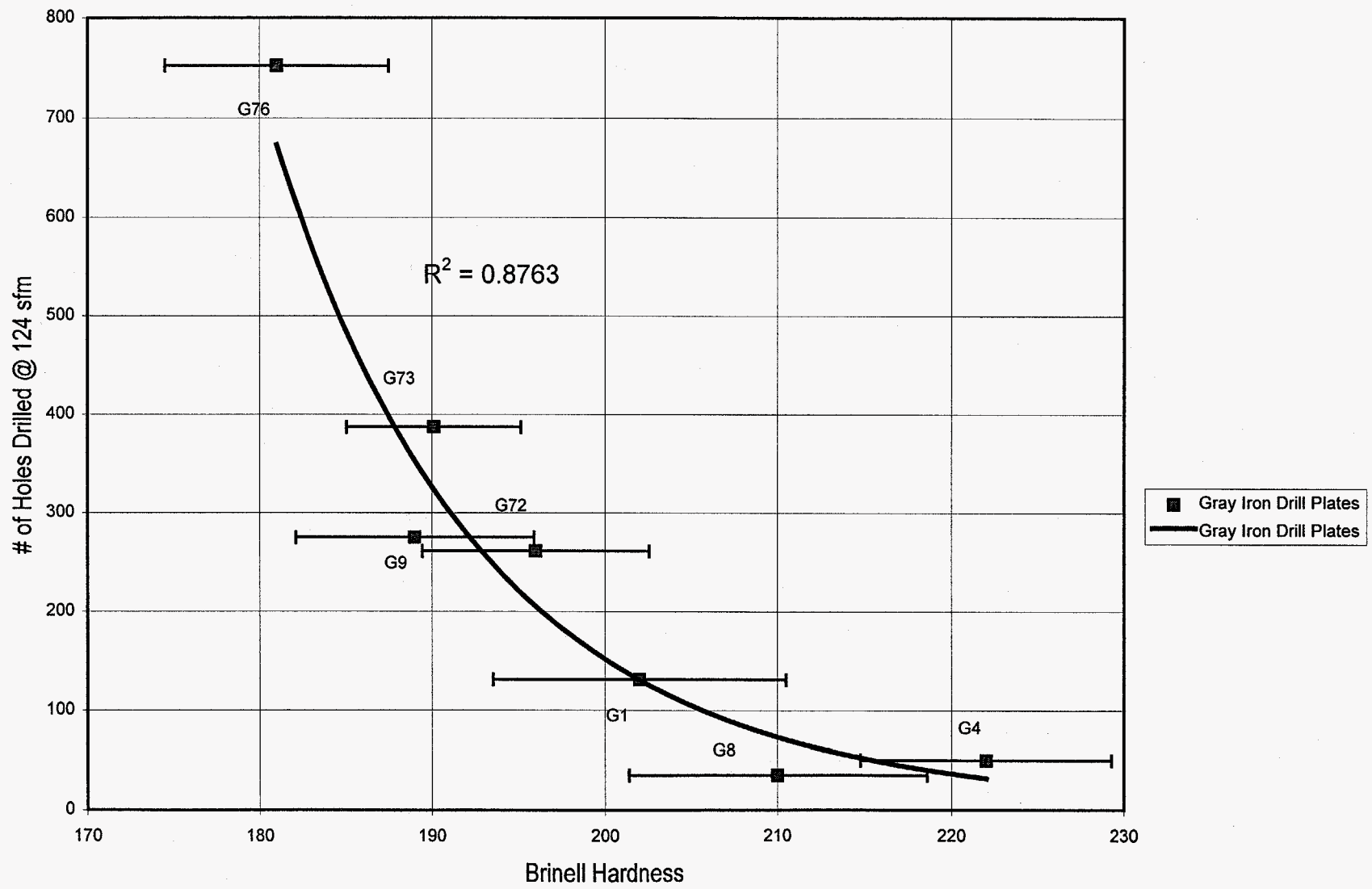| Sample	Iron Class	Melt Process	Shake-Out Time	Tool Life @ 124 sfm	Pearlite Microhardness	Standard Deviation	C.V.
G76	35	Cupola	35 min.	752	302	24	0.08
G75	35	Cupola	18 min.	687	307	18	0.06
G73	35	Induction	35 min.	387	320	16	0.05
G72	35	Induction	18 min.	261	297	19	0.06
G1	30	Cupola	28 min.	131	334	41	0.12
G8	40	Induction	48 hr.	35	400	47	0.12
GS	40	Induction	Fast	21	386	20	0.05

Figure 21.   Tool Life versus Brinell Hardness in Gray Iron Drill Plates (Results from Hardness Maps).

decreased with tensile strength, but two data points fell significantly off the trend line. Both of these irons contained graphite flakes that were significantly longer than present in the other irons, and the longer flakes caused tensile failure at lower stress level. In spite of the lower strength, the irons produced relatively high tool wear rates because of the microcarbide contents of 11.28 and 14.44% respectively.

Preliminary results from compression tests show a correlation between compression strength and measured tool life as illustrated in Figure 19. The data points illustrated in Figure 19 are for cupola and induction-melted irons where no correlations could be found between microstructural features and tool life. There is a good correlation between compression fracture stress and tool life, and this material evaluation procedure may provide a convenient method of predicting tool life from a relatively simple test that can be run in a foundry. Additional experiments are underway to evaluate more irons and verify the correlation.

Hardness Results. The pearlite microhardness results are illustrated in Figure 20, and the raw data are presented in Table V. As the pearlite microhardness increased, the tool life generally decreased. The pearlite microhardness results appear to mirror the pearlite microcarbide content in the castings, but there is considerable scatter in the data. Additional procedural details must be developed to reduce the data scatter, but in general, plates with better machinability contained fewer microcarbides and a lower pearlite microhardness.

The tool life also decreased as the Brinell hardness increased. The Brinell hardness results are shown in Figure 21. The results of the Brinell hardness measurements mirrored the microhardness and pearlite microcarbide measurements.

Commercial Gray Iron Castings

Four sets of "acceptable" and "hard-to-machine" gray iron commercial castings were submitted by sponsor companies. The castings were reported to be "hard-to-machine" by commercial machine shops, but the degree was subjective. For each pair of "acceptable" and "hard-to-machine" castings, the microcarbide weight percent was greater in the "hard-to-machine" castings.

The results of the microcarbide analysis are presented in Tables VI-IX for disc hubs, cylinder bores in diesel blocks, diesel heads, and brake rotors, respectively. In each case, ThermoCalc was used to predict the equilibrium microcarbide percent assuming a fully pearlitic microstructure. This calculation was made based on the actual carbon and silicon concentrations and both major elements and minor elements present in each iron. The predicted microcarbide content is followed by an experimentally determined microcarbide concentration.

TABLE VI

**CORRELATION BETWEEN SUBJECTIVE MACHINABILITY RATINGS ON DISC BRAKE HUBS
AND EXPERIMENTALLY DETERMINED MICROCARBIDE CONTENTS IN THE CASTINGS**

(Tool Material not Known for Certain but Thought to be Carbide)

UAB SAMPLE NUMBER	MACHINABILITY AND PROCESS DESCRIPTORS	COMPOSITION C (%)	Si (%)	PREDICTED MICRO-CARBIDE WT (%)	EXPERIMENTAL MICRO CARBIDE WT (%)
CIP-22-2G	"Acceptable" Machinability Heat Date 1425 Bored Surface	3.52	2.17	8.60	9.47
CIP-22-2G	"Acceptable" Machinability Heat Date 1425 Faced Surface	3.53	2.15	8.64	10.53
CIP-22-1P	"Hard-to-Machine" Heat Date 3205 Bored Surface	3.53	2.23	8.54	13.23
CIP-22-1P	"Hard-to-Machine" Heat Date 3205 Faced Surface	3.54	2.22	8.60	13.68

52

TABLE VII

CORRELATION BETWEEN SUBJECTIVE MACHINABILITY RATINGS FROM CBN TOOLS USED ON BORED CYLINDER BLOCKS AND EXPERIMENTALLY DETERMINED MICROCARBIDE CONTENTS IN THE CASTINGS

(Blocks were machined with CBN inserts)

UAB SAMPLE NUMBER	MACHINABILITY AND PROCESS DESCRIPTORS	COMPOSITION		PREDICTED MICRO-CARBIDE WT (%)	EXPERIMENTAL MICROCARBIDE WT (%)
		C (%)	Si (%)		
CIP-13-TSR3	Foundry B Cylinder Bore #403, Semi-Rough Finish, "Acceptable" Machinability	3.34	2.15"	7.89	9.92
CIP-18-NTC1	Foundry A Cylinder Bore #403 with Foundry B chemistry "Acceptable" Machinability	3.42	2.25	7.98	9.62
CIP-13-NSR3	Foundry A Cylinder Bore #403 with August Chemistry, Semi-Rough Finish, "Marginal" Machinability	3.40	1.88	8.47	11.13
CIP-18-NFC2	Foundry A Cylinder Bore with February Chemistry, "Poor" Machinability	3.41	2.01	8.41	10.98
CIP-23	Foundry A Heads, "Broke Drills Left & Right"	3.39	2.03	8.15	12.6

53

TABLE VIII

CORRELATION BETWEEN SUBJECTIVE MACHINABILITY RATINGS OBERVED DURING DRILLING OF CLASS 40 GRAY IRON HEADS AND EXPERIMENTALLY DETERMINED MICROCARBIDES IN THE CASTINGS

(Blocks were drilled using high speed drills)

UAB SAMPLE NUMBER	MACHINABILITY AND PROCESS DESCRIPTORS	COMPOSITION C(%)	Si(%)	PREDICTED MICRO-CARBIDE WT (%)	EXPERIMENTAL MICROCARBIDE WT (%)
G8H-2-B	"Acceptable" Green Sand Mold "Thin" Section	3.28	2.08	9.53	9.62
G8H-5-B	"Acceptable" Green Sand Mold "Thin" Section	3.24	2.15	9.52	9.47
G8E-8-B	"Hard-to-Machine" January No-Bake "Thin" Section	3.24	2.03	9.54	10.23
G8E-9-B	"Hard-to-Machine" January No-Bake "Thin" Section	3.23	2.06	9.53	11.13
G8H-5-203	"Acceptable" Green Sand Mold "Thick" Section	3.24	2.15	9.52	9.77
G8H-5-205	"Acceptable" Green Sand Mold "Thick" Section	3.24	2.15	9.52	11.13
G8E-9-203	"Hard-to-Machine" January No-Bake "Thick" Section	3.23	2.06	9.53	12.03
G8E-9-205	"Hard-to-Machine" January No-Bake "Thick" Section	3.23	2.06	9.53	12.63

TABLE IX

**CORRELATION BETWEEN SUBJECTIVE MACHINABILITY RATINGS ON BRAKE ROTORS
AND EXPERIMENTALLY DETERMINED MICROCARBIDE CONTENTS IN THE CASTINGS**

UAB SAMPLE NUMBER	MACHINABILITY AND PROCESS DESCRIPTORS	COMPOSITION C (%)	Si (%)	PREDICTED MICRO-CARBIDE WT (%)	EXPERIMENTAL MICROCARBIDE WT (%)
CIP-29-A6	"Acceptable" Machinability Cupola Melt	3.47	2.14	----	10.98
CIP-29-AB	"Hard-to-Machine" Induction Melt	3.39	2.14	----	11.73

ThermoCalc predicted an equilibrium carbide weight percent of 8.54 to 8.64 in the hub irons as presented in Table VI. The weight percent microcarbides in the irons considered to have acceptable machinability ranged from 9.47 to 10.53. The weight percent of microcarbides in the irons considered to have poor machinability ranged from 13.23 to 13.68.

Similar data on diesel blocks being machined with CBN inserts and one cylinder head are presented in Table VII. The first iron composition was for a Foundry B cylinder bore containing 3.34% carbon and 2.15% silicon. These cylinder blocks had an "acceptable" machinability. The predicted microcarbide content was 7.89%, and the measured microcarbide content was 9.92%.

The second iron composition was from a Foundry A cylinder bore made with a Foundry B composition containing 3.42% carbon and 2.25% silicon. Cylinder blocks with this iron composition had "acceptable" machinability. The predicted carbide weight percent was 7.98, and the actual microcarbide weight percent was 9.62.

The third and fourth irons were poured at Foundry A and made with "normal" chemistry in August and February 1995, respectively. These irons contained carbon in the range of 3.40 to 3.41% and silicon in the range of 1.88 to 2.01%. Cylinder blocks with this chemistry had "marginal" to "poor" machinability rating. The predicted microcarbide weight percent was 8.47, but the actual microcarbide weight percent ranged from 10.98 to 11.13.

The last entry in Table VII is for a diesel head produced at Foundry A that "broke drills left and right" at the machine shop. This iron contained 3.39% carbon and 2.03% silicon. The iron was expected to contain about 8.15% microcarbides at equilibrium but was observed to contain the highest microcarbide content of any of these irons at 12.6%.

The results obtained on several cylinder heads from another foundry are presented in Table VIII. These irons contained 3.23 to 3.28% carbon and 2.03 to 2.15% silicon. These castings were poured from the same type of iron to produce the same head in the same foundry using both no-bake and green sand casting processes. Two regions of each casting were examined. The "thin" section was about 1" thick and the "thick" section was about 4" thick.

ThermoCalc predicted an equilibrium microcarbide weight percent based on the metal compositions of about 9.52 to 9.53% in both the green sand and the no-bake castings having acceptable machinability. The weight percent microcarbides in the thin sections considered to have acceptable machinability ranged from 9.47 to 9.62%. The weight percent microcarbides in thin section no-bake castings considered to have poor machinability was in the range of 10.23 to 11.13%.

The weight percent microcarbides in thick sections considered to have acceptable machinability ranged from 9.77 to 11.13%. The weight

percent microcarbides found in the thick sections of castings considered to be "hard-to-machine" ranged from 12.03 to 12.63. In all cases, the poorly machinable irons contained a higher concentration of microcarbides than the companion irons with acceptable machinability.

Results obtained on two solid (uncored) brake rotors from batches having acceptable and unacceptable machinability when machined with CBN inserts is presented in Table IX. Both irons were cast in the same foundry. The iron with acceptable machinability contained 10.98% microcarbides and the iron with unacceptable machinability contained 11.73% microcarbides.

Force Measurements

Exploratory studies were performed to determine if force measurements made on tools used to machine cast iron might be used to predict tool life. Torque and feed forces were observed to correlate to machinability. The goal of these torque and force measurements is to develop a procedure to provide a "quick" indication of tool life without having to develop a complete tool life curve.

Chip Formation

Machining and the process of chip formation in gray cast iron is quite different from most other metals. The iron characteristics which cause the differences are the low fracture strain and the non-linear stress-strain response. Both characteristics are the result of the graphite flakes which serve as discontinuities and stress intensifiers. The discontinuities redistribute localized strains and produce the non-linear stress-strain response characteristic of iron. The tips of each graphite flake serve as stress intensifiers which result in plastic deformation and cracking of the matrix at low bulk stresses. These built-in "flaws" cause the fracture path in cast iron to not follow the principal stress plane.

The fact that the fracture path in cast iron does not follow the principal stress planes is clearly evident in machining videos developed by G. Wamecke in 1976.(32) The video micrographs show fracturing of cast iron ahead of the cutting tool along graphite flakes and through the matrix between the graphite flakes. The chips appear to be randomly sized depending on the orientation and size of the graphite flakes. The chips fracture from the workpiece and are ejected by the tool rake face. Observations about metal flow, fracture, and chip formation made from the video at various machining speeds provided the basis for a model to analyze the forces exerted during cast iron boring and drilling operations.

The purpose of the model is to describe the energy distribution associated with machining. The energy associated with machining is distributed into 1) metal shear energy (strain energy), 2) rake face frictional energy (heat), and 3) flank face frictional energy (heat) as illustrated in Figure 22. In general, the total energy associated with shear and both rake face and flank face friction are distributed
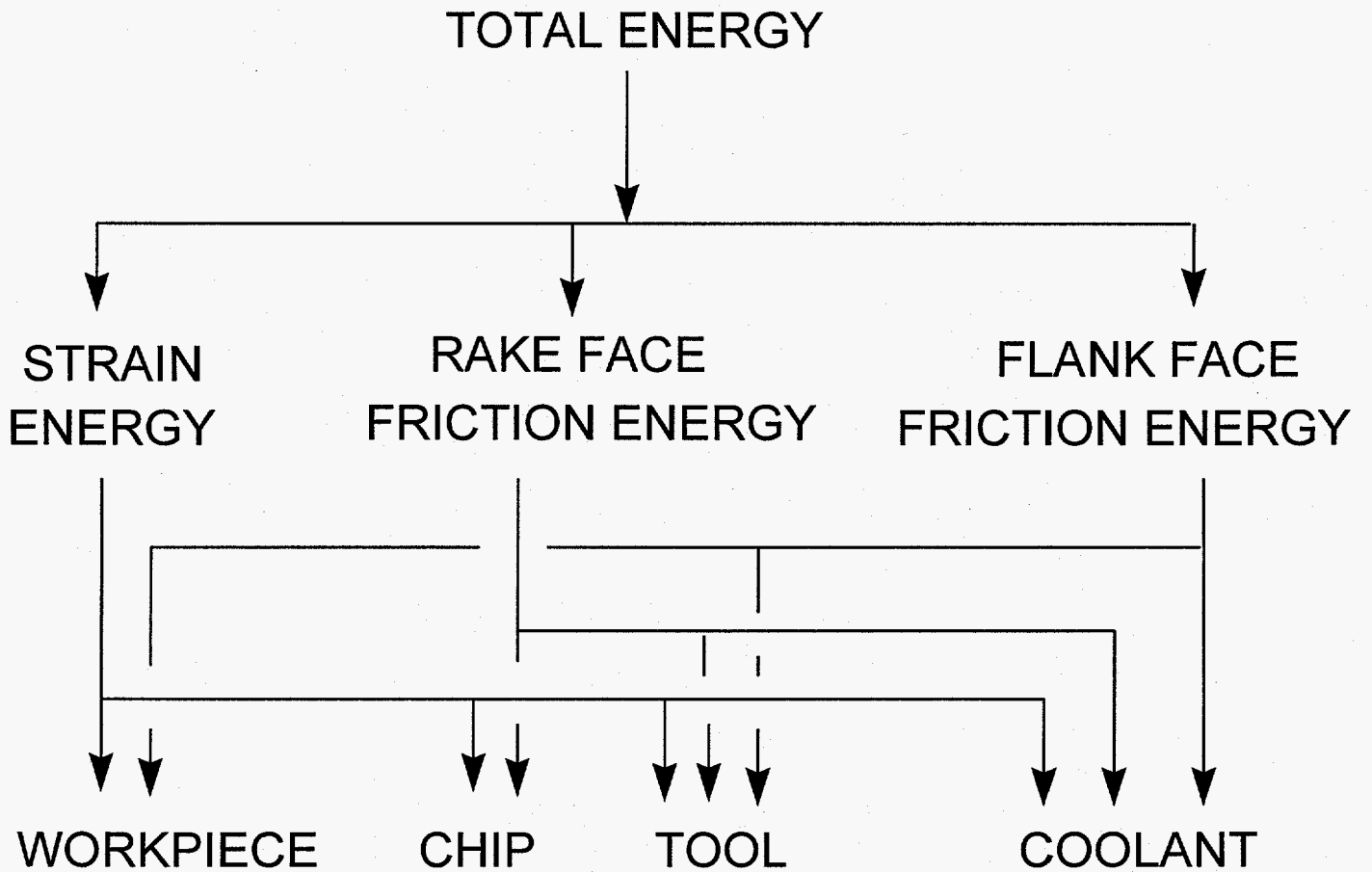
57

TOTAL ENERGY

STRAIN ENERGY

RAKE FACE FRICTION ENERGY

FLANK FACE FRICTION ENERGY

WORKPIECE   CHIP   TOOL   COOLANT

Figure 22.   Energy Distribution in Machining.

58

into the 1) workpiece, 2) chip, 3) tool, and 4) coolant. However, no coolant is being used in UAB machining experiments so no coolant energy absorption occurs.

The experimental technique for making measurements in boring and drilling experiments is illustrated in Figure 23. In this apparatus, the tool, either a drill or a boring bar is mounted in a CNC mill and enters the workpiece from above. The workpiece is a plate if a drill test is being performed or hollow cylinder if a boring test is being performed. The workpiece is mounted on a multiaxis dynamometer that permits forces in various directions to be measured. In this case, there are thrust (Fz), torque, and forces in both the X and Y directions (Fx and Fy, respectively). In most machining operations, these four forces exist, but analyzing data from such a system is complex.

A simpler system for analysis is illustrated in Figure 24. This arrangement consists of a tool making an orthogonal cut in a workpiece. A dynamometer is located underneath the workpiece (not illustrated in Figure 24) that measures the cutting force (Fc) and the feed force (F_T). This type of system is commonly referred to as a two-force system, and such a system can be approximated in boring by using a small depth of cut compared to the width of the cut. The orthogonal analysis allows classical equations to be used to separate the energy distribution into various components.

A magnified view of the tool tip, chip, shear zone between the workpiece and the chip, workpiece, and the compression zone in the workpiece is illustrated in Figure 25. Some minimum depth of penetration into the workpiece is required to form a chip. If the penetration is inadequate, no chip is formed, and the energy is distributed between the tool as heat and the workpiece as strain energy and heat.

The situation involving inadequate tool penetration to form a chip is illustrated in Figure 26. If a chip is formed, energy goes into the shear zone between the workpiece and chip as illustrated in Figure 25.

Before the energy contributions can be determined, force-time data taken with a dynamometer must be interpreted. An actual torque-time curve obtained while boring a cast iron cylinder is illustrated in Figure 27. The feed force-time response is similar in appearance to the torque-time curve illustrated in Figure 27.

The characteristics of the torque time curve illustrated in Figure 27 can be interpreted using the concepts illustrated in the schematic of Figure 28. The saw-tooth shaped force-time response is the expected response based on friction, workpiece deformation under the tool flank, and chip formation observations made from the machining video.(32) First, the force or torque on the tool increases as the chip load develops, and as the chip load develops, the friction between the chip and the tool increases. However, as the compressive
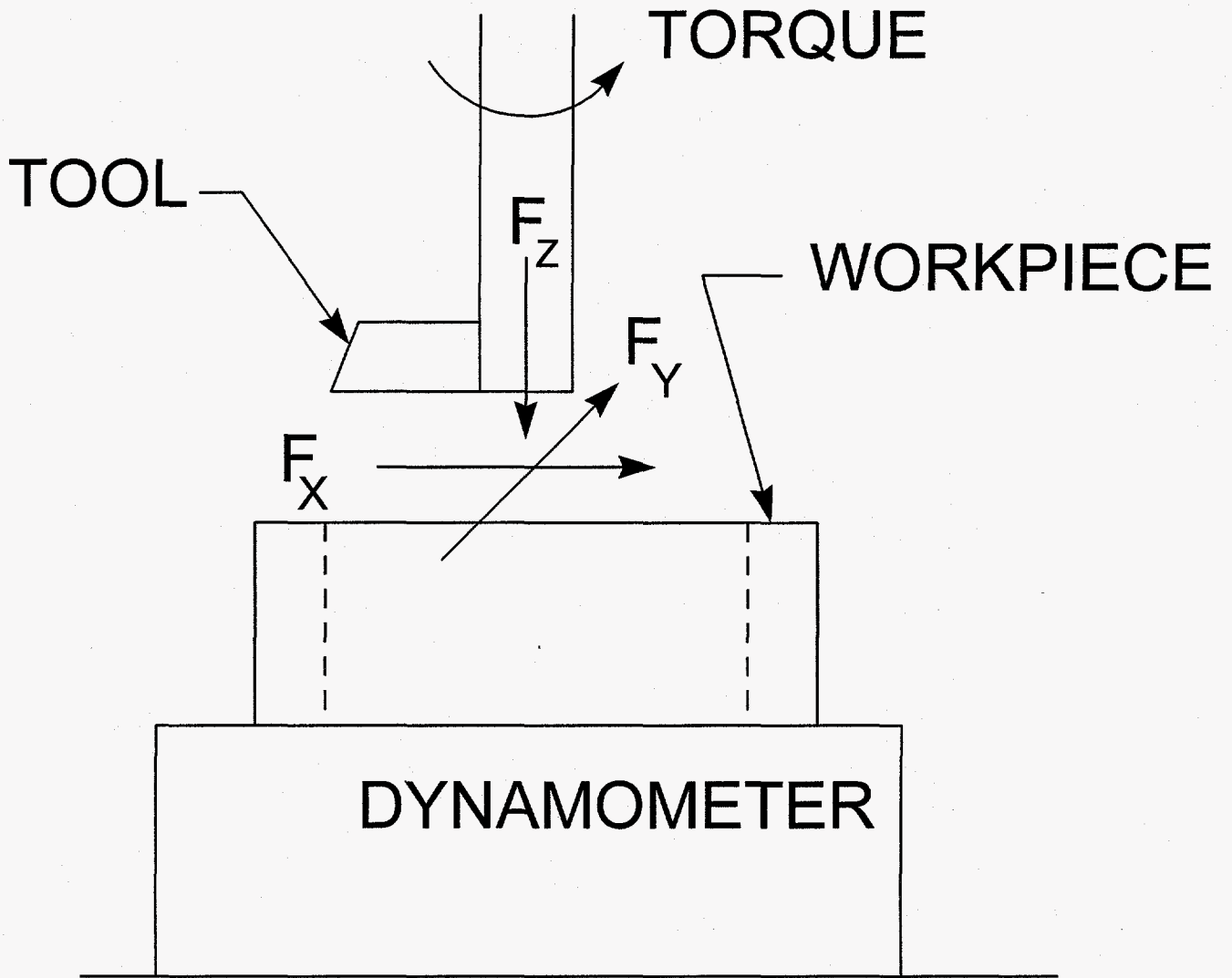
59
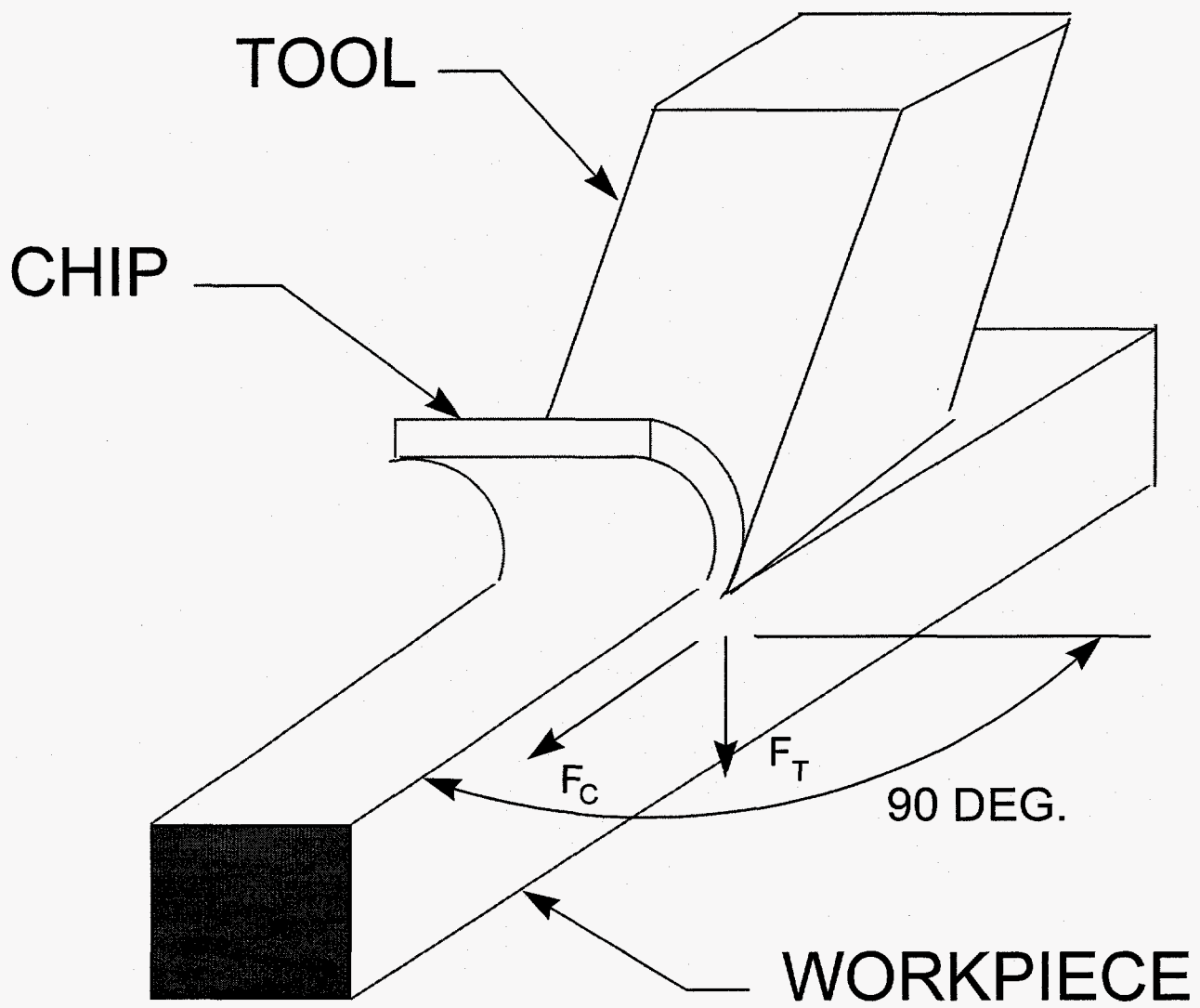
Figure 23. Schematic of Force Measurement Technique.

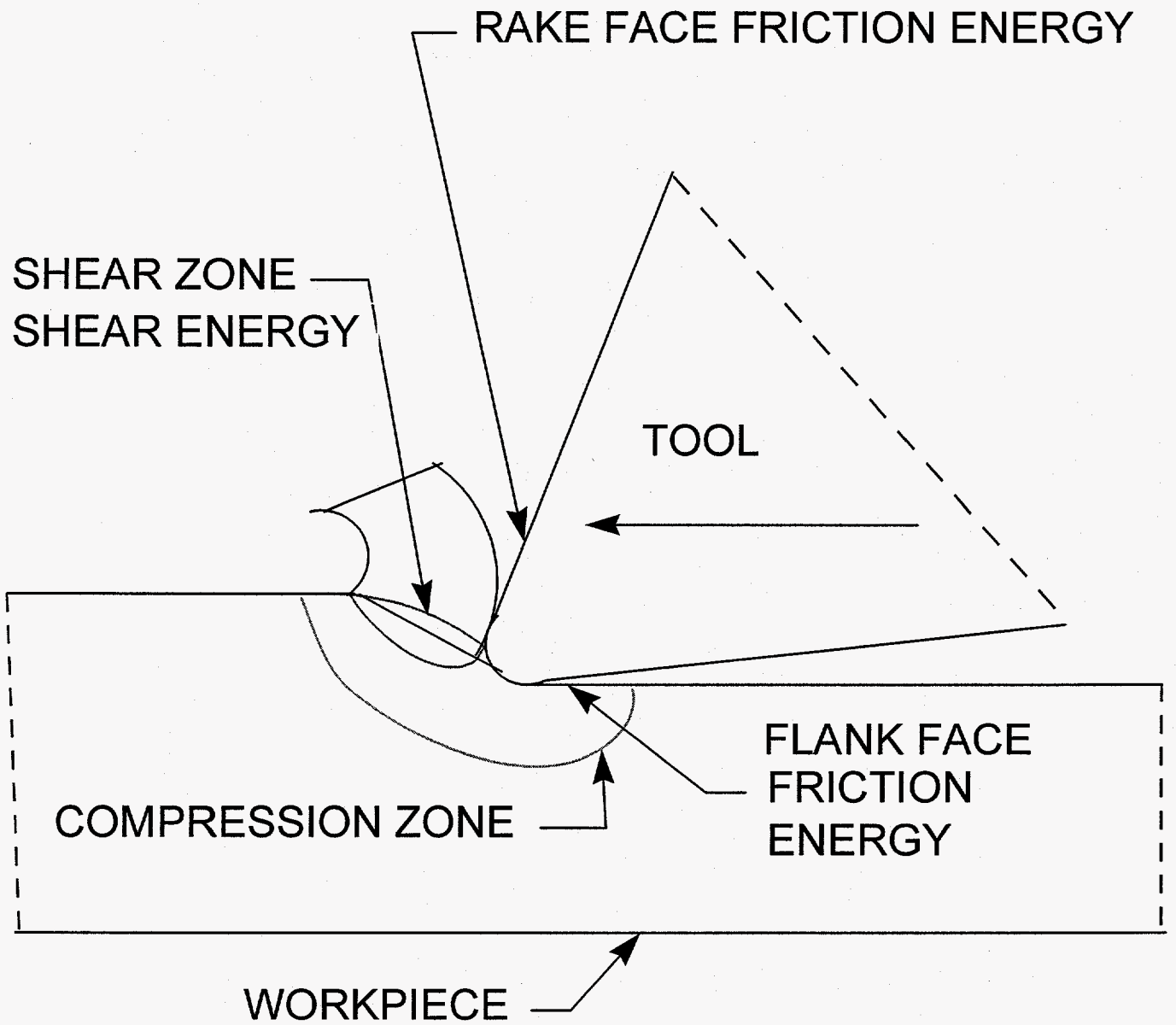Figure 24. Schematic of Orthogonal Machining.

Figure 25. Compression and Shear Zones in Cutting.

TOOL

TOOL RADIUS

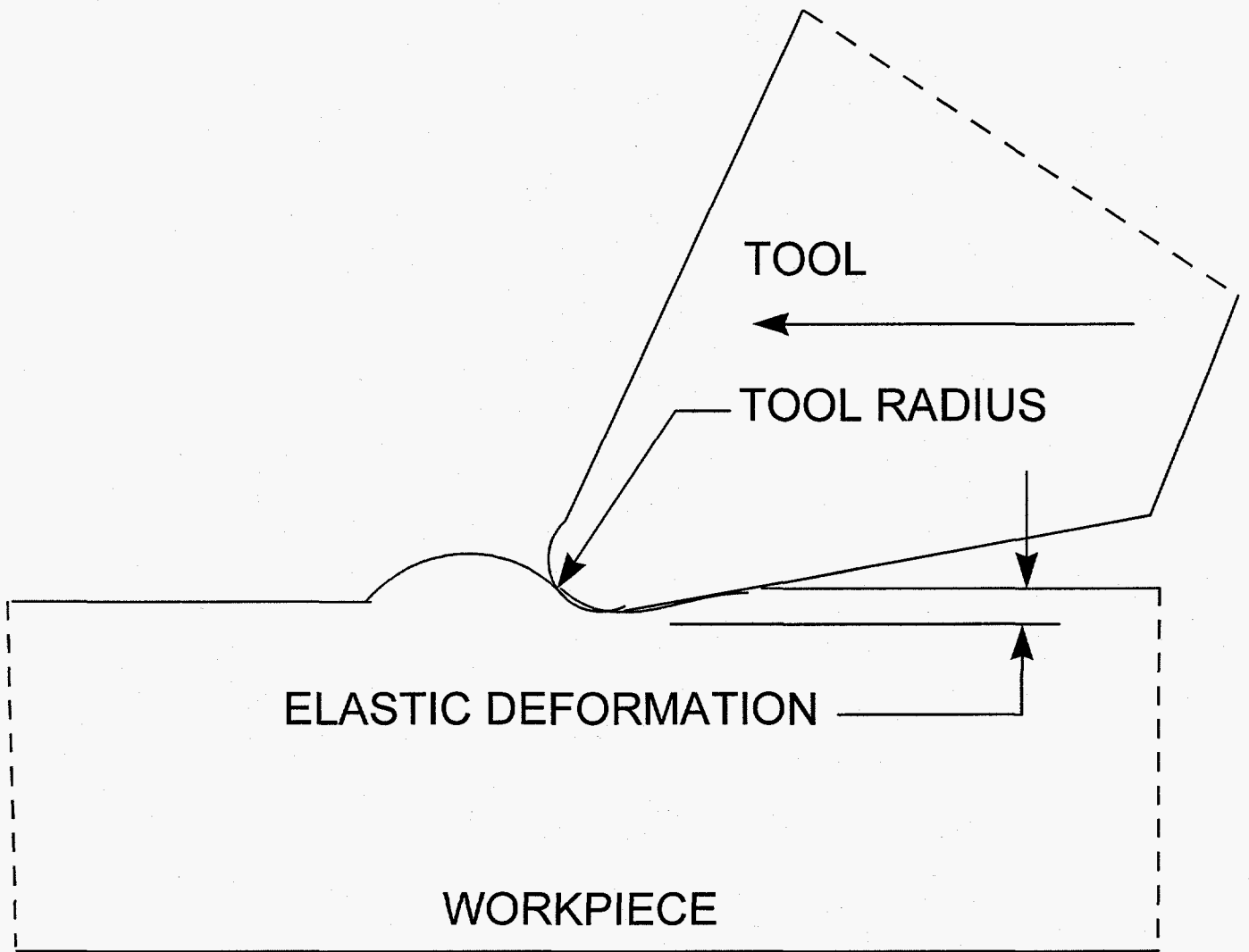ELASTIC DEFORMATION

WORKPIECE

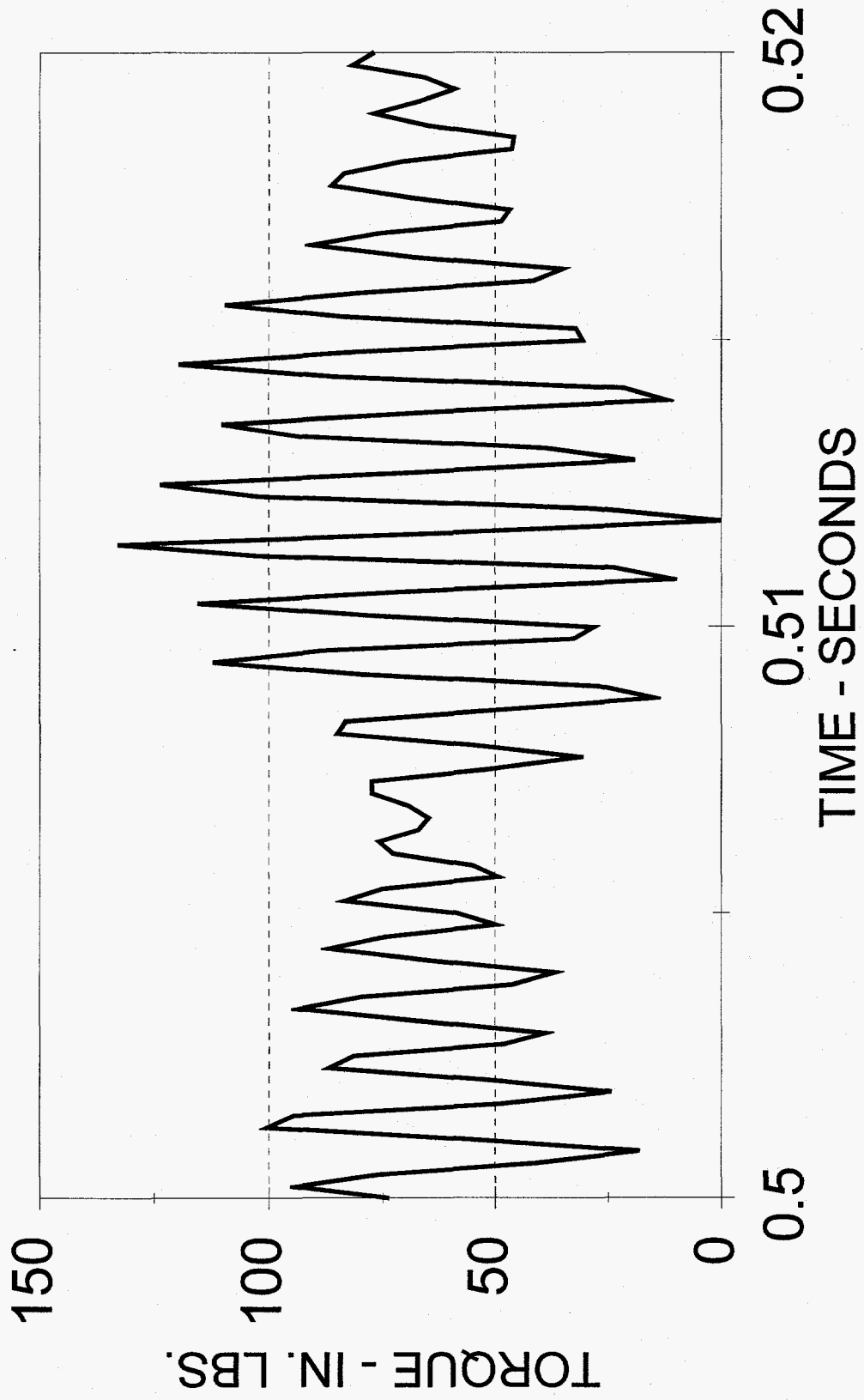Figure 26.   Flank Face Friction Schematic.
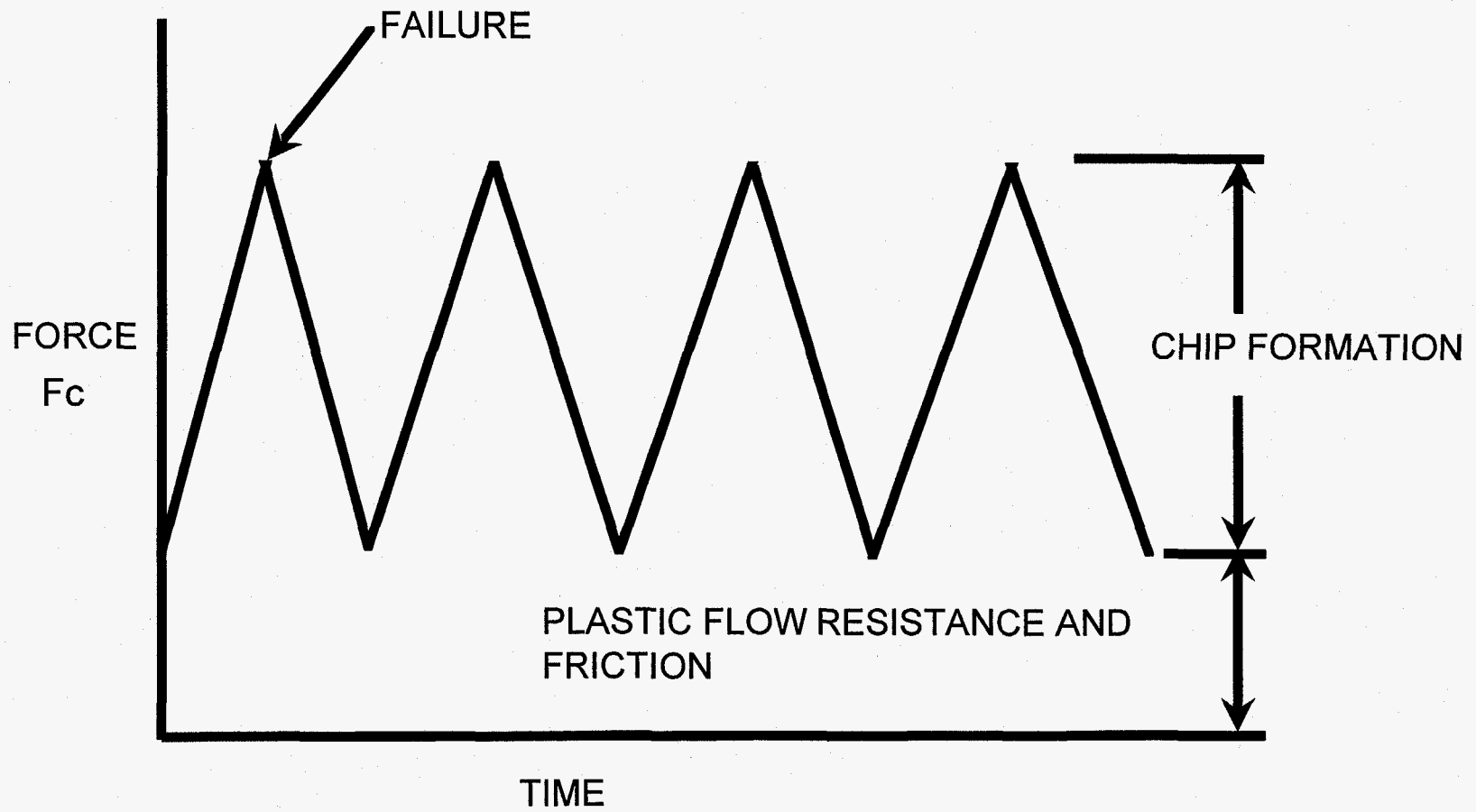
Figure 27. Torque-Time Response

Figure 28. Expected Force-Time Response for Machining.

stress in the workpiece increases, the flow stress in the vicinity of a graphite flake is exceeded, and fracture occurs along flakes and through the matrix between flakes.

When the shearing action occurs, a chip is removed and this frees the rake face from the compressive load and reduces the rake face friction. This is the zone labeled "chip formation" in Figure 28. When the chip forms, the force on the tool rapidly decreases, but it does not fall to zero because there is still a frictional force on the flank face of the tool. The flank face friction load is a function of the deformation occurring beneath the tool edge during cutting and the modulus of the material being cut.

Elastic deformation exists in the workpiece under the tool at all times during machining. The elastic deformation produces a continuous friction force acting on the tool flank face, and this is the region where most cutting tools machining cast iron first deteriorate.

Tool wear is actually a consequence of a sequence of events. First, flank wear occurs which exposes additional flank area to the workpiece which, in turn, produces a higher frictional force. The higher frictional force, coupled with the compressive load on the nose radius (rake face), increases the tool temperature to its softening point and this accelerates the nose radius wear. As the nose radius wears, the forces on the flank and nose radius increase. The tool temperature and stress continue to rise until the nose radius is blunted and the proper tool geometry lost.

The analysis being developed of the component forces in cutting uses the vertical offset (friction) force in Figure 28 to estimate the flank face force exerted on the tool. The difference in the top peak to bottom peak forces is used to estimate the shear and rake face forces. Treating the machining data in this manner yields results that correlate with results reported by a commercial machine shop regarding tool life when machining motor blocks.

The study involved four batches of engine blocks. These are referred to as "Current" representing blocks produced in Foundry #1 and machined in the period of April through June, 1996; "Summer" representing material produced in Foundry #1 in the period of June through August, 1995; "Winter" representing material produced during the period of January-February, 1996; and "Standard" representing blocks from Foundry #2 which is believed to deliver iron with consistently acceptable machinability. Cylinders were cut from blocks from each batch. Force-time data was recorded as the cylinders were rebored on a CNC mill operated at 200 rpm using a feed of 0.007 inches per revolution and a depth of cut of 0.015 in. Torque-time curves obtained on each material (such as illustrated in Figure 27) were analyzed to extract the work associated with metal shear, rake face friction, and flank face friction.

The percent of total energy consumed in 1) shearing (chip formation), 2) rake face friction, and 3) flank face friction,

respectively are illustrated Figures 29 to 31. The analysis indicates that on average 30% of the total work is associated with shear work, 30% is associated with rake face friction, and 35-40% is associated with flank face friction.

Significant differences are evident in the "Summer" and "Winter" irons from Foundry #1 compared to the "Standard" iron from Foundry #2 and the "Current" iron from Foundry #1. The flank face friction of the "Summer" and "Winter" irons was higher than the flank face friction in the "Current" and "Standard" irons. This correlates to the shorter tool life observed in the "Summer" and "Winter" irons when compared to the tool life in the "Current" and "Standard" irons. The elastic moduli of the "Summer" and "Winter" irons were higher than the moduli of the "Current" and "Standard" production irons. The higher elastic moduli (which reflect higher stiffness irons), produce a higher flank face load. This higher flank face load, with other conditions remaining constant, produces more frictional heat and faster wear on the tool flank. High flank face loads coupled with higher microcarbide concentrations in the iron have synergistic effects that increase tool flank face wear and decrease tool life.

The above studies were conducted on commercial cylinder liners. The machining characteristics were based on reported tool behavior and life and not on laboratory measurements of tool life. Additional studies along these lines must be conducted using irons of defined machining characteristics to further verify the model.

Ductile Iron Plate Castings

Drill Life

Drill life experiments were performed on six sets of ductile iron plates submitted by participating foundries. The drill life results obtained on ductile irons are summarized in Figure 32. The results are presented in the same format and on the same scale as the gray iron drill life results. The failure criteria in the ductile iron drill life experiments was 0.005 inches of flank wear. Tool wear was generally higher when machining ductile iron compared to gray iron, perhaps because the higher modulus produced more frictional heat at the tool flank and the higher yield stress produces more heat at the rake face compared to gray iron.

However, the tool wear curves of ductile irons with yield strengths in the range of 45-55 ksi generally overlay the tool wear curves obtained with gray iron having a fracture stress in the range of 40-50 ksi.

The irons submitted for analysis included 65-45-12 and 80-55-06 grades of iron. Ductile iron grade 65-45-12 generally had the best tool life. Two heats of 80-55-06 and one heat of 65-45-12 exhibited mid-range tool life, but one heat of 65-45-12 and one heat of 80-52-03 fell at the bottom end of the tool life range.
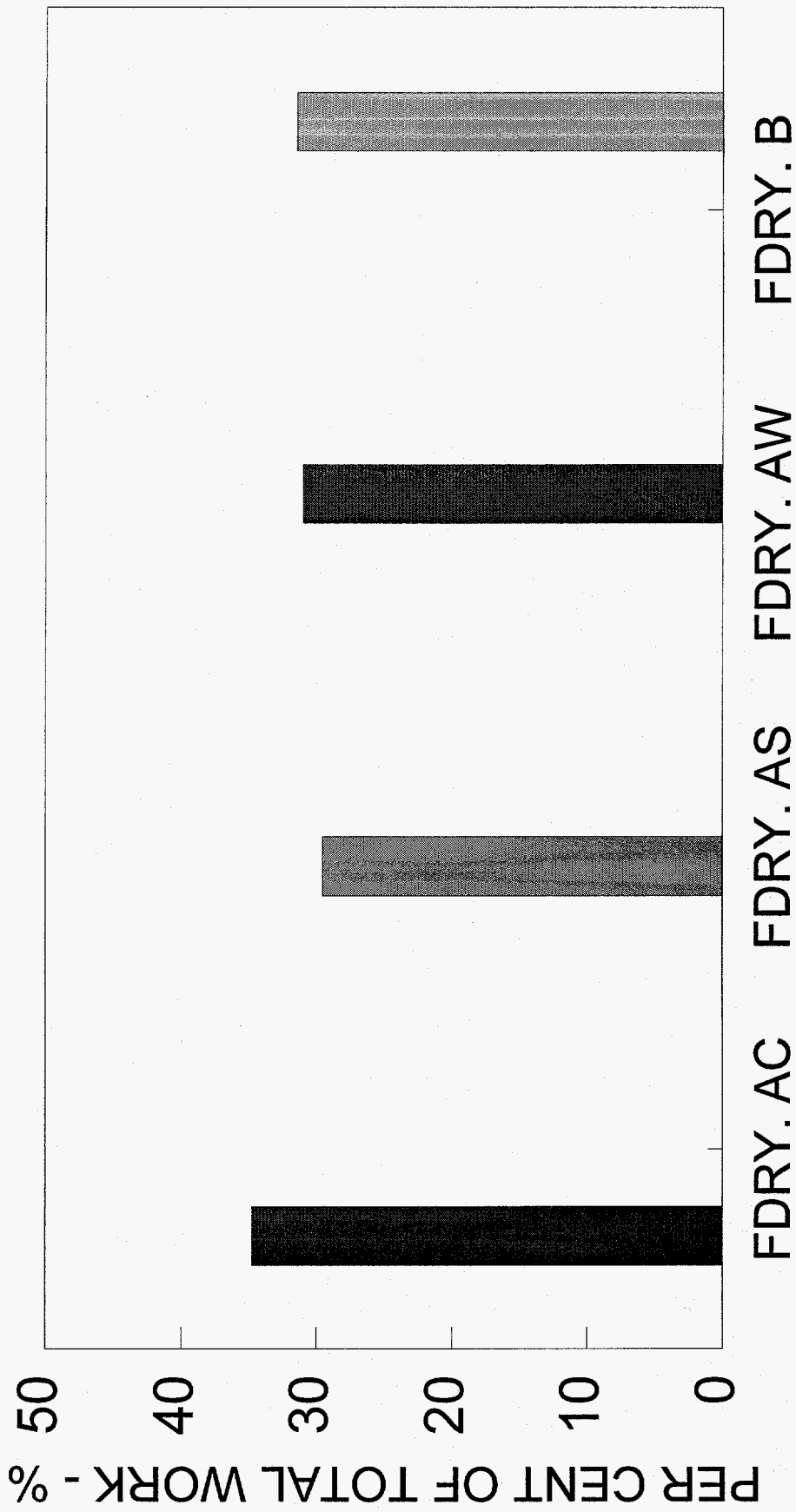
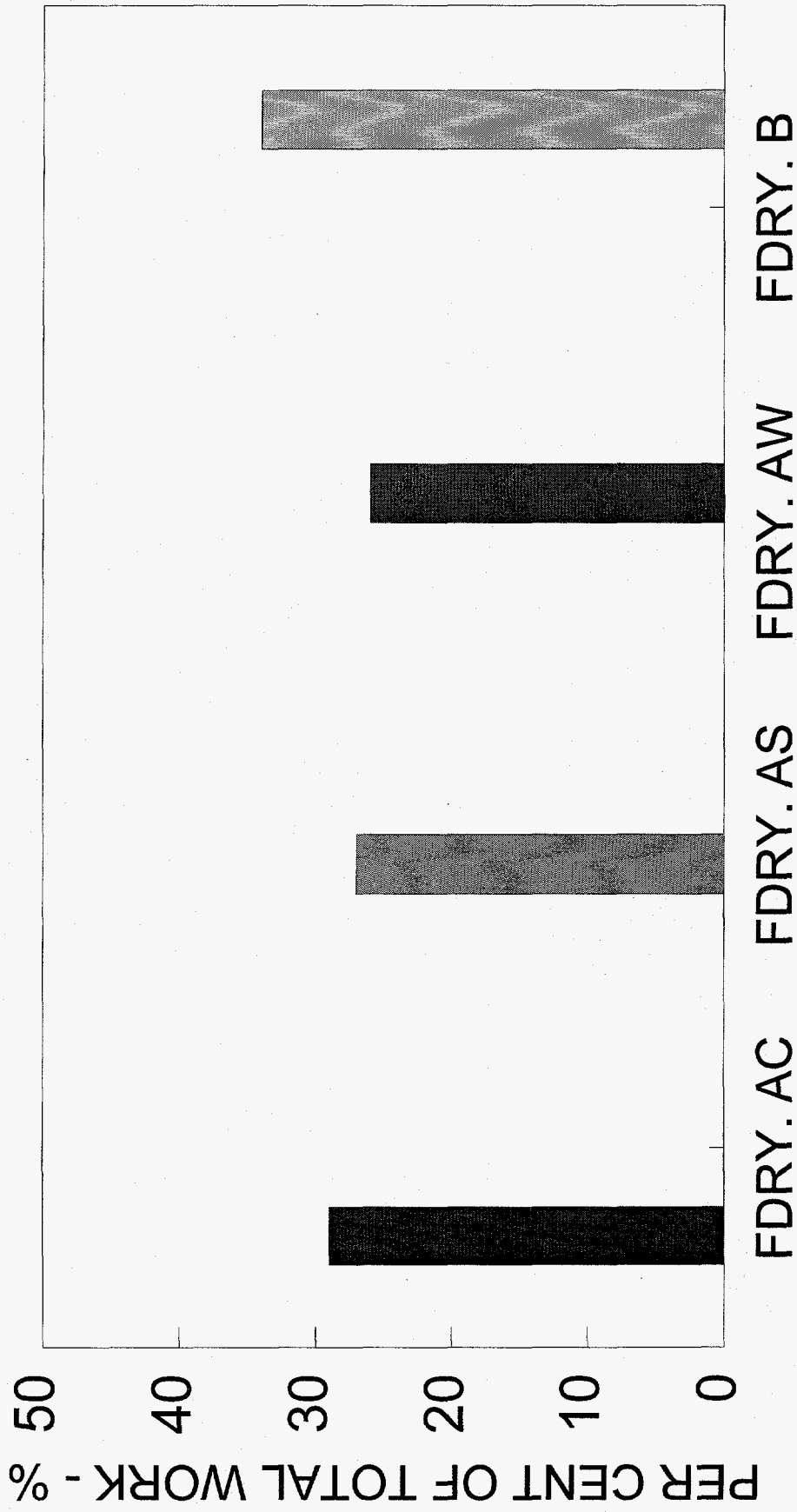Figure 29. Shearing Work. 200 RPM-0.007 In./Rev.— 0.015 In. Cut.

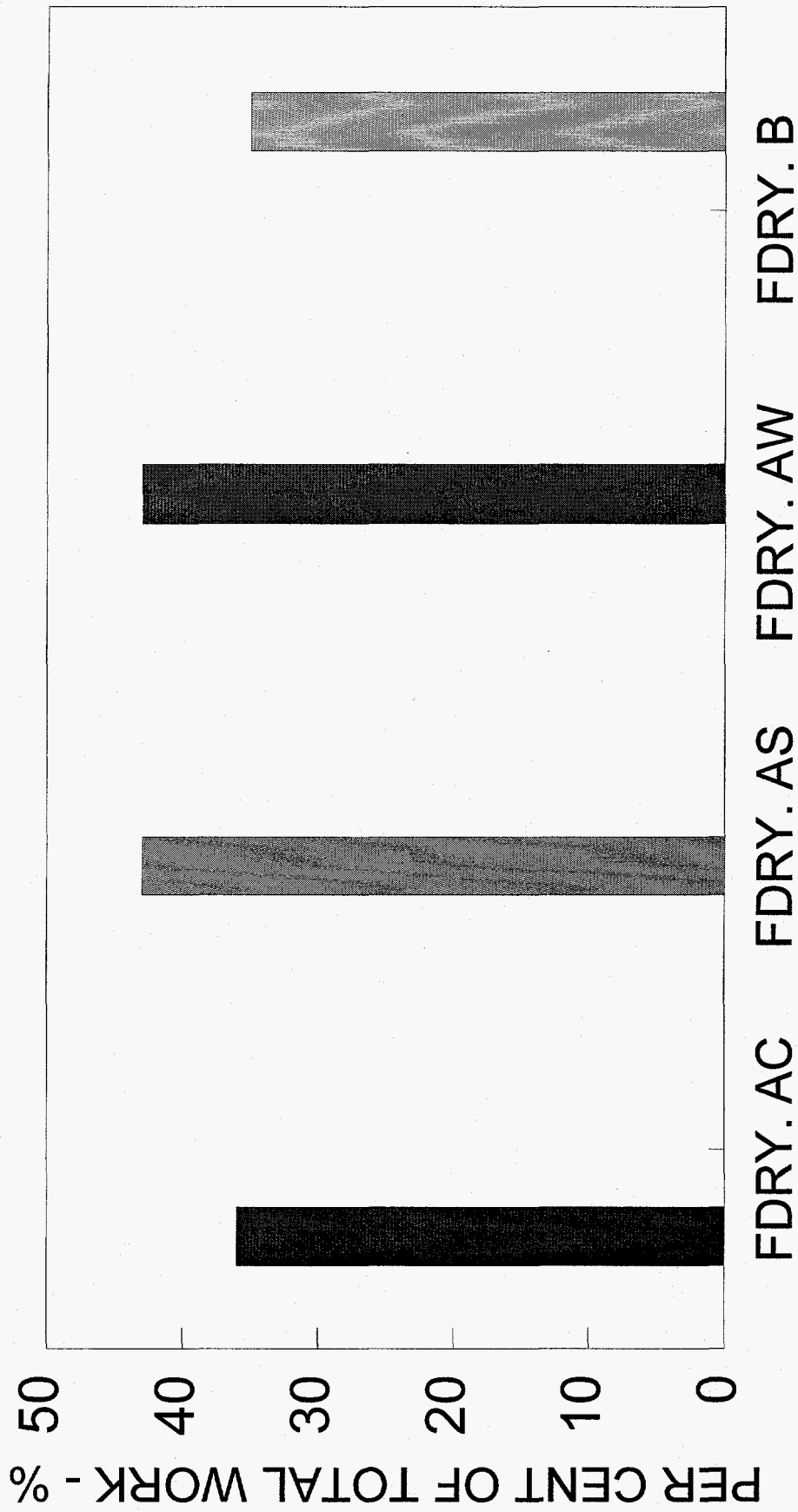Figure 30. Rake Face Friction Work. 200 RPM-0.007 In./Rev.-- 0.015 In. Cut.

Figure 31. Flank Face Friction Work. 200 RPM-0.007 In./Rev.-- 0.015 In. Cut
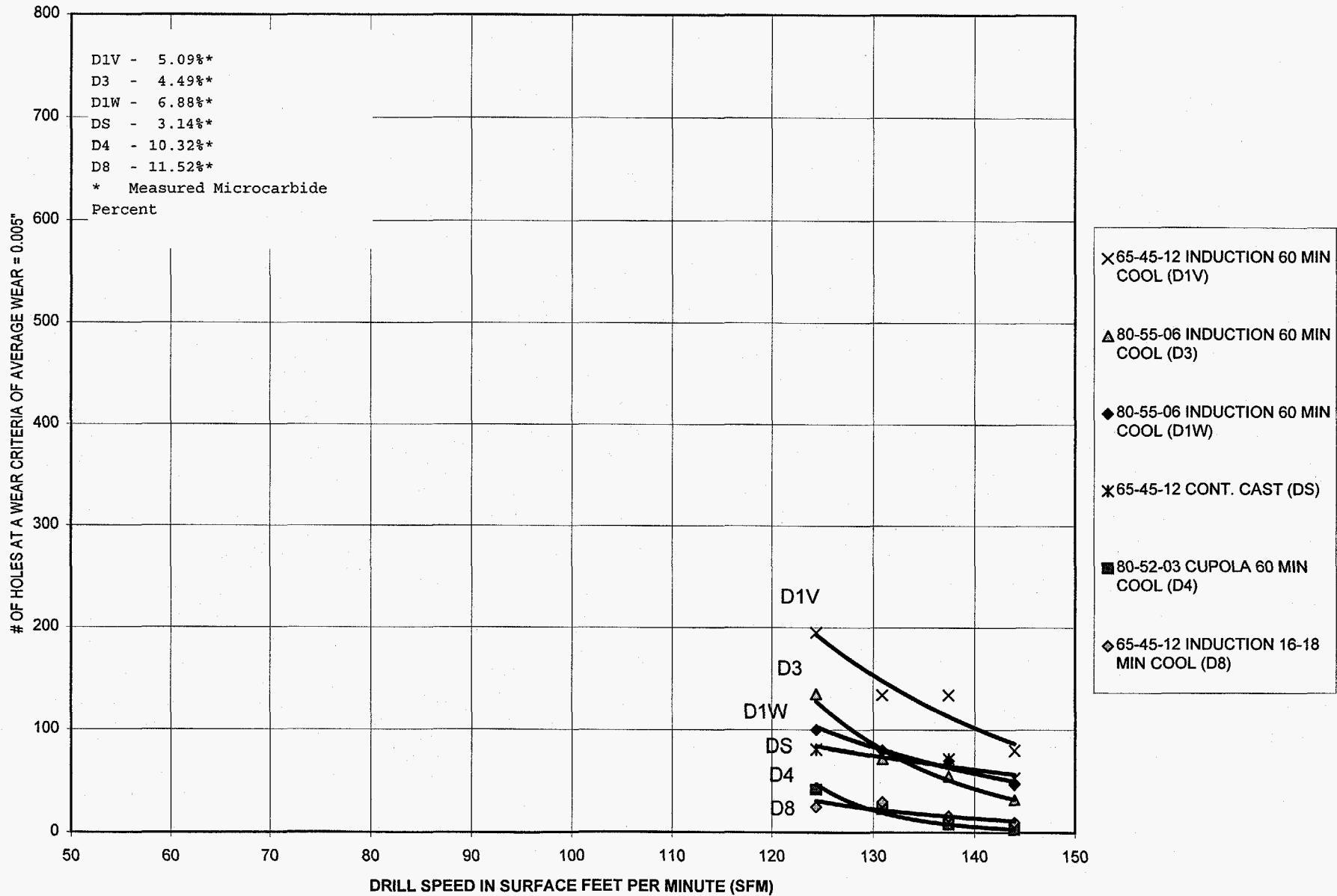
Figure 32.   Tool Life Curves for HSS Drilling of Ductile Iron Plates
(Number of Holes Drilled as a Function of Drill Speed).

Experimentally determined microcarbide contents are available on all irons, and the effect of microcarbide content on tool life is illustrated in Figure 33. The machinability decreased as a second order function of microcarbide content. These results are similar to those observed in the gray irons. The theoretical microcarbide weight percent versus actual microcarbide weight percent for these irons is presented in the insert of Figure 32. The microcarbide content increased as the volume percent pearlite increased as illustrated in Figure 34.

Microstructures

Representative etched and unetched microstructures from the 65-45-12 and 80-55-06 drill plates are illustrated in Figures 35 to 36. The 64-45-12 microstructures consisted of graphite nodules with a ferritic and pearlitic matrix. The 80-55-06 microstructures consisted of graphite nodules with a higher volume fraction pearlite. No massive carbides were found in any of the ductile iron plates.

Quantitative measurements of ferrite, pearlite, and TiX volume fractions are presented in Table X. As the ferrite volume fraction increased, the machinability generally increased as illustrated in Figure 37, but there was a large amount of scatter in the data. The iron labeled D8 was significantly off the trend line.

As the amount of pearlite increased, the machinability decreased as indicated in Figure 38. Again, there was some scatter, and D8 fell significantly off the trend line. Future microstructural measurements must be made to determine why these irons were off the trend lines.

Graphite Analysis. Analyses were made of several microstructural features including graphite volume percent, graphite surface area per volume material, graphite mean spacing, nodule number density, average nodule diameter, maximum nodule diameter, and average nodule circumference. As the volume percent graphite increased in the 80-55-06 ductile irons, the machinability increased as illustrated in Figure 39. No correlation between tool life and the surface area per unit volume or mean nodule spacing with tool life was found. A lower number density of graphite nodules was observed to correlate to higher tool life as illustrated in Figure 40, but this effect cannot currently be rationalized.

Mechanical Properties

Tensile Strength. The tensile strength of each set of iron plates submitted for analysis was determined. The tensile stress-strain curves are illustrated in Figure 41 and the correlation between tensile strength and tool life is illustrated in Figure 42. The raw data is presented in Table XI. In general, the tool life decreased with tensile strength. No correlation was found between tool life and yield strength.
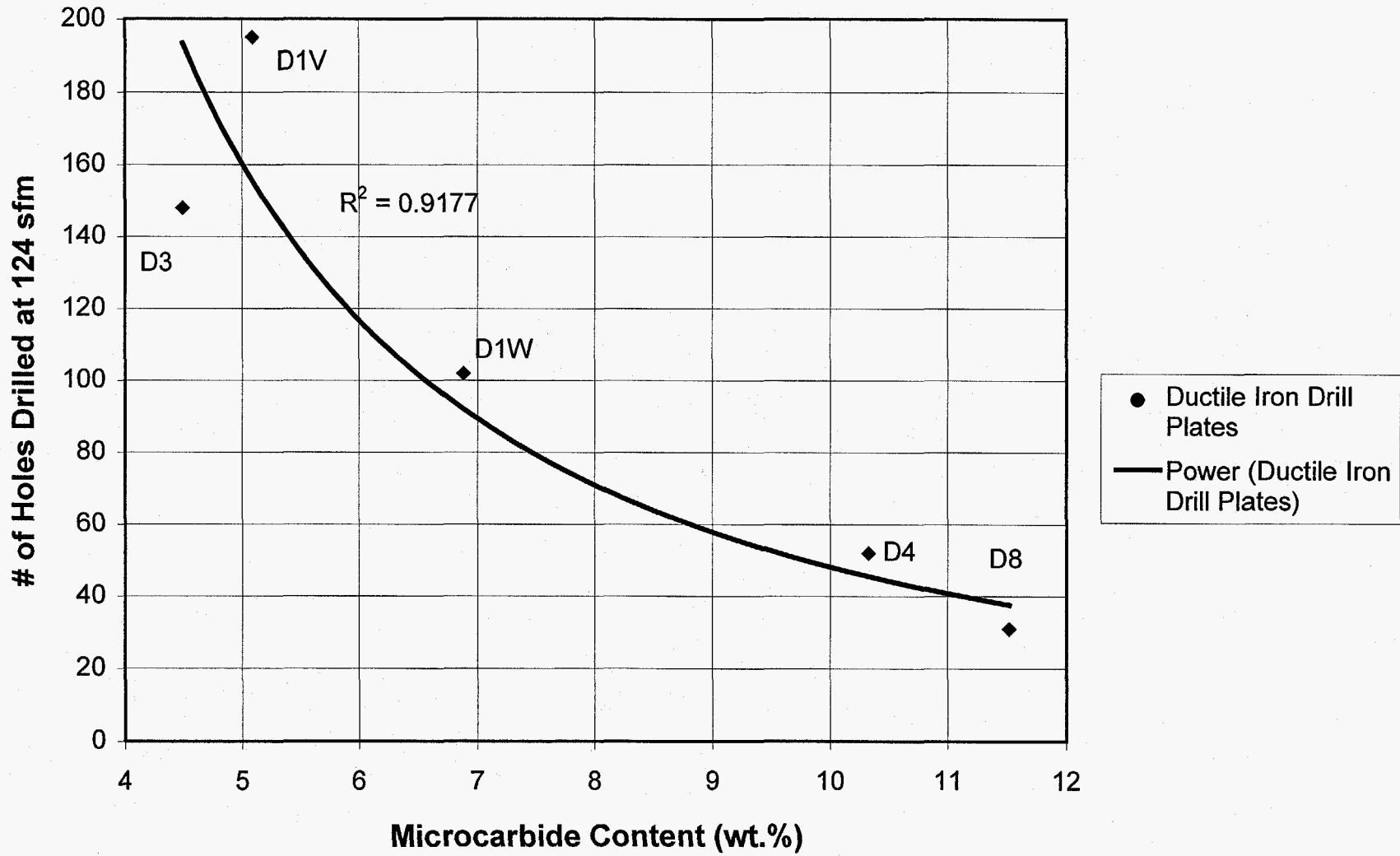
Figure 33.   Effect of Microcarbide Weight Percentage in Ductile Iron on Drill Life.
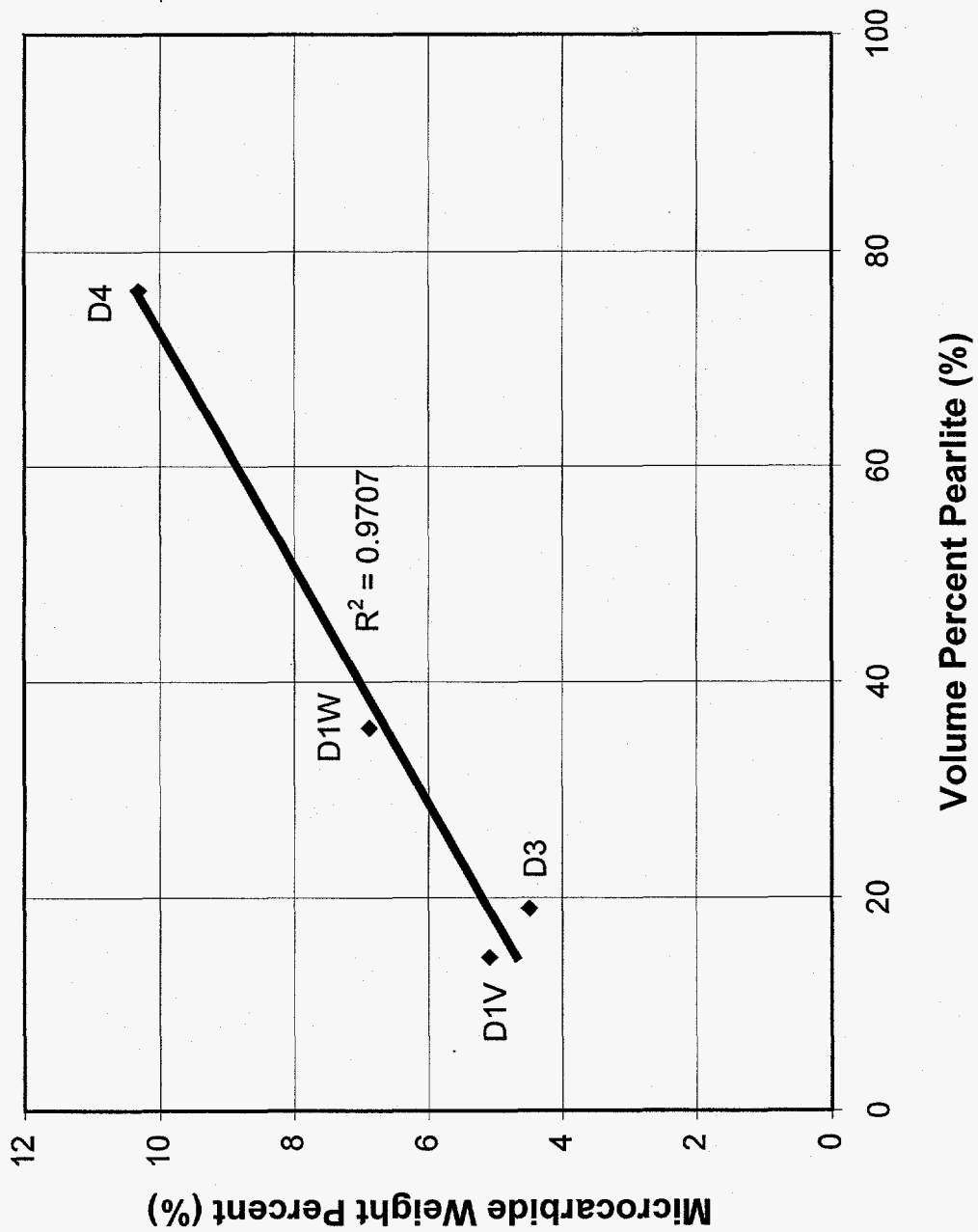
Figure 34. Microcarbide Weight Percent versus Volume Percent Pearlite in Ductile Iron Drill Plates.
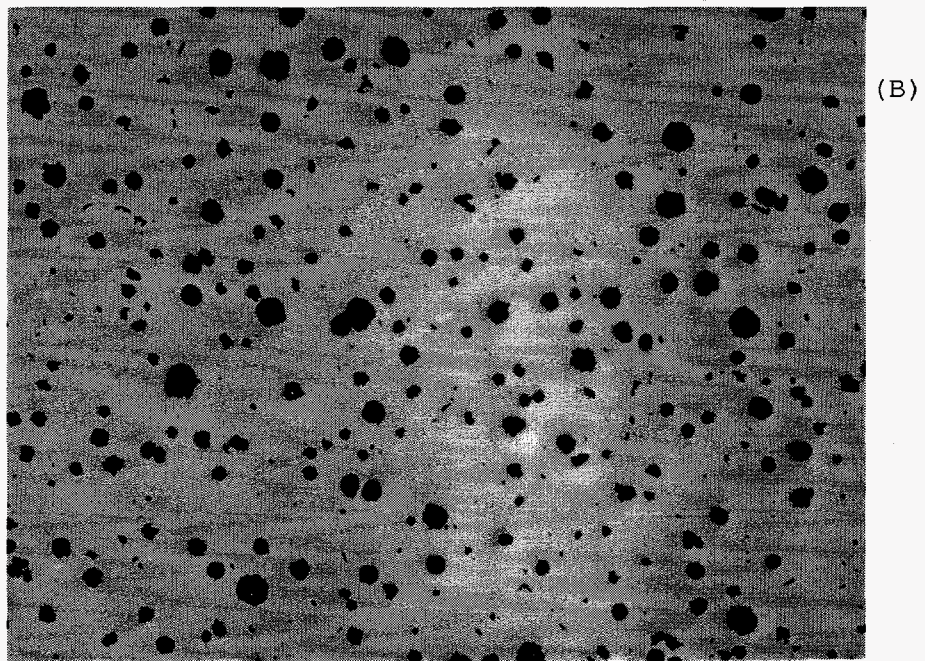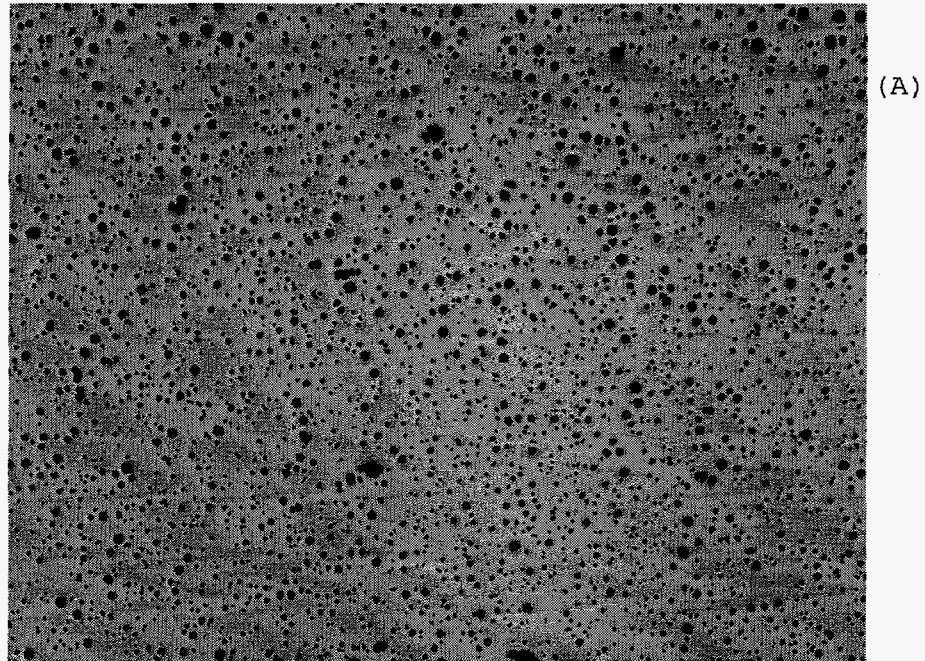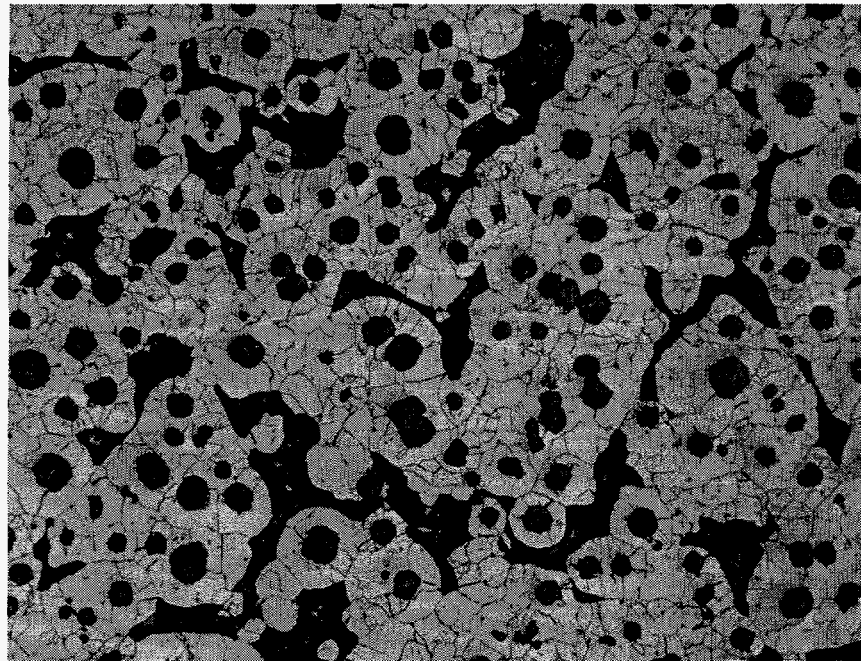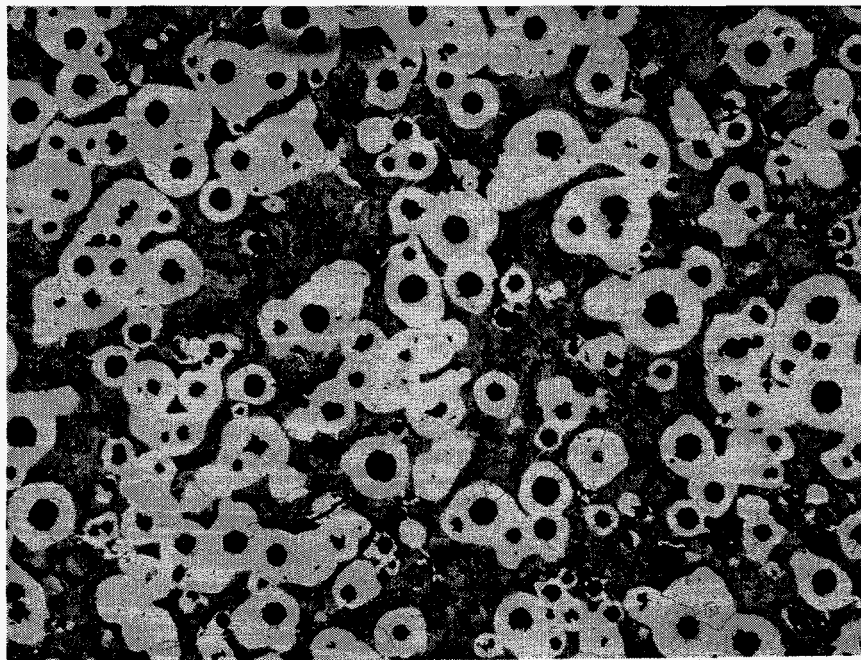
(A)

(B)

Figure 35.   Representative Unetched Microstructures
             of a 80-55-06 Ductile Iron (D1W).   (A)
             25X (B) 100X.

(A)

(B)

Figure 36.   Representative Etched Microstructures of
a (A) 65-45-12 Ductile Iron (D1V) and (B)
a 80-55-06 Ductile Iron (D1W). 100X,
Nital.

Table X.

Microstructural Features of the Ductile Iron Test Plates

Sample	Grade Iron	Melt Process	Tool Life @ 124 sfm	% Ferrite	% Pearlite	% TiX
D1V-3	65-45-12	Induction	195	74.2	14.4	0.00
D1W-2	80-55-06	Induction	102	56.2	35.7	0.12
D3-1	80-55-06	Induction	148	67.0	19.0	0.35
D4-34	80-52-03	Cupola	52	12.8	76.4	1.46
D8-4	65-45-12	Induction	31	50.2	35.8	
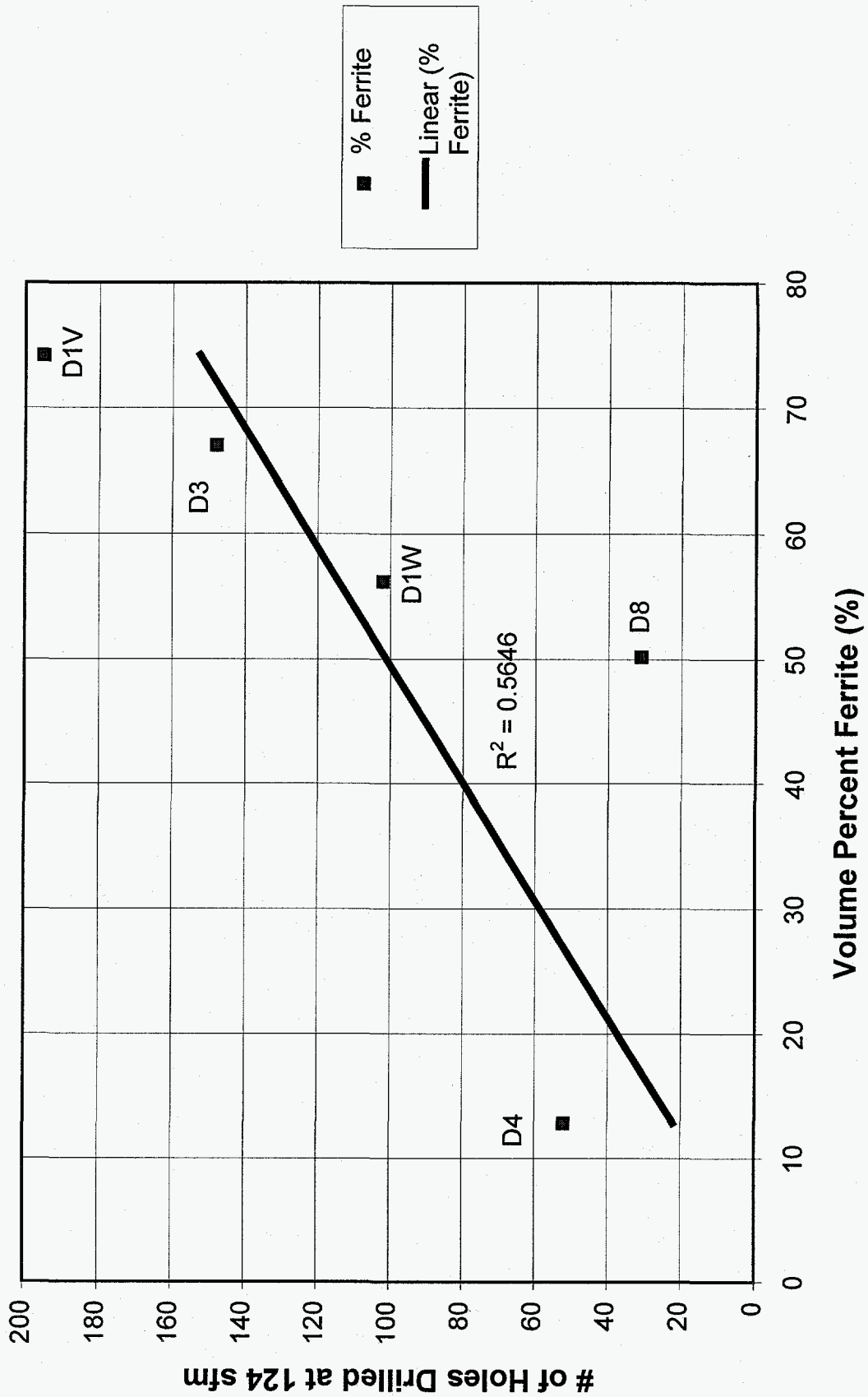
Figure 37. Effect of Volume Percent Ferrite in Ductile Iron on Drill Life.
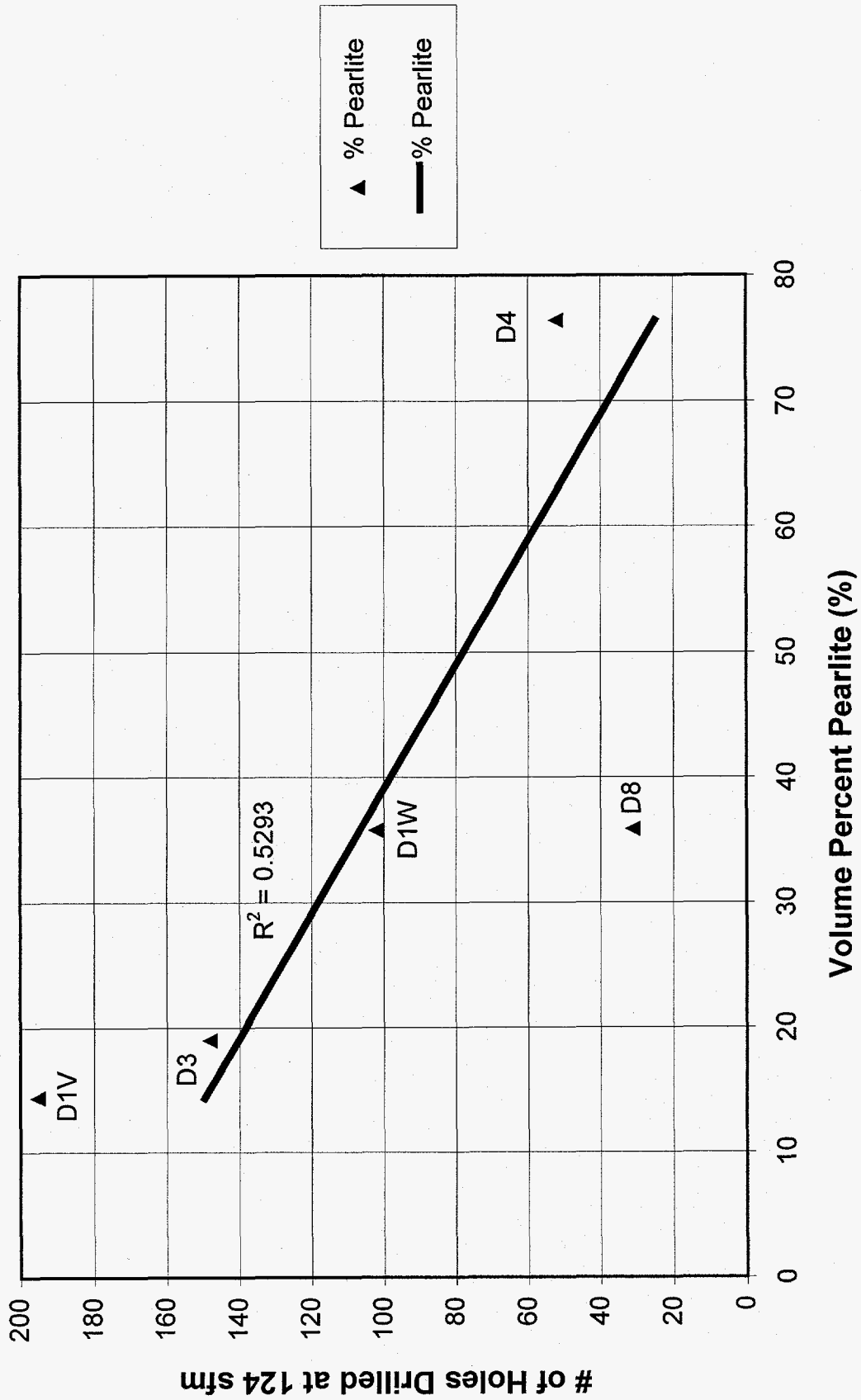
Figure 38. Effect of Volume Percent Pearlite in Ductile Iron on Drill Life.
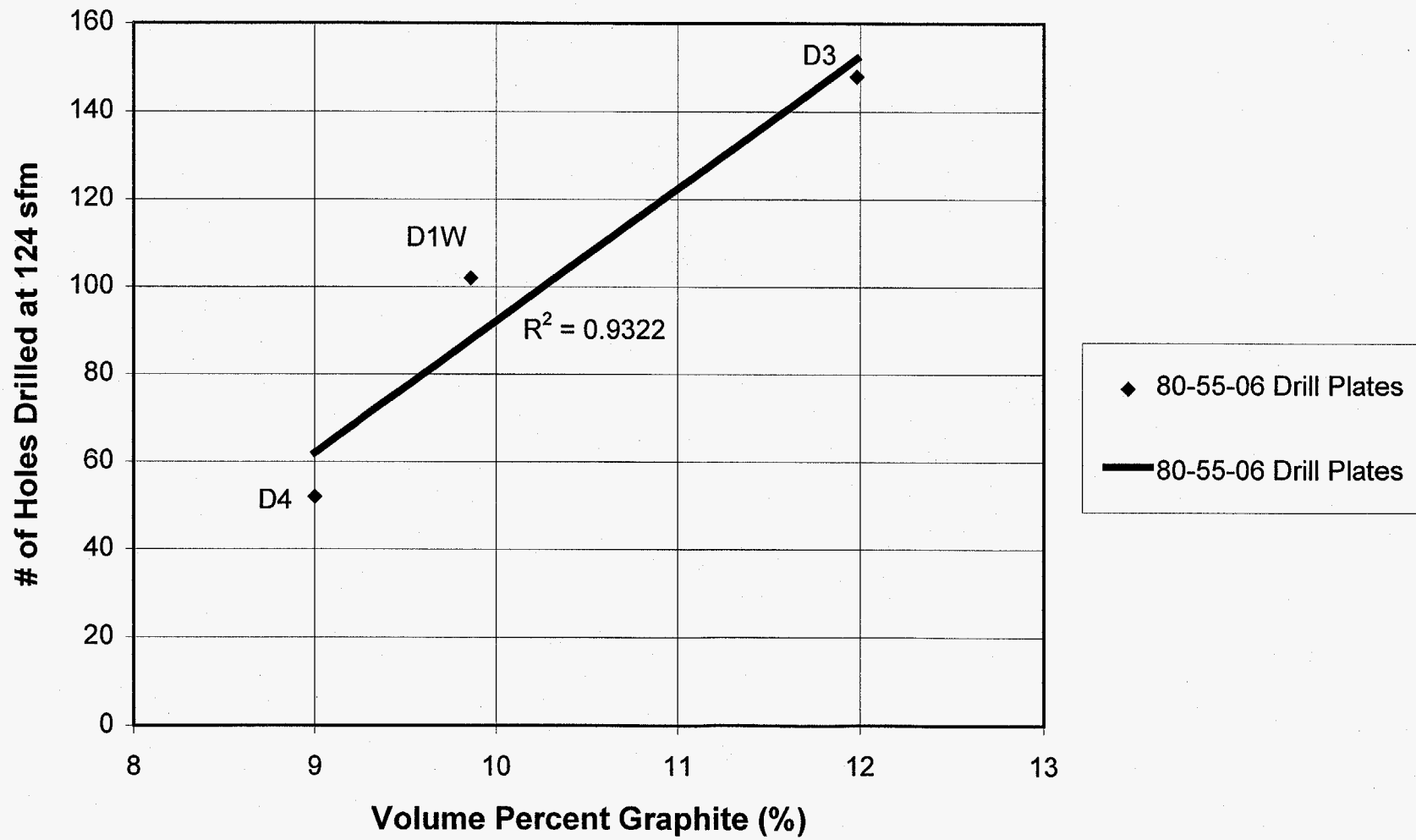
Figure 39. Effect of Volume Percent Graphite in 80-55-06 Ductile Iron on Drill Life.
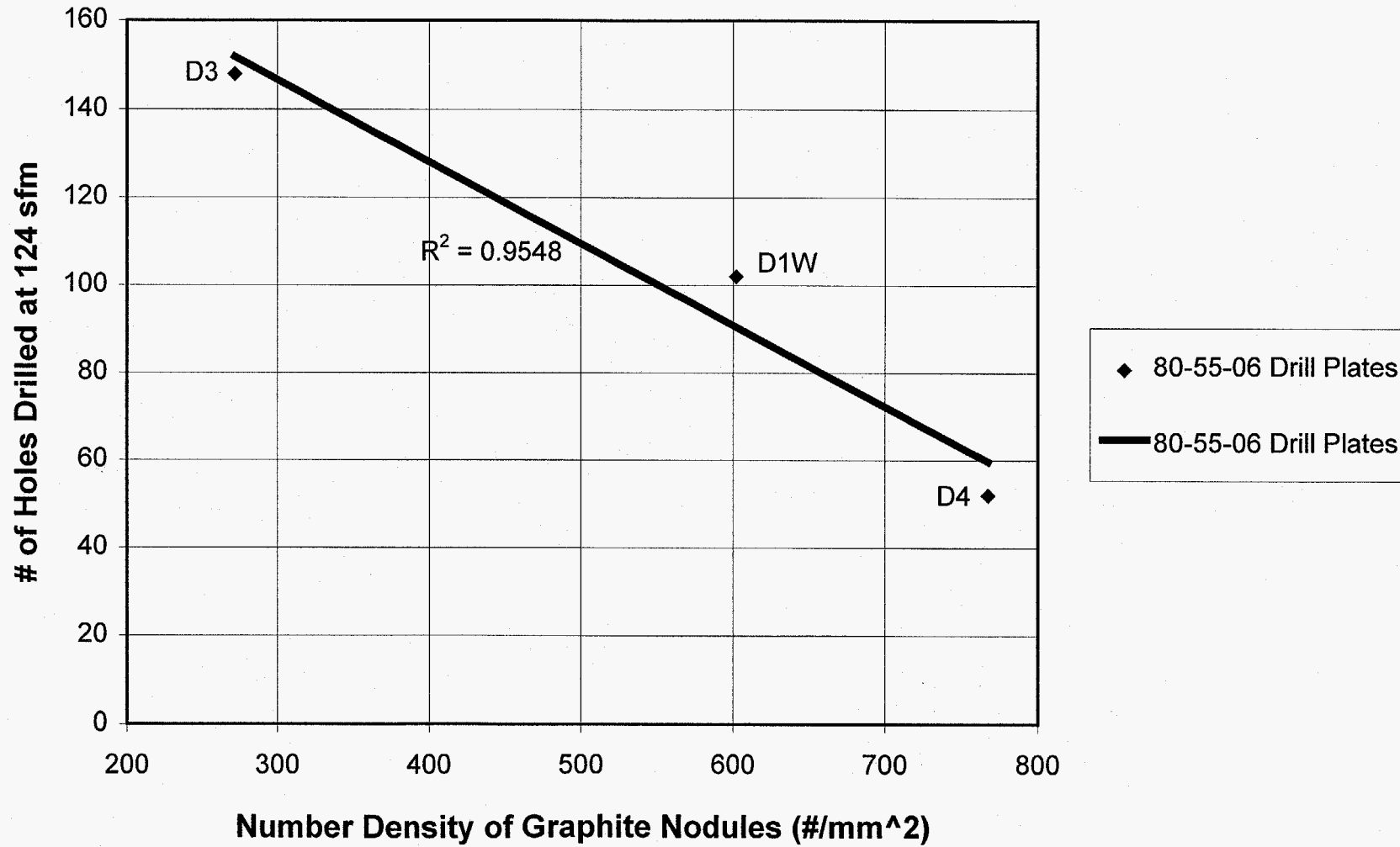
Figure 40. Effect of Number Density of Graphite Nodules in 80-55-06 Ductile Iron on Drill Life.
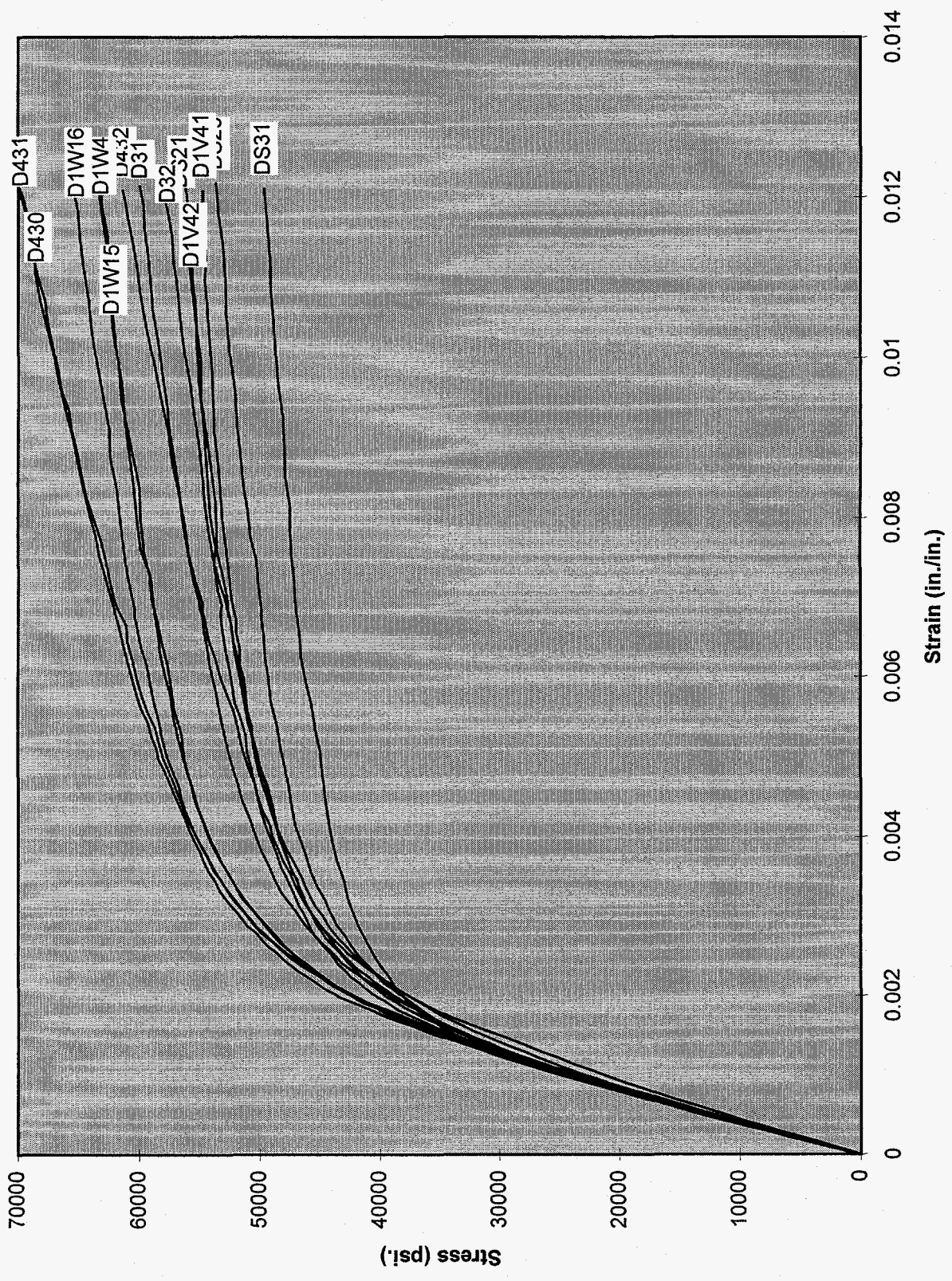
Figure 41. Tensile Stress-Strain Curves for Ductile Iron Drill Plates.
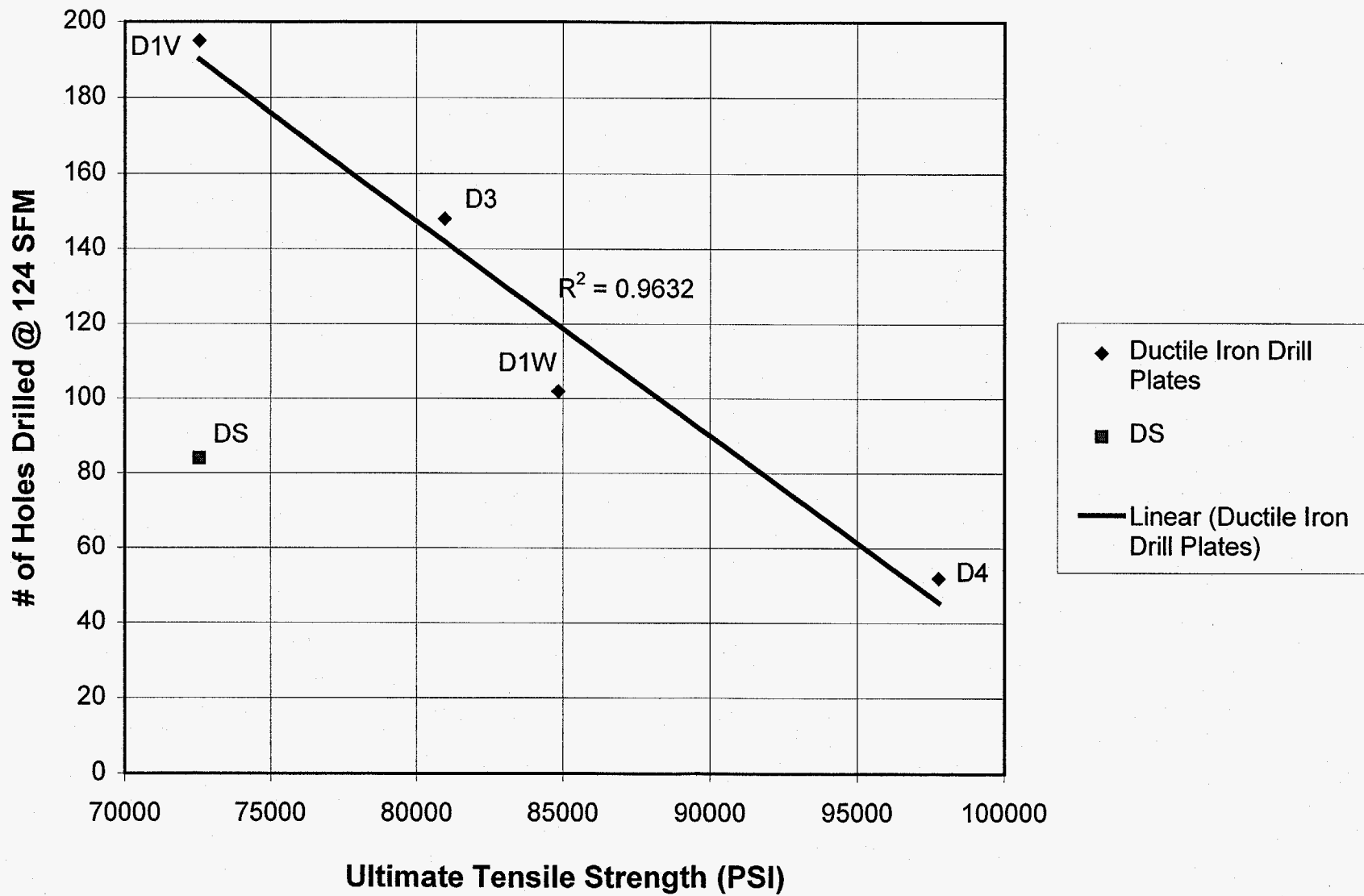
Figure 42. Tool Life versus Ultimate Tensile Strength in the Ductile Iron Drill Plates.

Table XI.

Tensile Properties from the Ductile Iron Drill Plates.

Sample I.D.	Remarks	Tool Life @ 124 sfm	Load Rate psi/m	Ultimate Strength psi	Ult. @ .2% Strength psi	0.2% Yield Strength psi	Int. Elastic Modulus 10^6 psi.	Total Strain in./in.	Measured Microcarbide Content (wt.%)
D1V41	65-45-12	195	10K	71000	48300	39400	24.23	0.080	5.09
D1V42	Induction Melt		10K	74100	49700	40500	24.23	0.105	
	Normal Cool		Average	72550	49000	39950	24.23	0.093	
			Std Dev	2192	990	778	0.00	0.018	
D31	80-55-06	148	10K	88300	50300	37930	25.64	0.115	4.49
D32	Induction Melt		10K	73600	48200	37700	23.94	0.050	
	Normal Cool		Average	80950	49250	37815	24.79	0.083	
			Std Dev	10394	1485	163	1.20	0.046	
D1W15	80-55-06	102	10K	85400	54900	42500	23.84	0.090	6.88
D1W16	Induction Melt		10K	86800	56000	42300	24.32	0.060	
D1W4	Normal Cool		10K	82300	55300	42300	23.38	0.065	
			Average	84833	55400	42367	23.85	0.072	
			Std Dev	2303	557	115	0.47	0.016	
DS21	65-45-12	84	10K	81000	48600	39000	23.75	0.110	3.14
DS29	Induction Melt		10K	77400	46700	38500	24.49	0.160	
DS31	Fast Cool		10K	69300	43700	38000	24.46	0.200	
			Average	75900	46333	38500	24.23	0.157	
			Std Dev	5992	2470	500	0.42	0.045	
D430	80-52-03	52	10K	92700	56000	42200	24.32	0.040	10.32
D431	Cupola Melt		10K	107500	56000	43400	25.32	0.070	
D432	Normal Cool		10K	93100	49800	38000	22.05	0.070	
			Average	97767	53933	41200	23.90	0.060	
			Std Dev	8432	3580	2835	1.68	0.017	

Brinell Hardness. The Brinell hardness results from the ductile iron drill plates are shown in Figure 43. As the Brinell hardness increased, the machinability decreased. The results from the Brinell hardness maps on both the gray and ductile iron drill plates are illustrated in Figure 44. The gray iron plates exhibited a smaller range of Brinell hardnesses but exhibited a wider range of machinability than was observed in the ductile iron plates.

Inoculation Effects

The ductile iron experimental matrix on inoculation involved a 65-45-12 ductile iron inoculated with (1) 0.5% addition of a foundry grade 75% ferrosilicon containing calcium and aluminum, (2) 0.2% addition of a foundry grade 75% ferrosilicon containing calcium and aluminum, (3) a 0.2 % addition of a 75% ferrosilicon containing barium, and (4) a 0.2% addition of a high aluminum 75% ferrosilicon inoculant.

Drill Life

The machinability results from the inoculation experiments are shown in Figure 45. Each data point in this figure is based on triplicate tool life determinations at the indicated surface speeds. The plates with the 0.2% addition of inoculating grade 75% ferrosilicon exhibited the best machinability. The other three sets of inoculation plates exhibited similar, but lower, tool life.

The higher addition of ferrosilicon may have resulted in the formation of oxides of aluminum and calcium that could degrade machinability. While the mechanism for improved machinability with the reduced inoculant can be questioned at this point, there is very little doubt that the reduced inoculating addition had a significant effect on machinability.

Microstructures

Representative etched and unetched microstructures of the inoculated drill plates are illustrated in Figures 46 to 48. The 65-45-12 microstructures consisted of graphite nodules with a ferritic and pearlitic matrix which varied little with inoculant type and addition. No massive carbides were detected in the ductile iron inoculation drill plates.

The results of grid counts used to measure the volume percent ferrite, pearlite, and TiX are shown in Table XII. As the volume percent ferrite increased, the machinability increased as illustrated in Figure 49.

Graphite Analysis. The graphite analysis on ductile iron inoculation drill plates included volume percent graphite, surface area graphite per volume material, graphite mean spacing, nodule number density, average nodule diameter, maximum nodule diameter, and
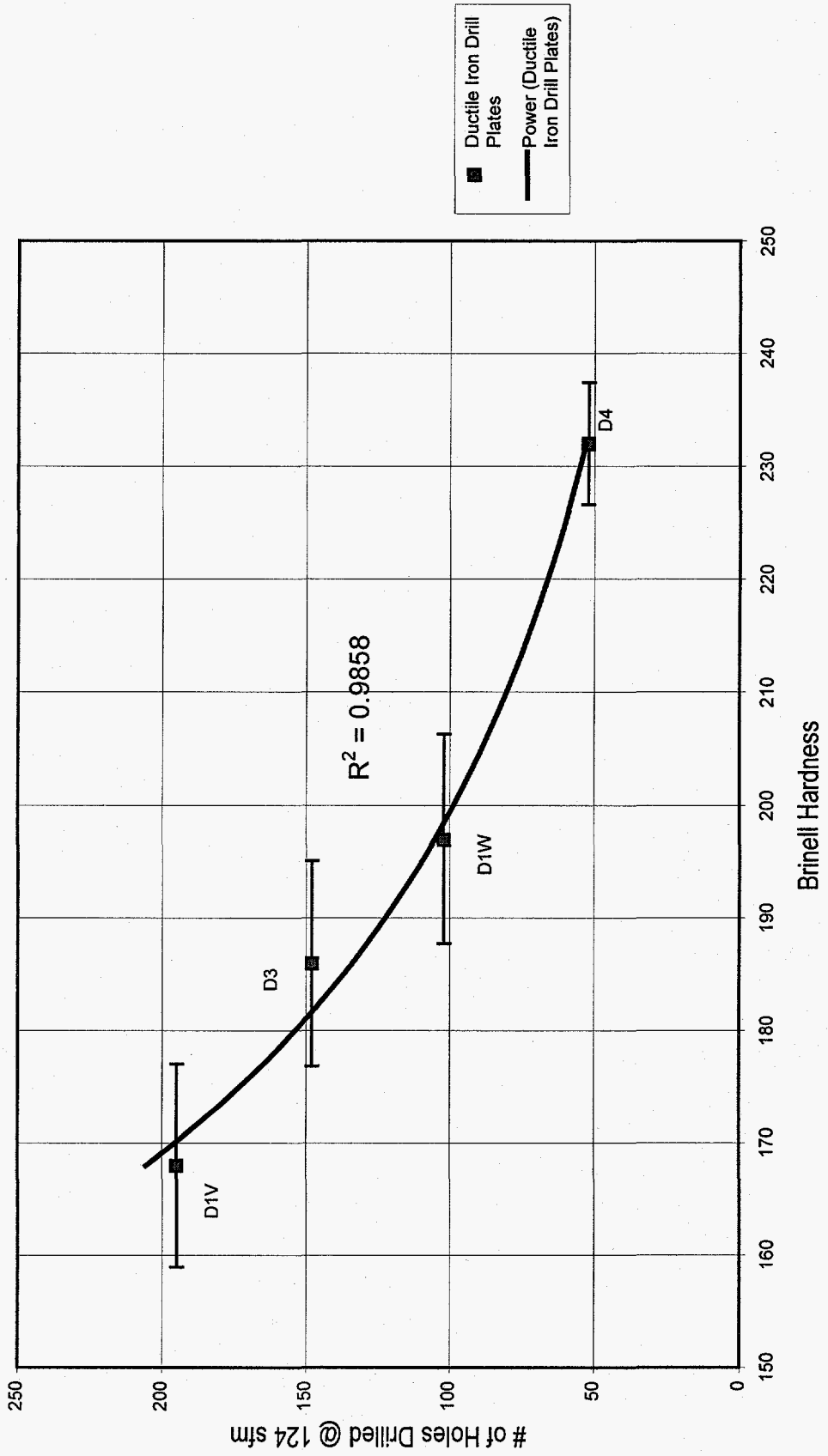
Figure 43. Effect of Brinell Hardness in Ductile Iron on Drill Life (Results from Brinell Hardness Maps).
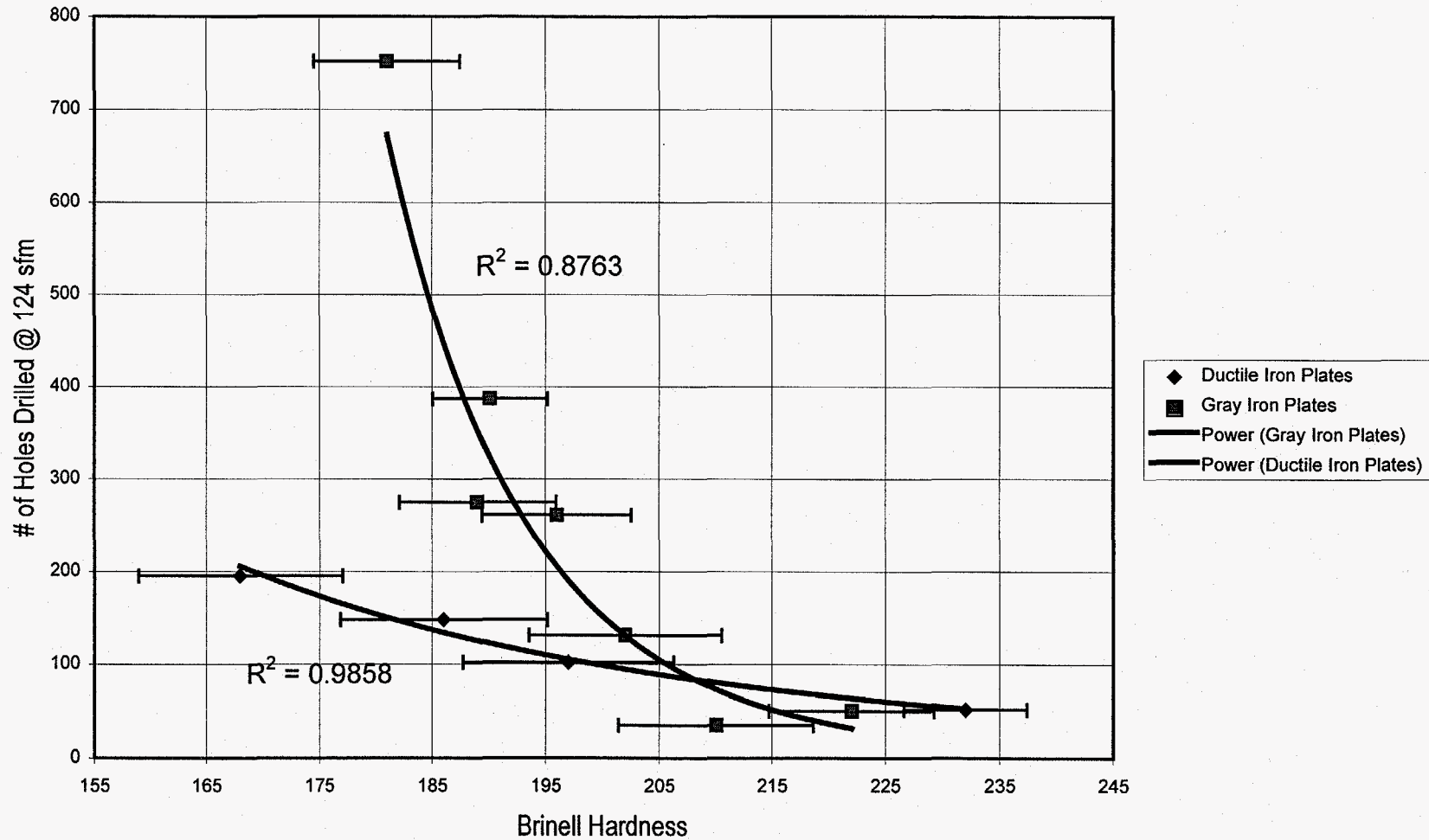
Figure 44. Effect of Brinell Hardnes in Gray and Ductile Iron on Drill Life
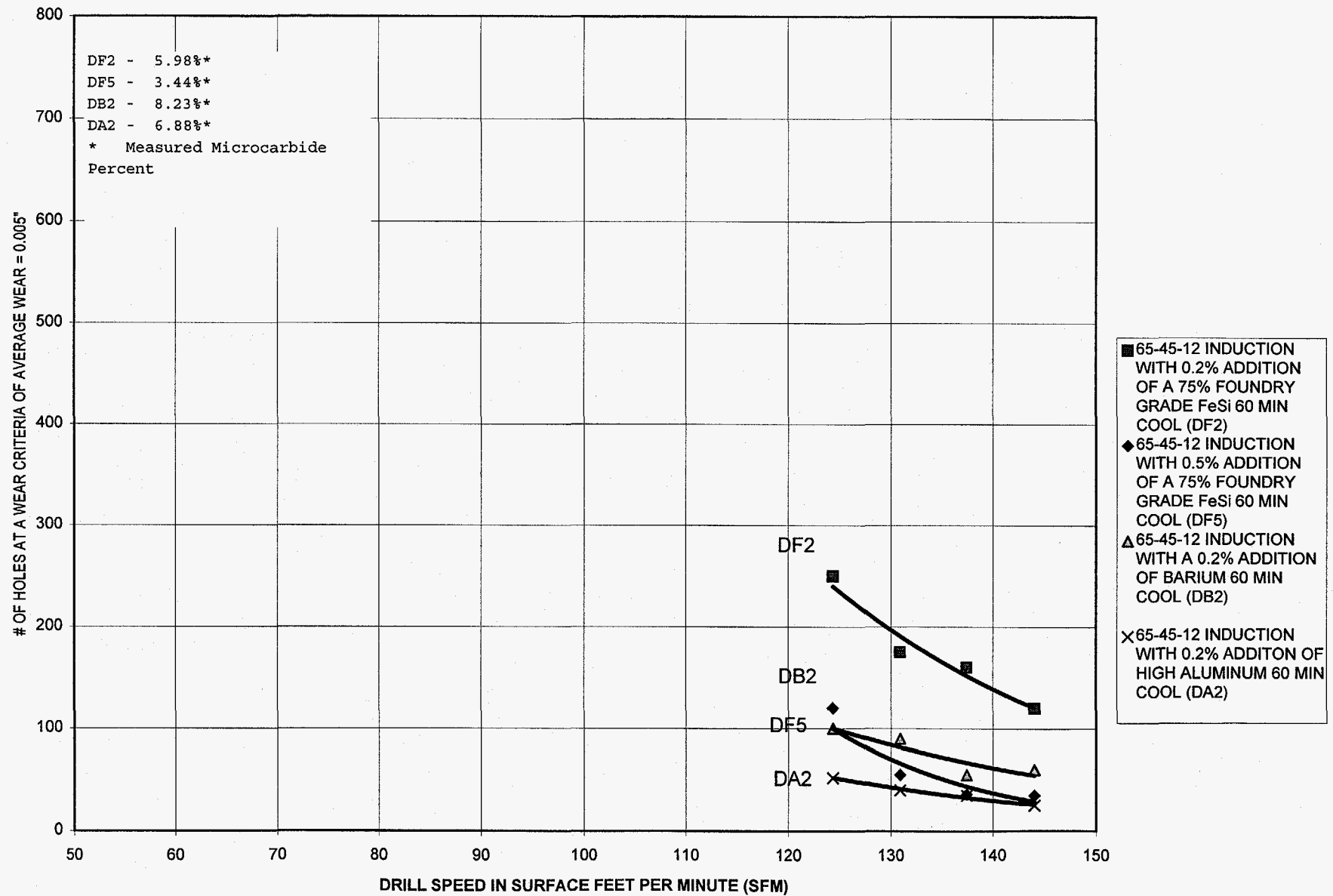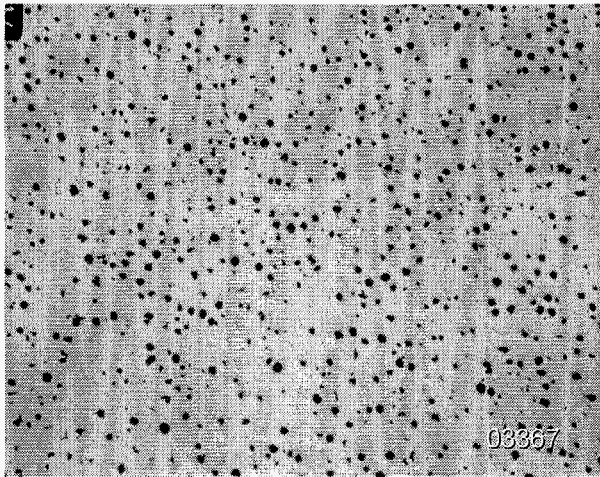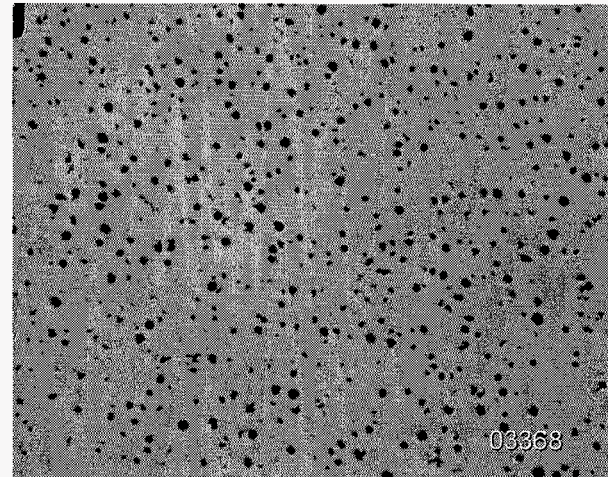(Results from Brinell Hardness Maps).

Figure 45. Effect of Inoculant Addition to Ductile Iron on Drill Life.
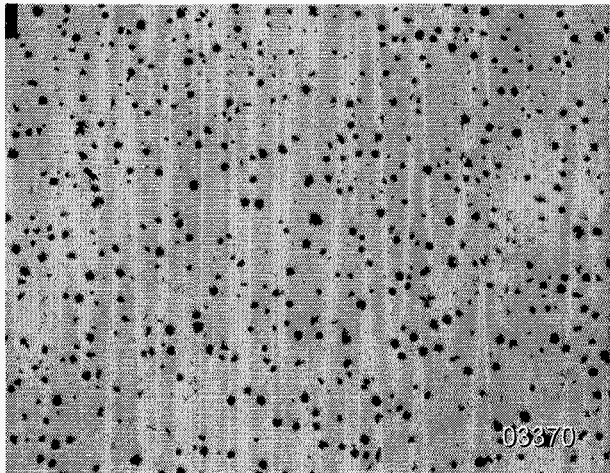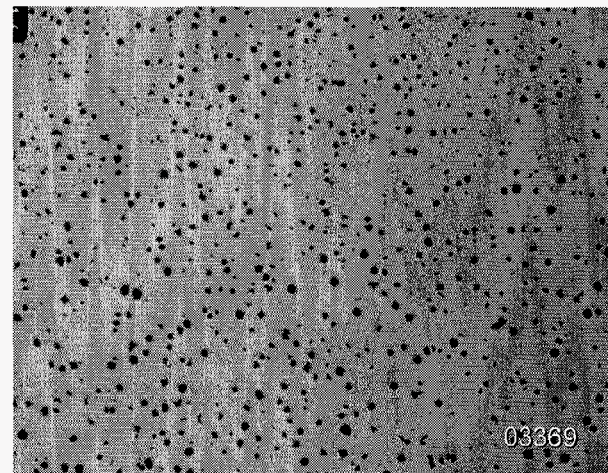
DA2 - Tool Life @ 124 sfm = 52

DB2 - Tool Life @ 124 sfm = 101
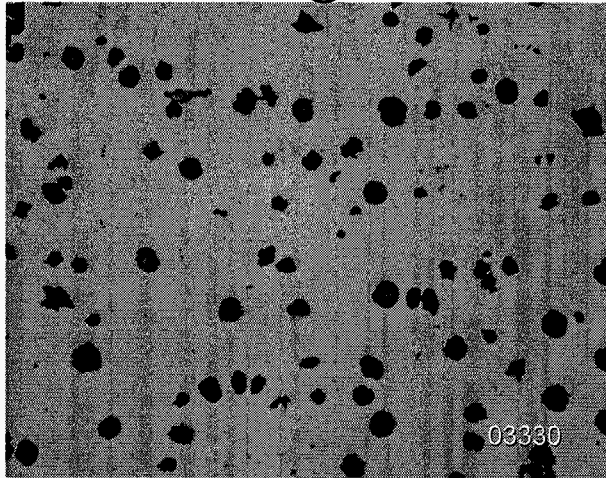
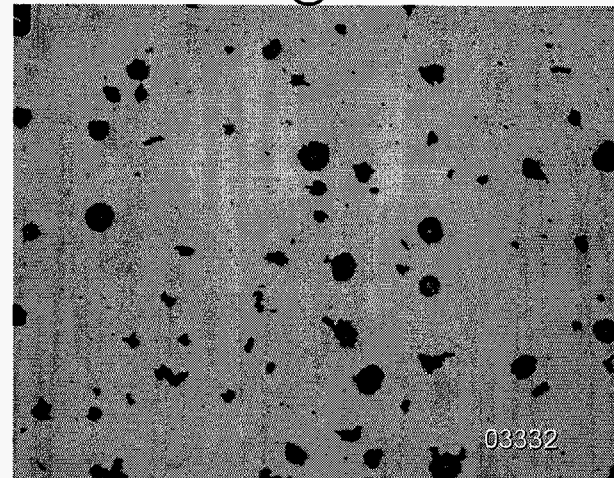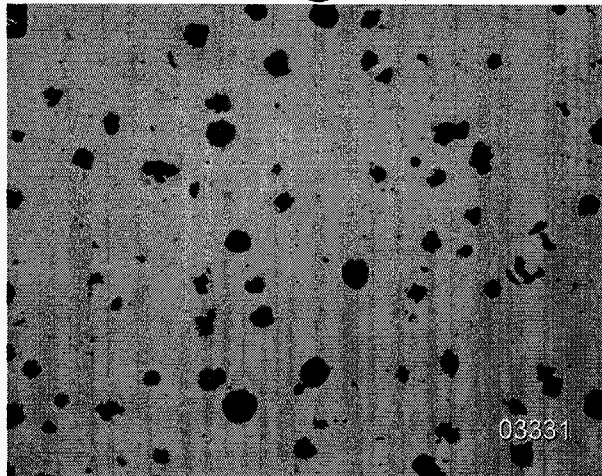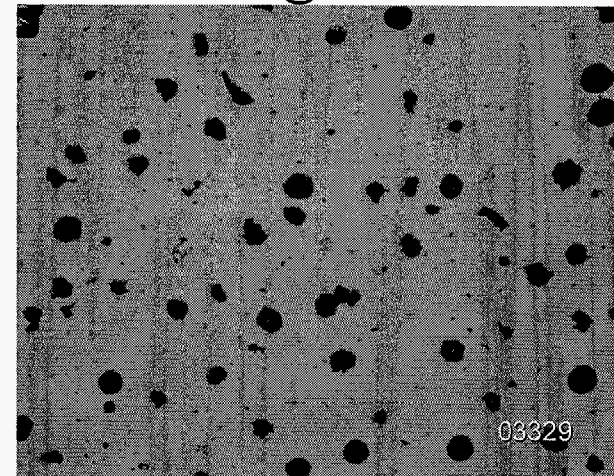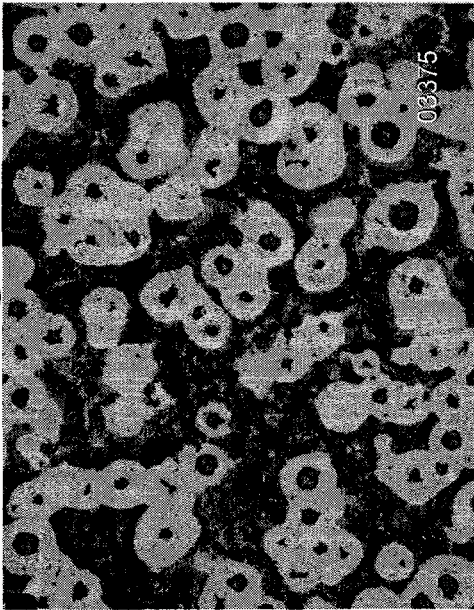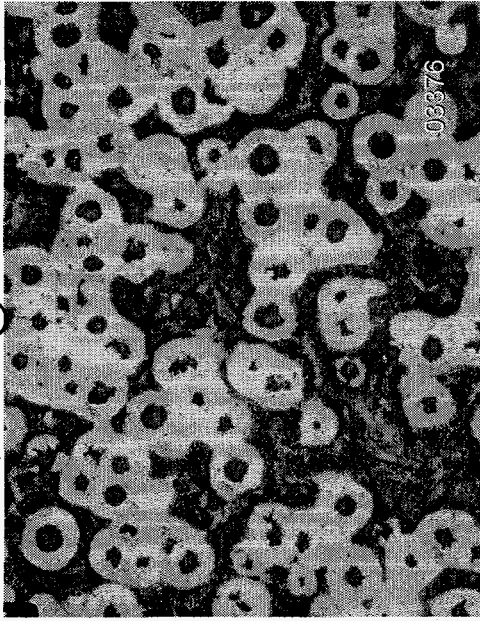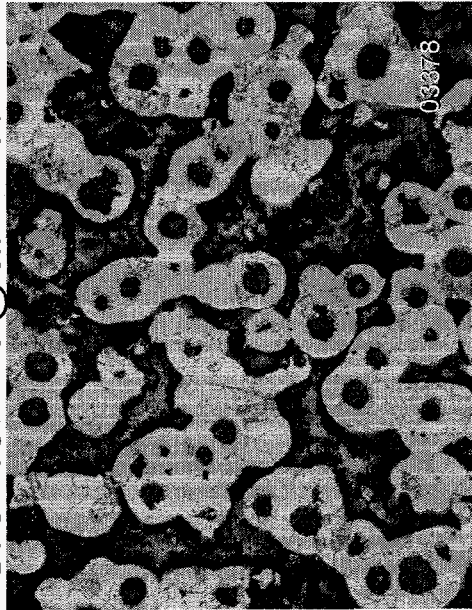DF5 - Tool Life @ sfm = 101

DF2 - Tool Life @ 124 sfm = 241

Magnification = 20x

Figure 46.   Representative Unetched Microstructures for the 65-45-12 Inoculated Ductile Irons - 20X

DA2 - Tool Life @ 124 sfm = 52

DB2 - Tool Life @ 124 sfm = 101

DF5 - Tool Life @ sfm = 101

DF2 - Tool Life @ 124 sfm = 241

Magnification = 67x

Figure 47.   Representative Unetched Micrrostructures of the 65-45-12 Inoculated Ductile Irons - 67X

DB2 - Tool Life @ 124 sfm = 101
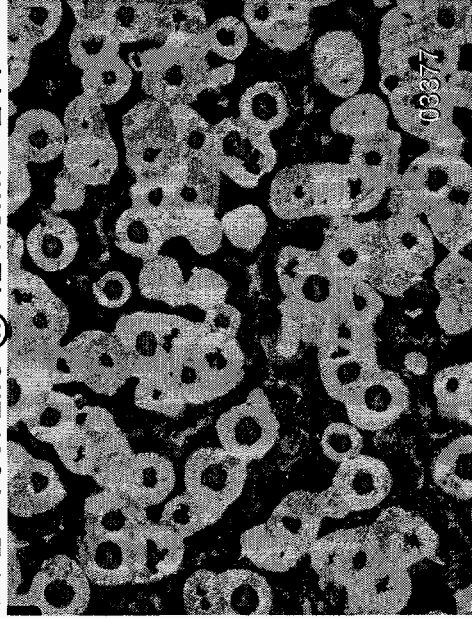
DF2 - Tool Life @ 124 sfm = 241

DA2 - Tool Life @ 124 sfm = 52

DF5 - Tool Life @ sfm = 101

Magnification = 67x

Figure 48. Representative Etched Microstructures of the 65-45-12 Inoculated Ductile Irons - 67X

91

Table XII.

Microstructural Features of the Ductile Iron Inoculation Plates

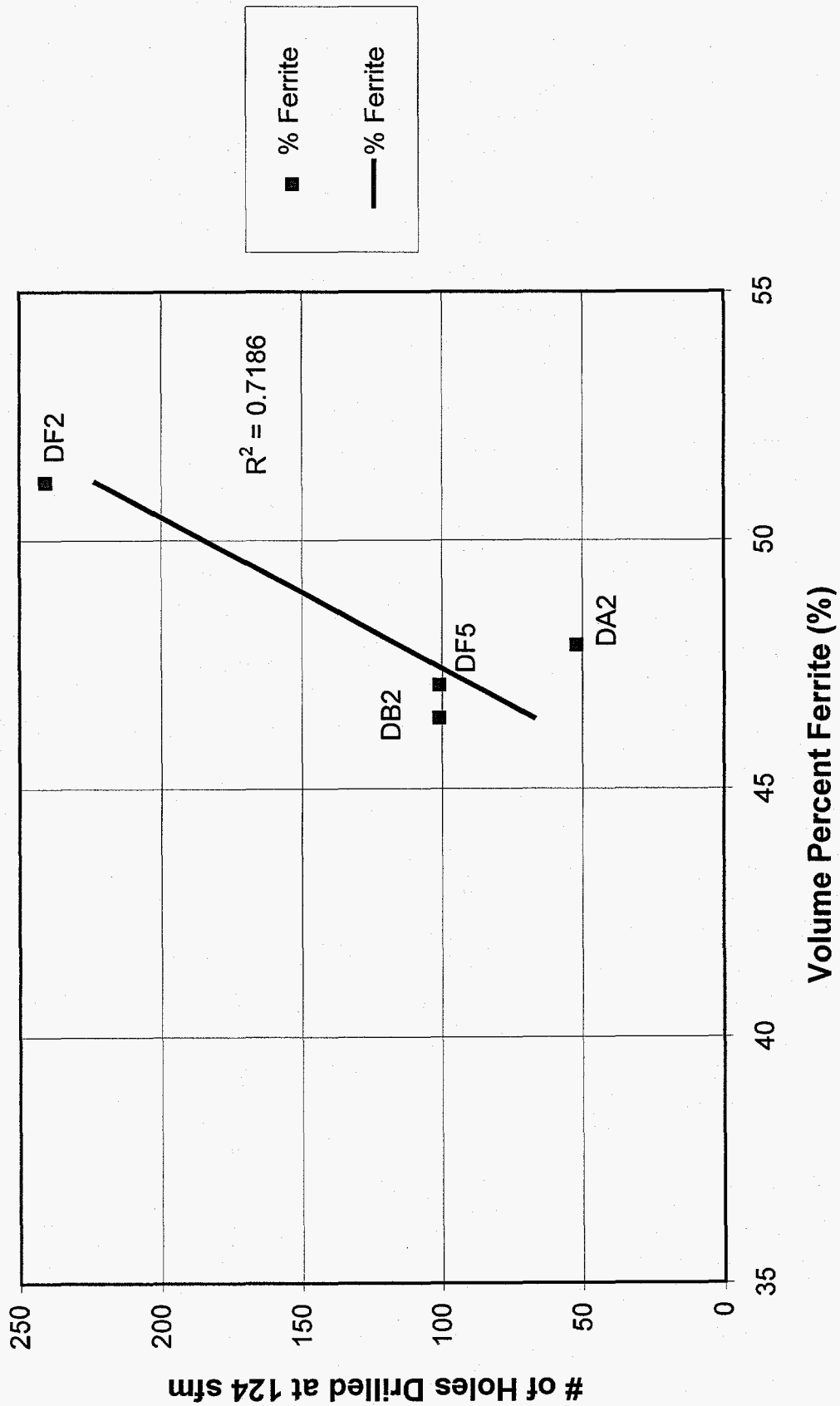| Sample	Inoculant	Wt %	Tool Life @ 124 sfm	Volume % Ferrite	Volume % Pearlite
DF5	Calsifer 75	0.5	101	47	41
DF2	Calsifer 75	0.5	241	51	36
DA2	SB5	0.2	101	48	40
DB2	VP216	0.2	52	46	43

Figure 49. Effect of Volume Percent Ferrite in the Inoculated Ductile Iron Plates on Drill Life.

average nodule circumference. Machinability decreased as the number density graphite nodules increased as shown in Figure 50.

Microcarbide Analysis. The effect of microcarbides on tool life is illustrated in Figure 51. The microcarbide contents were relatively low and did not correlate with tool life.

SUMMARY

There is no doubt that the weight fraction microcarbides in iron significantly affects machinability. Other characteristics -- such as graphite volume fraction, graphite shape and distribution, strength, and matrix hardness -- can affect machinability, but microcarbides have a dominate effect.

Three factors probably control the formation of microcarbides in iron, and these are:

(1)   the cooling rate of the iron from the eutectic temperature to the eutectoid temperature,
(2)   the concentrations of pearlite stabilizing elements (Cr, Mn, Mo, N, etc), and
(3)   the concentrations of elements that retard diffusion of carbon from austenite to graphite including tin, antimony, and copper.

The practical question is going to be how to best control and reduce the microcarbides under specific situations. This will be the focus of the next phase of research.
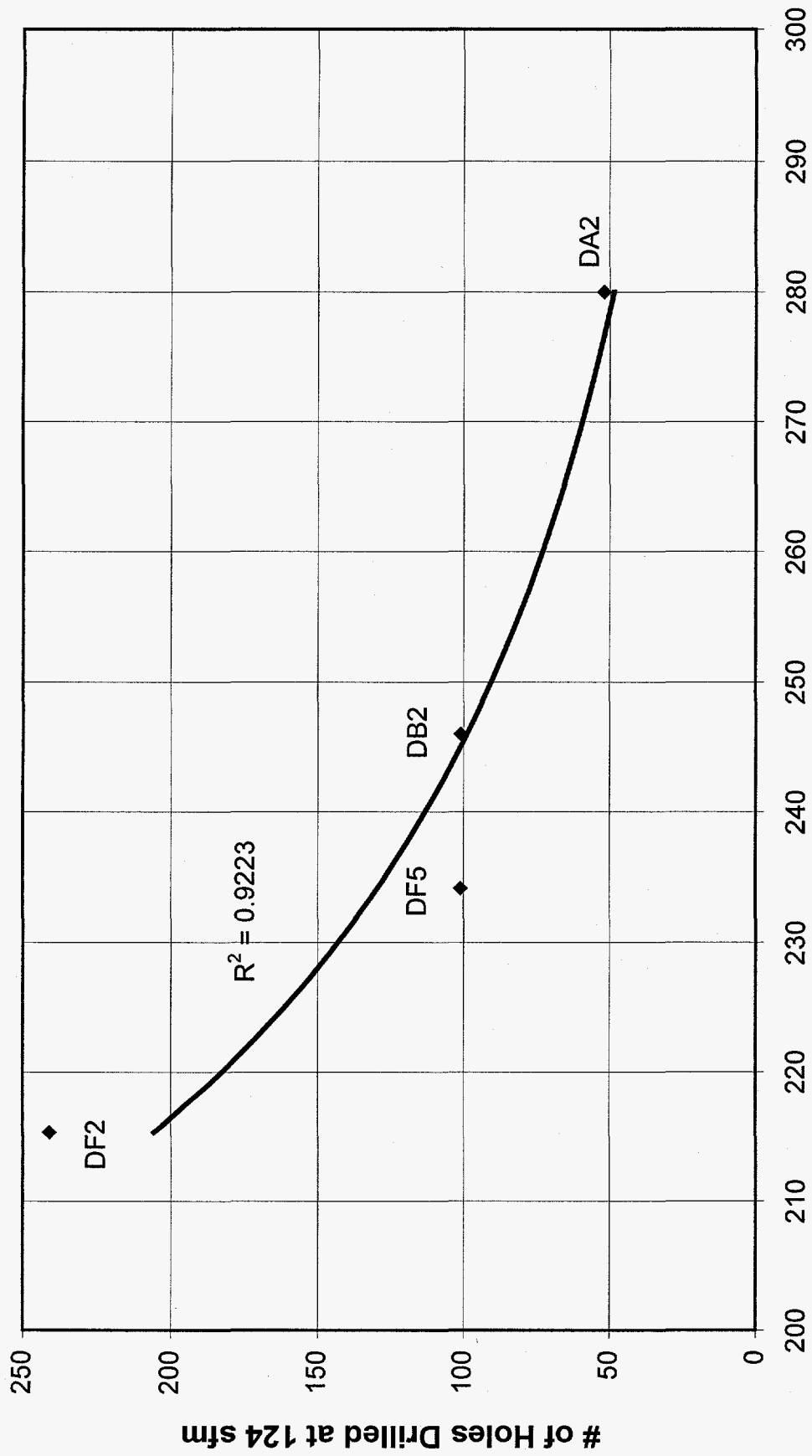
Figure 50. Effect of Number Density of Graphite Nodules in the Inoculated Ductile Iron Plates on Drill Life.
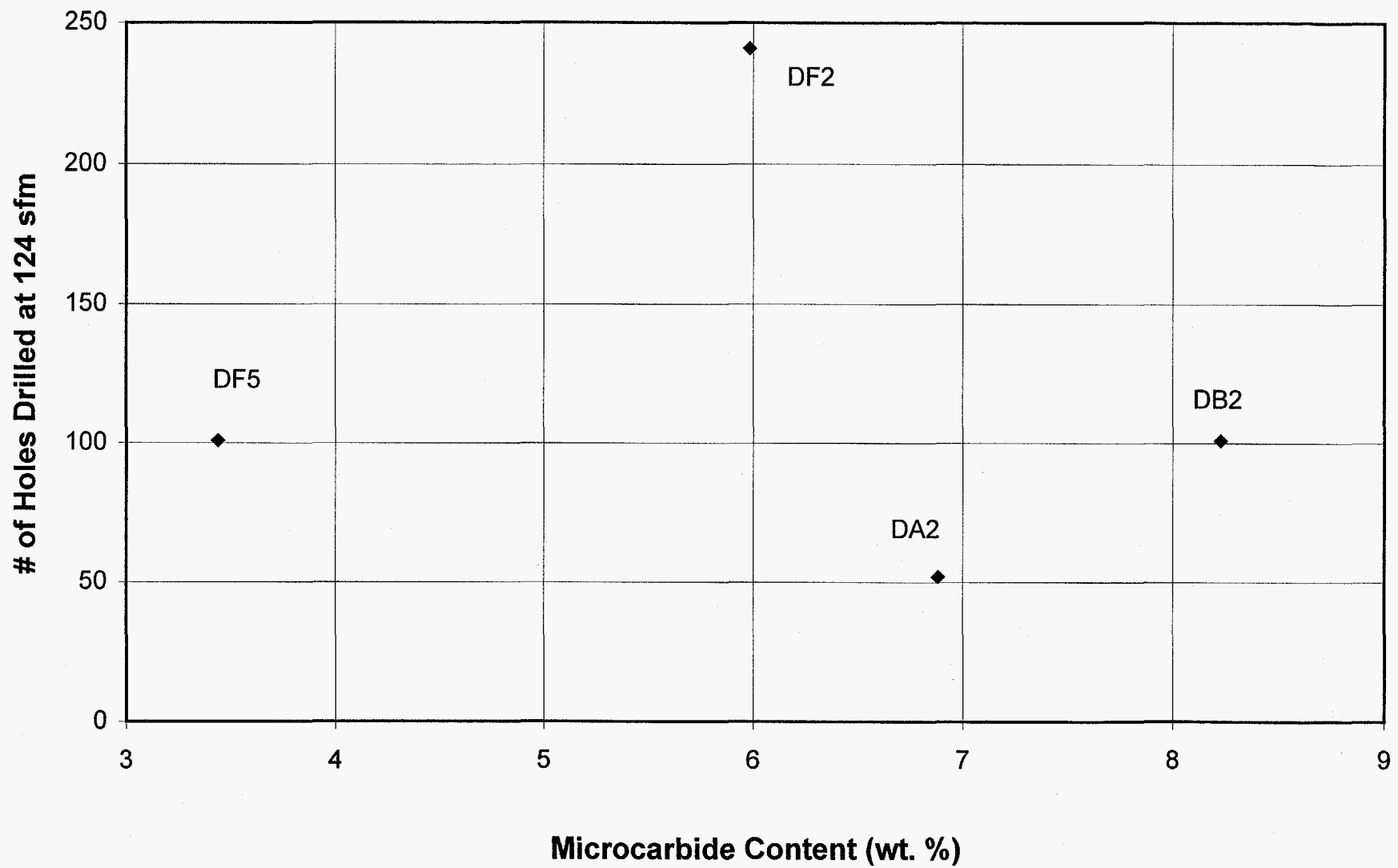
Figure 51. Effect of Microcarbide Content in the Inoculated Ductile Iron Plates on Drill Life.

CONCLUSIONS

1. Microcarbides present in the irons were found to dominate the machinability of iron.

2. Pearlitic irons considered to have "acceptable" machinability were found to contain from 8.9 to 10.5% by weight microcarbides.

3. The tool wear rate increased when machining at higher surface speeds and when machining irons containing higher weight percentages of microcarbides.

4. All irons containing above 11.5% microcarbides consistently exhibited poor machinability.

5. Graphite size, shape, and distribution affected machinability, but the microcarbide weight fraction had a dominant effect.

6. Tool wear results obtained using tungsten carbide (WC) and cubic boron nitride (CBN) cutters in commercial machine shops paralleled the results obtained with HSS. Irons with higher microcarbide contents exhibited higher rates of tool wear.

7. The amount of inoculant added to 60-45-12 ductile iron was found to have a significant effect on tool life. Reducing the addition of a foundry grade calcium and aluminum bearing 75% FeSi inoculant from 0.5% to 0.2% increased the tool life by about 100%.

8. Tool force measurements were found to correlate with machinability of gray iron.

9. Shakeout time had a significant effect on tool life. About 30% more holes could be drilled in one set of castings cooled for 35 minutes in the mold compared to similar castings cooled for 17 minutes in the mold.

10. Above 11.5% by weight microcarbides, drill life was low even at the lowest speeds.

11. Tool life generally decreased with tensile strength, but some data points fell significantly below the trend line. The reason will be established in future work.

12. Low strength irons with high microcarbide contents produced high drill wear in spite of the low strength values.

13. Compression test results show a high correlation with tool life. Additional experiments are underway to evaluate more irons and verify the correlation.

14. Tool life decreases as the pearlite microhardness increases. The pearlite microhardness results appear to mirror the pearlite microcarbide content in the castings, but there is considerable scatter in the data.

15. Microcarbide analyses were performed on disc hubs, cylinder bores in diesel blocks, diesel heads, and brake rotors and the results correlated with reported machinability behavior.

16. Irons with higher elastic moduli (which reflect higher stiffness irons), produce higher flank face loads. Higher flank face loads, with other conditions remaining constant, produce more frictional heat and faster wear on the tool flank.

17. High flank face loads coupled with higher microcarbide concentrations in the iron have synergistic effects that increase tool flank face wear and decrease tool life.
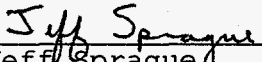
ACKNOWLEDGMENT

Our hope is that the information contained in this report will be of assistance to companies throughout the United States in advancing the technology of Clean Iron Production and Machinability.

Submitted by,   Submitted by,
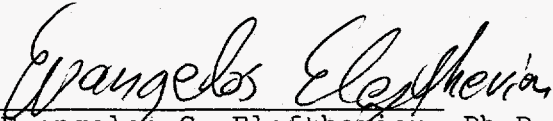
Jeff Sprague   Carl DelSorbo
Masters Degree Candidate   Masters Degree Candidate

Zoe B. Dwyer, Ph.D.   Robin Griffin, Ph.D.
Research Engineer   Electron Optic Laboratory
                                                 Manager

Evangelos C. Eleftheriou, Ph.D.   Harry Littleton
Assistant Professor   Engineering Manager

Approved by:

Charles E. Bates, Ph.D.
Research Professor

101

REFERENCES

1. Boulger, F.W. "Machining and Machinability." Metal Review, Vol. 20, March 1947, pp. 5-8.

2. Harris, G.G. Bibliography of Machinability Tests, Battelle Memorial Institute, Columbus, Ohio, 1944. 12 pages.

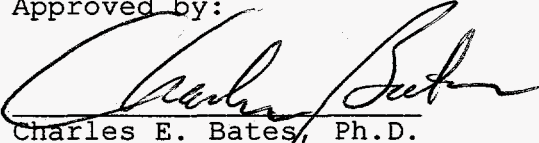3. Schlesinger, George. "How to Measure Machinability in the Shop." American Machinist, Vol. 90, November 21, 1946, pp. 117-128.

4. Egorov, S.N., and Prima, V.I., "Cutting Forces in End Milling," Soviet Engineering Research, Vol.6, No. 12, 1986, pp. 82.

5. Field, Michael, and Bullock, W.E. "Milling Cast-Iron with Carbides." Mechanical Engineering, Vol. 67, October 1945, pp. 647-658.

6. Ernst, Hans. "Physics of Metal Cutting." Machining of Metals, American Society for Metals, Cleveland, Ohio, 1938, 177 pp., P. 1-34.

7. Merchant, Zlantin N. "Photographic Studies Contribute to Better Machining Methods." Steel, Vol. 120, March 17, 1947, pp.94-97.

8. Baker, H., Ed., et al. ASM Handbook: Alloy Phase Diagrams, Volume 3. Materials Park, Ohio: Asm International, 1992.

9. Metals Handbook, 8th Ed., Vol. 8, American Society for Metals, Metals Park, Oh, 1973, P. 236, 275, 276.

10. Hughes, I. C. H. "Solidification of Cast Iron," Journal of the Australian Institute of Metals, 10 (1965), 4.

11. Keverian, J., Taylor,H. F. And Wulf, J. "Experiments on Spherulite Formation in Cast Iron," American Foundryman, Vol. 22 (1953), P.85.

12. Minkoff, "Factors Affecting Growth of Spheroidal Graphite," Modern Castings, Vol. 41 (1962), p. 66.

13. W. Patterson and D. Amann, "Contribution to the Theory of Graphite Crystallization," Giesserei, Vol. 48(1963), p. 364.

14. J. W. Gibbs, The Collected Works of Gibbs. Vol. 1; New Haven: Yale University Press, 1948.

15. I. G. Neizhko, "The Formation of Graphite Types in Fe-Si-C Alloys", Russian Castings Production, No. 12(1963), p. 572.

16. The Cupola and Its Operations. 3rd Ed.; Des Plaines: American Foundrymen's Society, 1965.

17. C. R. Loper, Jr. and R. W. Heine, "Graphite Formation During Solidification of Cast Iron," AFS Transactions, Vol 69 (1961), p. 583.

18. H. Morrogh, "Graphite Formation In Grey Cast Irons and Related Alloys," British Cast Iron Research Association Journal of Research and Development, Vol. 5 (1955), p. 655.

19. A. Wittmose and E. Houdremont, "Studies on Graphite Formation in Hypoeutectic Gray Iron," Arch. Eisenhiittenwesen, Vol. 27 (1956), p. 241.

20. W. C. Filkins et al., "Gray Iron Inoculation and Inoculants Evaluation," AFS Transactions, Vol. 70 (1962), p. 893.

21. S. C. Massari and R. W. Lindsey, "Some Factors Influencing the Graphitizing Behavior of Cast Iron," AFS Transactions, Vol. 49 (1941).

22. A. Boyles, "The Freezing of Cast Iron," Transactions, American Institute of Mining and Metallurgical Engineers, Vol. 125 (1937), p. 141.

23. J. F. Wallace and P. F. Wieser, Trace Elements in Gray Iron. Special AFS Publication, 1965.

24. H. Morrogh, "Progress and Problems in the Understanding of Cast Irons," AFS Transactions, Vol. 70 (1962), p. 449.

25. A. Boyles, The Structure of Cast Iron. ASM, 1947.

26. J. F. Wallace, "Structure of Graphite in Gray Iron," Gray Iron News, (November, 1960), p. 14.

27. R. P. Dunphy and W. S. Pellini, "Nodule Genesis and Growth in Magnesium Treated Hypoeutectic Irons," Memoires No. 8 Congress International De Fonderie, Brussels: 1951.

28. A. Wittmoser, "Comments on the Question of Solidification of Cast Iron with Nodular Graphite," Giesserei, Vol. 40 (1953), p. 75.

29. Malleable Iron Castings. Cleveland, Ohio: Malleable Founders Society, 1960.

30. R. W. Heine and P. C. Rosenthal, Principles of Metal Casting. Mcgraw Hill, 1955.

31. Thermocalc, Division of Computational Thermodynamics, Department of Materials Science & Engineering, Royal Institute of Technology, S100-44, Stockholm, Sweden.

32. Warneche, Dr. G. <u>Machining of Gray Iron and Steel--metal Cutting and Microstructure.</u> Video Produced by the Technical University of Hanover, 1976.

USE OF THIS REPORT AND INFORMATION
CONTAINED THEREIN

<u>Publicity</u>

This report and the information contained therein is the property of the individual or organization named on the face hereof and may be freely distributed in its present form. However, the University of Alabama at Birmingham (UAB) hereby reminds Sponsor that no advertising or publicity matter, having or containing any reference to the University of Alabama at Birmingham, shall be made use of by anyone, unless and until such matter shall have first been submitted to and received the approval in writing of UAB. (UAB does not usually approve any type of endorsement advertising.)

<u>Limitation of Liability</u>

The faculty and staff of UAB associated with this project have used their professional experience and best professional efforts in performing this work. However, UAB does not represent, warrant or guarantee that its research results, or product produced therefrom, are merchantable or satisfactory for any particular purpose, and there are no warranties, express or implied, to such effect. Acceptance, reliance on, or use of such results shall be at the sole risk of Sponsor. In connection with this work, UAB shall in no event be responsible or liable in contract or in tort for any special, indirect, incidental or consequential damages, such as, but not limited to, loss of product, profits or revenues, damage or loss from operation or nonoperation of plant, or claims of customers of Sponsor.

Report No.: CIP Final - January 1995-March 1997

To: The Department of Energy, the American Foundrymen's Society, and Afs-Doe Clean Iron Production Consortium Member Companies

Date: April, 1997

UAB Account No. 527965, 633167

E-File: cip96FNL.DOE